

DESIGN OF MODULAR SELF CONTAINED
KNEE AND ANKLE PROSTHESES

BY

Jason E. Mitchell

Dissertation

Submitted to the Faculty of the
Graduate School of Vanderbilt University
in partial fulfillment of the requirements
for the degree of

DOCTOR OF PHILOSOPHY

in

Mechanical Engineering

December, 2014

Nashville, Tennessee

Approved:

Dr. Michael Goldfarb

Dr. George E. Cook

Dr. Paul H. King

Dr. Eric J. Barth

Dr. Robert J. Webster III

To Audrey

ACKNOWLEDGMENTS

First, I would like to thank Dr. Richard Houghton who gave me a real love for machine design and encouraged me to come to Vanderbilt for graduate school. Next, I would like to thank my advisor Dr. Michael Goldfarb who allowed me the freedom to make all of the designs presented here my own. Thanks also goes to the other members of my committee, Dr. George Cook, Dr. Paul King, Dr. Eric Barth and Dr. Robert Webster for their time and support.

The mechanical designs are presented here for systems which are too complex for one person to master, so I would like to thank the other members of the development team; Dr. Frank Sup and Dr. Atakon Varol who worked on earlier versions of these systems and on whose shoulders we stand, Dr. Brian Lawson and Amanda Shultz who developed control systems for the transtibial and transfemoral versions respectively, and Don Truex who designed motor controllers and all manner of electronic circuits.

Last, I would like to thank my wife Audrey for seeing me through three degrees, numerous jobs, countless moves, and seven children all while encouraging me to chase my dreams.

TABLE OF CONTENTS

	Page
LIST OF FIGURES.....	VI
LIST OF TABLES.....	X
Chapter I OVERVIEW.....	1
INTRODUCTION AND MOTIVATION	1
LITERATURE SURVEY.....	2
SCOPE AND SUMMARY OF RESEARCH.....	4
ORGANIZATION OF THE DOCUMENT	5
II MANUSCRIPT 1 DESIGN OF A HYBRID TRACTION/CABLE DRIVE	
TRANSMISSION FOR LOWER LIMB POWERED PROSTHETICS.	6
ABSTRACT	6
INTRODUCTION AND DESIGN CONTEXT	6
DESIGN OBJECTIVES	8
MECHANICAL DESIGN	9
TRACTION DRIVE	9
TRACTION DRIVE TESTING	16
CABLE DRIVE DESIGN.....	17
TRACTION/CABLE DRIVE ASSEMBLY TESTING.....	25
CONCLUSIONS	25
III BELT, CHAIN, CHAIN TRANSMISSIONS AND	
PARALLEL LINK LOAD CELL DEVELOPMENT	27
INTRODUCTION.....	27
PROTOTYPING AND TESTING	27
LOAD CELL.....	31
CONCLUSIONS	34
IV GENERATION 2.0 TRANSFEMORAL PROSTHESIS.....	35

INTRODUCTION	35
PROSTHESIS DESIGN	36
ANALYSIS	38
ASSEMBLY	40
LOAD CELL	43
SPRING FOOT	45
CONCLUSIONS	49
V GENERATION 3 TRANSFEMORAL AND TRANSTIBIAL PROSTHESES	51
INTRODUCTION	51
GENERATION 3.0 TRANSTIBIAL PROSTHESIS	52
GEN 3.0 TRANSTIBIAL PROSTHESIS CONCLUSIONS	54
LOAD CELL	54
GENERATION 3.0 TRANSFEMORAL AND GENERATION 3.1 TRANSTIBIAL PROSTHESES	55
TRANSMISSION CHARACTERIZATION.....	56
CONCLUSIONS	61
VI MANUSCRIPT 2: A POWERED KNEE AND ANKLE PROSTHESIS FOR TRANSFEMORAL AMPUTEES	62
ABSTRACT	62
INTRODUCTION	62
PROSTHESIS DESIGN	64
CONTROL APPROACH	69
EXPERIMENTAL IMPLEMENTATION AND BIOMECHANICAL RESULTS.....	73
CONCLUSION.....	83
VII CONTRIBUTIONS AND FUTURE WORK	84
REFERENCES	85

LIST OF FIGURES

	Page
Figure 1-1. Vanderbilt Powered Prosthesis shown inside anatomical envelope.	1
Figure 1-2. Power Knee prosthesis developed by Ossur (left)	2
Figure 1-3. Prototype powered ankles developed by Bellman et. al. (left) and Au and Herr (right).	3
Figure 1-4. Vanderbilt Powered Prosthesis.....	4
Figure 1-5. A pictorial history of leg designs by the author.	4
Figure 2-1. CAD model of traction/cable drive (left) and photograph of working prototype (right).	9
Figure 2-2. Endview CAD model of traction/cable drive (left) and photograph of working prototype (right).	10
Figure 2-3. CAD model of exploded view of traction drive.....	11
Figure 2-4. CAD model showing cross section of traction drive.	12
Figure 2-5. Traction coefficient as a function of surface pressure.[28]	13
Figure 2-6. Pressure profile between Cylinders, reproduced from [23].	13
Figure 2-7. CAD model showing bidirectional operation of self wedging mechanism.	14
Figure 2-8. Parameters governing operation of self wedging traction drive.	15
Figure 2-9. Photograph of experimental setup showing traction drive coupled to hysteresis brake.	16
Figure 2-10. Traction drive efficiency as a function of torque and speed.	17
Figure 2-11. CAD model of cable drive (left) and photograph of working prototype (right).	18
Figure 2-12. CAD rendering of input shaft and close up photograph of cables.....	18
Figure 2-13. Cable life fatigue chart for various cable types [34].....	19
Figure 2-14. Cable on wheel and shaft.	20
Figure 2-15. Surface plots showing the relationship between number of cables, number of wraps and and cable width and cable life.	22
Figure 2-16. CAD model of cable drive and traction drive (left).....	22
and photograph of working prototype (right).	22
Figure 2-17. Detail of cable termination (left) and top and bottom die (right).	23
Figure 2-18. Photograph showing close-up view of cable tensioning mechanism and cable termination.	23
Figure 2-19. CAD model of deflection measurement gauge (left) and gauge in use (right).	24
Figure 2-20. FEA analysis showing displacement of tensioning finger.	25
Figure 3-1. Inverted ankle assembly bench top testing setup.	29
Figure 3-2. CAD models of first prototype belt-chain-chain leg shown inside the anatomical envelope (left) and without covers right showing the drive train (right).....	30
Figure 3-3. Photographs of assembled leg prototype.....	31
Figure 3-4. Sensorized prosthetic foot.	32

Figure 3-5. CAD models of load cell showing a side view (left) and exploded view (right).	33
Figure 3-6. Cross sectional view of load cell showing operation.	33
Figure 3-7. Side and isometric views of experimental test load cell.	34
Figure 4-1. Isometric, right (showing 90% male anatomical envelope), front.....	36
and left side (with covers hidden) views of leg.....	36
Figure 4-2. Front and left side views of the ankle drive train with and without belt and chains.	37
Figure 4-3. Ankle drive train.	38
Figure 4-4. Finite element analysis of sprocket.	39
Figure 4-5. Finite element analysis of knee Lateral shell showing applied loads (left) finite element mesh (center) and von-Mises stress (right).....	39
Figure 4-6. Shell halves with drive train installed.....	40
Figure 4-7. Knee assembly with eccentric timing tool.....	41
Figure 4-8. Sonic tension meter.	41
Figure 4-9. Leg with and without spacer.	42
Figure 4-10. Right, front and left side views of leg.....	43
Figure 4-11. Detail view of load cell incorporated into leg housing. Parallel linkages are shown in dashed white lines.	44
Figure 4-12. Exploded view of load cell included in belt-chain-chain leg.	44
Figure 4-13. The powered tethered prototype.	45
Figure 4-14. CAD rendering of spring foot design and ankle assembly.....	46
Figure 4-15. CAD model showing spring foot shown in plantarflexion (left), neutral (center), and dorsiflexion (right).	46
Figure 4-16. The reduction in ankle torque required by the transmission by the addition of a spring in parallel for fast walking taken from averaged normal biomechanical data [3].	47
Figure 4-17. CAD model of ankle showing leaf spring-ankle moment arm.	47
Figure 4-18. FEA analysis of spring foot showing von Mises stress (left) and maximum deflection (right).	48
Figure 4-19. FEA prediction of force vs. deflection of the spring of CFRP leaf spring.....	49
Figure 4-20. Picture of spring foot.....	49
Figure 4-21. Test subject wearing belt-chain-chain leg.....	50
Figure 5-1 Transmissions of Gen 2.0 and 3.0 ankle units, showing a linear vs. folded configuration. Also showing the addition of an embedded angular position sensor and cam roller configuration in Gen 2.0.	52
Figure 5-2. A picture of the physical prototype from Schultz et al. [38].....	53
Figure. 5-3. Power and torque vs. percent of stride for the Gen 3.0 prosthesis, from Shultz et al [38].....	53
Figure. 5-4. Curved and straight spring feet.	54
Figure 5-5. The double four bar load cell (left) and a cross section showing the steel spring (right)	54

Figure 5-6. Gen. 3.0 Transfemoral and Gen. 3.1 Transtibial Prostheses showing fit inside a 50% male anatomical envelope (left), enclosed electronics and battery (center left) modularity of knee, loadcell and ankle units (center right) and configured for shortest build height of 8% female (right).....	56
Figure 5-7. Experimental setup for measuring stiffness and damping of knee (left) and ankle (right)	57
Figure 5-8. Commanded and measured stiffness at the knee joint (left) and ankle joint (right).	58
Figure 5-9. Measured stiffness of foot spring.....	59
Figure 5-10. Commanded and measured damping at the knee joint (left) and ankle joint (right).	59
Figure 5-11. Experimental setup for measuring open loop torque response of knee ankle joint (left) and ankle joint (right).....	60
Figure 6-1. A rendering of the CAD model of the powered prosthesis.	65
Figure 6-2. Overview of the embedded system architecture. Inputs to the main controller include absolute encoders for each joint; an analog voltage signal from the load cell, measured via an onboard 10-bit A/D converter; and an integrated 6-axis inertial measurement unit which communicates over a serial peripheral interface (SPI). Outputs to the main controller include an optional controller area network (CAN) interface for real time data monitoring on a computer, a wireless Bluetooth interface also for data monitoring, and a microSD card reader for both data logging and parameter selection. The inputs to the servo-controller include incremental encoders for each joint; Hall effect sensor signals from the brushless DC motors; and analog current measurement signals from the three phases of each brushless DC motor (via the onboard 10-bit A/D converter). The outputs of the servo-controller are pulse-width modulated (PWM) signals that control the brushless motor MOSFET bridges.	69
Figure 6-3. Experimentally measured response of both knee and ankle joints to a 40 Nm step command in joint torque.	70
Figure 6-4. The supervisory state machine for the powered prosthesis.	72
Figure 6-5. The walking state machine for the powered prosthesis. Phases 0 and 1 emulate the virtual impedance equation described by (1), with parameters tuned for each subject and listed in Table II. Phase 2 executes a trajectory as described in the text, and automatically reverts to Phase 0 upon completion of the trajectory (when ρ_s , the percentage of the stride, is equal to 100%). The transition from Phase 0 to Phase 1 is governed by the listed condition, where θ_k is the knee angle and θ_{th} is a predetermined threshold. The transition from Phase 1 to Phase 2 is governed by the listed condition, where θ_a is the ankle angle and θ_{th} is a separate, predetermined threshold.	73
Figure 6-6. A subject walking with the powered prosthesis.	75
Figure 6-7. Knee and ankle kinematics for 3 amputee subjects using the powered prosthesis. For the knee joint, 0 deg corresponds to full knee extension, and flexion is positive. For the ankle joint, positive angles represent dorsiflexion and negative angles represent plantarflexion. The dots represent average state transitions for each subject (from Phase 0 to Phase 1, and from Phase 1 to Phase 2). The crosses represent toe off, as measured by the load cell. The largest standard deviations for each subject at the knee were 6.95, 6.85, 4.27 deg at 86, 84, and 85% of stride for subjects A, B, and C, respectively. The largest standard deviations for each subject at the ankle were 4.44, 2.68, and 1.88 deg at 57, 58, and 71% of stride for subjects A, B, and C, respectively.	77

Figure 6-8. Knee and ankle kinetics for 3 amputee subjects using the powered prosthesis. For the knee joint, a positive torque is a flexive torque. For the ankle joint, positive torque is a dorsiflexive torque. The dots represent average state transitions for each subject (from Phase 0 to Phase 1, and from Phase 1 to Phase 2). The crosses represent toe off, as measured by the load cell..... 79

Figure 6-9. Knee and ankle powers for 3 amputee subjects using the powered prosthesis. For both joints positive power is power delivered by the joint, and negative power is power absorbed by the joint. The dots are average state transitions for each subject (from Phase 0 to 1, and from Phase 1 to 2). The crosses denote toe off, as measured by the load cell..... 82

LIST OF TABLES

	Page
Table 2-1. Traction Drive Testing Parameters	17
Table 3-1. Summary of bench top Belt Chain tests.....	28
Table 6-1. Mechanical and Electrical Characteristics of the Powered Prosthesis	66
Table 6-2. Subject Data and Prosthesis Configuration	74
Table 6-3. Level Walking Parameters for the Three Test Subjects	76
Table 6-5. Parameters for the Knee and Ankle Transmission Models	78

CHAPTER I

Overview

Introduction and Motivation

As of 1999, there were more than 300,000 transfemoral amputees living in the United States alone [1]. Losing a lower limb and specifically the power that it generates, has a major impact on ambulation including having to expend up to 60% more metabolic energy [2] and exert three times the affected-side hip power and torque [3].

The Vanderbilt Powered Prosthesis [4] was designed by the author and is the only powered knee-ankle prosthesis in existence. It is a highly functional prosthesis which restores near normal gait in transfemoral amputees, but has several characteristics which make it impractical for use on a regular basis outside of a research lab.

Some of these issues are due to the use of a ballscrew in a slider crank configuration for joint actuation. These characteristics include, excess noise (>75 dB), low cycle life and poor fit within the anatomical envelope (Fig 1-1). In addition, the design is difficult to shield both for pinch points and against dust. Last the ankle and knee ball screw actuation unit extend well past the midpoint between the two joints which makes it impossible to separate the ankle to make a transtibial prosthesis.



Figure 1-1. Vanderbilt Powered Prosthesis shown inside anatomical envelope.

Another issue is the use of a sensorized foot as a load cell to measure ground contact. This is impractical for a robust product because it is expensive to make, has wires which pass across the joint and precludes quick changing of foot sizes.

The last issue, is the steel biasing spring: which stores energy during the stance phase of gate and returns it during push off. The steel spring is heavy and has low cycle life.

This work aims to develop new and novel transmission, load cell and biasing spring designs to overcome the aforementioned limitations. It is the hypothesis of this work that lower limb prosthetic devices can be designed which provide biomechanically normal levels of torque, speed, and range of motion in self-contained, reliable, quiet, and anatomical packages. In addition these devices can provide robust mechanical platforms to develop and test a broad range of activities and control strategies.

It is important for the designer of such a device to consider both the activities that may be performed and the control strategies that may be employed. Activities will dictate the speed and torque required from the transmission and the forces imposed on the drivetrain and structure. Control strategies which incorporate impedance control (primarily used by this device) will demand that the device be back drivable, be able to provide high series stiffness if needed and have an inherently low parallel damping.

Literature Survey

Research in powered transfemoral prostheses has been carried out since the 1970's. Some of this early work is described in [5-11]. The author of this work will limit the present discussion to recently developed knee and ankle devices.

Knee designs fall in the range of fully powered to partially powered, with partially powered designs proposing to capture or leverage some of the passive dynamics of normal gate. The only commercially available powered knee prosthesis (Fig. 1-2) is the Power Knee by the prosthetics company Ossur [12]. An agonist-antagonist knee design is discussed by Martinez-Villalpando et al. [13] and a "semi active" knee is presented by Lambrecht et al. [14]



Figure 1-2. Power Knee prosthesis developed by Ossur (left)

Ankle designs generally have a series or parallel elastic element which transmits torque to the corresponding joint of the prosthesis through a slider-crank mechanism. The SPARKy ankle prosthesis developed at Arizona State University by Bellman et al.[15] and Hitt et al. [16] is a “active foot-ankle” prosthesis that provides net power generation at the ankle joint using an electric motor and lead screw in series with a spring or springs, Fig 1-3. Bergelin et al. [17] describe an ankle prosthesis which incorporates a brushless DC motor coupled to a right angle gear head in series with a four bar linkage. An “Ankle Mimicking Prosthesis” is described by Cherelle et al. [18] which uses a motor, gearhead and ballscrew as the sliding link of a four bar mechanism to provide joint torque.

The BiOM ankle prosthesis described by Au et al. [19] and Herr et al. [20] is a commercially available ankle prosthesis that provides net power generation at the ankle with electric motors and both series and parallel elastic actuation, Fig. 1-3.



Figure 1-3. Prototype powered ankles developed by Bellman et. al. (left) and Au and Herr (right).

The Vanderbilt Powered Prosthesis [4] is a knee and ankle prosthesis that uses brushless motors (Maxon EC30 Powermax) connected to ball screws in a slider-crank arrangement to rotate the knee and ankle joints. In addition, the ankle joint has a coil spring in parallel with the ball screw to store energy during the late stance phase of gate and to decrease the motor torque during toe off, Fig. 1-4.

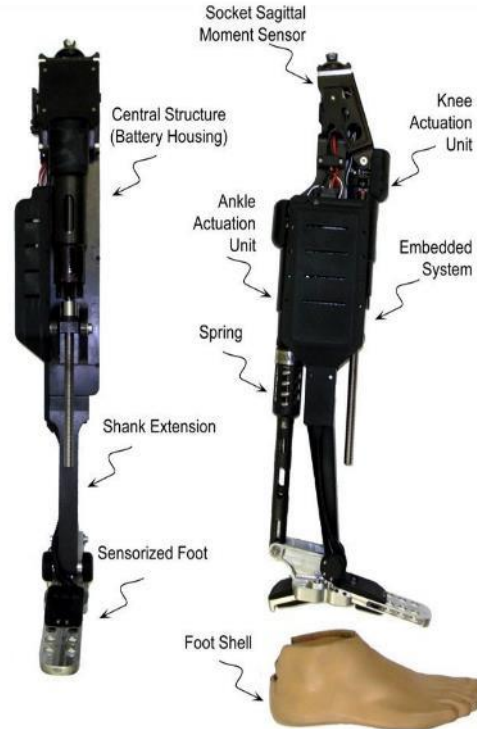


Figure 1-4. Vanderbilt Powered Prosthesis.

Scope and Summary of Research

This work marks a departure from the authors previous work designing ball screw actuated legs, Fig. 1-5, in collaboration with Fite et al. [21] (below left), Sup et al. [22] (center left), Sup et al. [4] (center), to new designs (center right and far right).



Figure 1-5. A pictorial history of leg designs by the author.

While the ball screw based legs were highly functional and able to reproduce biomechanically healthy gait, they had the issues previously mentioned that needed to be addressed to become a commercially viable product.

Toward this end a fundamentally new mechanical design was developed and tested. The design process included investigation of a novel traction-cable drive transmission and several belt-chain drive combinations. A parallel link ground sensing load cell was developed that is capable of sensing ground contact while mechanically filtering out moments. Lastly a leaf spring-foot combination was developed to decrease ankle motor torque at toe off.

Organization of the Document

The dissertation is organized into seven chapters. Chapter I presents the introduction and scope of work. Chapter II is comprised of a manuscript which describes the design of a novel hybrid traction/cable drive transmission for powered lower limb prostheses. Chapter III describes the development of a three stage belt, chain, chain drive transmission and a parallel link load cell which will serve as the basis for prostheses designs in subsequent chapters. Chapter IV presents a self-contained knee–ankle prosthesis using the above mentioned transmission and load cell. Chapter V describes the development of a separable knee and ankle prostheses. Chapter VI is comprised of a journal manuscript which presents the mechanical and IC designs along with the control strategy and kinematics and kinetics. Chapter VII concludes with the contribution and future direction.

CHAPTER II

Manuscript 1 Design of a hybrid traction/cable drive Transmission for lower limb powered prosthetics.

Jason Mitchell, and Michael Goldfarb

Vanderbilt University

Nashville, TN

Prepared for submission to the ASME Journal of Mechanical Design

Abstract

This paper presents the design and preliminary testing of a novel high ratio hybrid traction/cable drive transmission for lower limb powered prostheses. A bench top prototype of the device was designed and fabricated. The device was tested up to the maximum torque expected for fast walking in the human knee joint and preliminary efficiency mapping was performed.

Introduction and Design Context

As of 2005, there were approximately 620,000 persons living in the United States (i.e., one in five hundred) with major lower limb amputations [1]. Of these, according to the National Limb Loss Information Center, approximately 48% (300,000) are transfemoral amputees. Assuming a similar rate of prevalence throughout the world, one would expect approximately 7 million transfemoral amputees worldwide. Losing a lower limb, and specifically the power that it generates, has a major impact on ambulation. Transfemoral amputees expend up to 60% more metabolic energy [2] and exert up to three times the affected-side hip power and torque [3] relative to healthy individuals.

Recent advances in battery and electric motor designs have facilitated the emergence of powered prostheses. Like the healthy neuromuscular system, a powered prosthesis can both generate and absorb

power, and therefore can better replicate the energetic behavior of the healthy limb, relative to existing passive devices. One of the challenges associated with the design of such prostheses is implementing joint actuation that can provide the relatively high power-to-weight and torque-to-weight ratios that characterize healthy joints during human locomotion. One well-developed means of power transduction for such prostheses is a rare-Earth magnet DC motor. Use of a DC motor, however, requires a high-ratio transmission between the motor output and leg joint output, which converts the motor power from a high-speed, low-torque regime, to the relatively low-speed, high-torque regime associated with the biomechanics of human movement. Specifically, the torque/speed regime of the motor is typically different from the torque/speed regime of human biomechanics by two orders of magnitude; such systems typically require transmission ratios of approximately 200:1. Further, an appropriate transmission should provide a high efficiency in order to preserve power and torque; minimize or eliminate backlash in order to facilitate stable closed-loop control; accommodate the requisite joint range of motion; and minimize weight and audible noise for user acceptance.

Several electric-motor-actuated powered prostheses have been described in the engineering literature, each with an associated joint transmission.

Sup et al. [4] describe a prosthesis with powered knee and ankle joints, in which each joint incorporates a transmission in which a DC brushless motor directly drives a ballscrew, which transmits torque to the corresponding joint of the prosthesis through a slider-crank mechanism. Although the transmissions are nonlinear (as a result of the slider-crank), the nominal transmission ratio for both joints is approximately 200:1, averaged over the 120 deg and 65 deg range of the motion (ROM) of the knee and ankle joints, respectively. Bergelin et al. [17] describe an ankle prosthesis which incorporates a brushless DC motor coupled to a right angle gear head in series with a four bar linkage. Again the four bar makes the output nonlinear, but the estimated nominal transmission ratio is 140:1 over the 60 deg range of motion (ROM). The SPARKy foot ankle prosthesis designed by Hit et al. [16] utilizes a DC brushless motor with gear head driving a lead screw which forms the slider link in a slider-crank mechanism to transmit torque to the ankle joint. The estimated nominal transmission ratio is 300:1. The ROM is not stated explicitly, but is at least 30 deg. The ankle prostheses designed by Au et al. [19] also employs a slider crank mechanism with a brushless DC motor and a ball screw. It has a stated transmission ratio of 170:1. The ROM is not given, but is estimated to be at least 30 deg. The Power Knee transtibial prosthesis from Ossur [12] utilizes a electric motor and ball screw in a slider - crank arrangement. No published data exists to estimate the transmission ratio, but it is reasonable to expect something in the range of the systems described above.

The above transmissions use gears, ball screws or lead screws all of which have issues with noise and durability. In addition, a motor axially coupled to either a ball screw or lead screw with the transmission ration needed here is inherently quite long precluding its use in shorter ankle prostheses. A two stage traction/cable drive transmission designed to reduce transmission size, lower operating noise, and increase reliability is presented here.

Friction based drive trains are one of the most basic types of power transmissions. They can be seen in everyday use in train wheels, car tires. Typically a friction drive is a rolling element drive that relies on dry friction to transmit torque and one of the rolling elements is generally a softer material.

When a traction fluid is added to the transmission, it is generally referred to as a traction drive. The traction fluid separates the rolling elements by a thin film that becomes solid under the extreme pressures in the contact zone. Traction fluid can shear if the torque is high enough compared to the normal force thus providing overload protection. It also helps to spread the contact area between the rolling elements, decreasing contact force and surface fatigue. In addition, traction fluid decreases noise by absorbing vibration, and the fluid dissipates heat inside a transmission. Traction drives don't exhibit the torque ripple, noise and backlash inherent in even the best geared transmissions [23].

Additionally traction drives can be much more efficient and compact when compared to equivalent ratio geared systems [23, 24] and have efficiencies between 90 and 99%. [24, 25]

A cable drive can have low friction and zero backlash [26] if sized properly. Cable drives can come in a few different forms. In one embodiment, the first end of the cable is clamped rigidly to a rotating shaft (driving shaft) and wound around it. The other end is clamped to an adjacent parallel or orthogonal shaft (driven shaft) and wound around it until the cable is tight. As the driving shaft rotates in the clockwise direction, the driven shaft rotates in the counterclockwise direction. A second cable is wound around each shaft in the opposite direction for bidirectional operation. The ratio of the diameters of the two shafts is the transmission ratio. A device that uses this approach is the Whole Arm Manipulator (WAM) arm robotic arm from Barrett Technology [26].

One disadvantage of this two cable, clamped method is that the clamping mechanism takes up a significant amount of shaft space compared to the cable itself. Secondly, a large amount of space is needed for cable storage or take up. This may be acceptable with one cable but for a multiple cable assembly, where more torque is needed, this arrangement becomes much larger.

In a second embodiment of the cable drive, two cables are replaced by one and the two ends are clamped to the driven shaft via tensioning mechanisms. Instead of being clamped to the driving shaft, the cable is wrapped around it as many times as necessary and tensioned to have sufficient frictional force to hold it. This approach was used in the second stage of the device described below. The second stage is a cable drive (instead of another Traction drive for example) because the required normal force loading mechanism (described in detail below) would make the package significantly taller compared to the cable drive.

Design Objectives

There were several design criteria for this transmission. First the output had to be about 100 N-m which is approximately the maximum torque at the ankle joint during normal speed walking [27]. In this paper, the transmission was envisioned as knee joint, but could be used as an ankle in the future. The transmission ratio subsequently should be ~200:1 and able to output ~200 W based on the choice of a Maxon EC30 brushless DC motor as the input. This motor was chosen due to its exceptional power density. The range

of motion should be 5 deg. of hyperextension and at least 115 deg. of flexion. Additionally the transmission should have no backlash, be quiet (<50dB), and have a lifetime of ~1M cycles. For controllability, the device should be back drivable and therefore have a relatively high efficiency.

The device should be compact in width to stay within the natural anatomical envelope and in length from the knee center to the distal end to fit users with a shorter leg length. Furthermore the standard prosthetic pyramid connection should be as close to the knee center as possible to accommodate longer residual limbs and the device should have minimal weight.

Mechanical Design

The traction/cable drive was designed to fit inside the anatomical envelope of a 50 percentile male shank. A CAD model of the traction/cable drive is shown in a knee assembly, Fig. 2-1. Connection to the residual limb socket is made via a standard prosthetic pyramid fitting. A battery resides inside a structural housing that connects the transmission to a foot or ankle prosthetic via a standard prosthetics pylon.

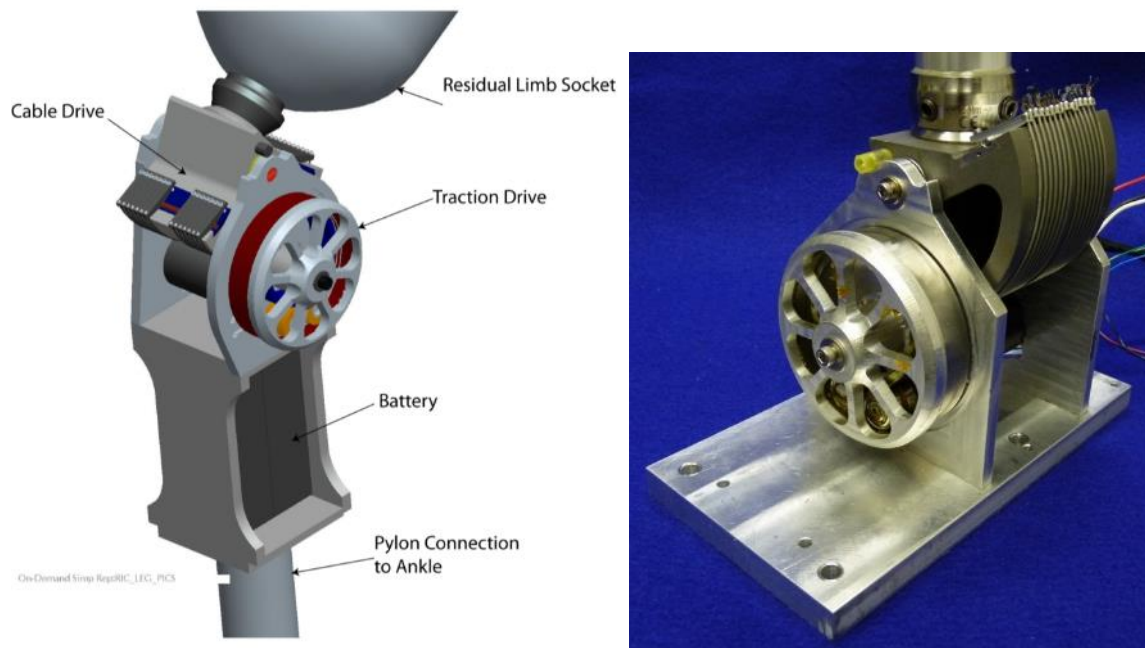


Figure 2-1. CAD model of traction/cable drive (left) and photograph of working prototype (right).

Traction Drive

The transmission starts with a 200 Watt EC30 4 pole brushless DC motor from Maxon Motor USA. To use the motor in the range of torques and speeds needed for human walking, the transmission ratio needs to be approximately 200:1. For compactness each stage was designed to have an equivalent reduction of 14:1 which gives a total ratio of 196:1.

Torque from the motor shaft is transmitted indirectly through two sets of support planets and a loading planet to a outer ring, Fig. 2-2. The outer ring is attached to an output shaft that is used for the cable drive

input shaft through a spoked aluminum hub. Normal forces between components are generated in proportion to the input torque by the loading planet with a “self wedging” mechanism which will be described in more detail below.

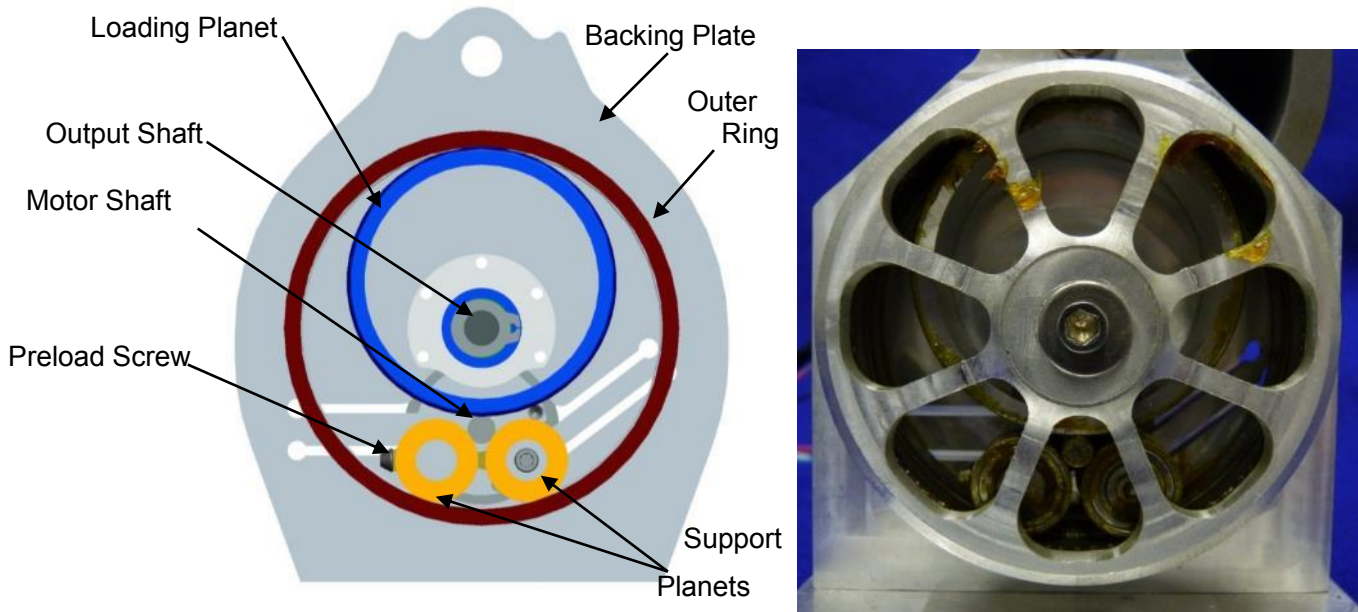


Figure 2-2. Endview CAD model of traction/cable drive (left) and photograph of working prototype (right).

The output shaft assembly consists of the output shaft, and two bearings which are slip fit inside a bearing block, Fig. 2-3. The assembly is then bolted to the backing plate. The outer ring is positioned in a hub with locating tabs and epoxied into place, and the hub assembly is bolted onto the end of the output shaft and locked to it with ball bearing keys. Each set of support planets consists of two ball bearings press fit onto a shaft with a spacer in between. One set of support planets is bolted to the backing plate and the second set is connected to it through a preload screw. It was necessary to have a minimum amount of preload otherwise the loading planet would not drive itself into the wedge gap between the outer ring and motor shaft.

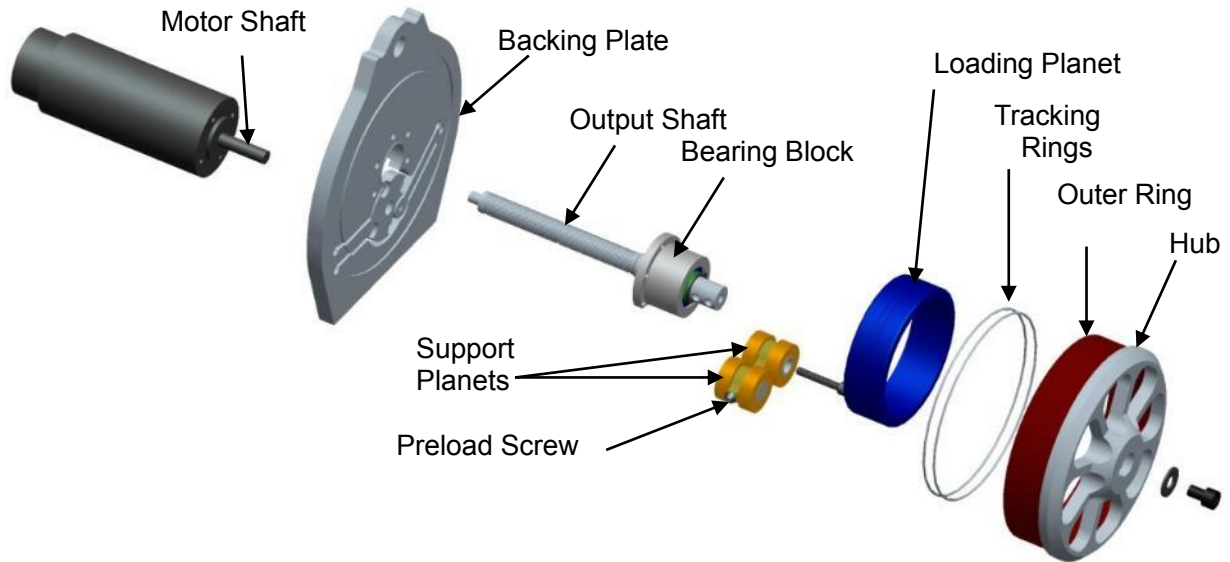


Figure 2-3. CAD model of exploded view of traction drive.

Grooves were cut in the outside of the loading planet and the inside of the outer ring, and stainless steel tracking rings were installed in the outer ring that traps the loading planet in the transverse direction, Fig 2-4. The loading planet and outer ring were both made from bearing grade 52100 steel, hardened to Rc 65, and then ground.

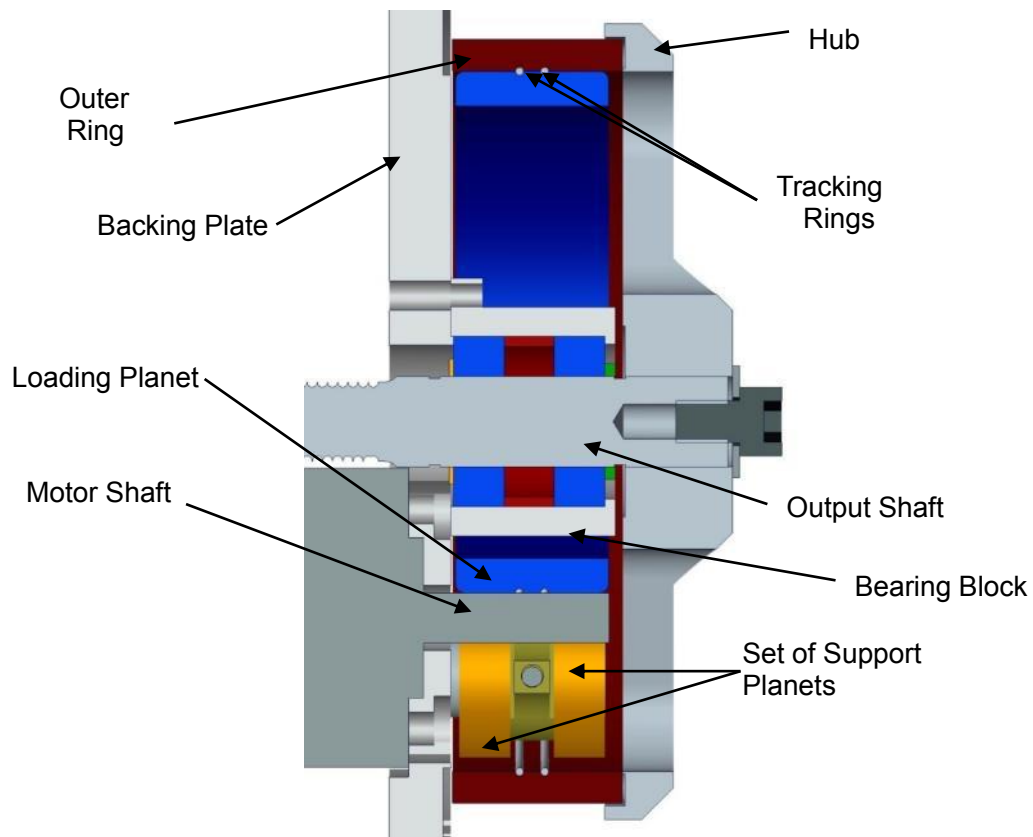


Figure 2-4. CAD model showing cross section of traction drive.

Traction grease (Santo Trac Ep-2) was added to the transmission to protect the hardened surfaces in the case of gross slip at overload. Traction grease also provides several benefits mentioned previously, such as noise and heat dissipation. Santo Trac Ep-2 traction grease is essentially Santo Trac 50 traction oil suspended in wax. A graph provided by the manufacturer showing the traction coefficient for several slide to roll ratios (SSR) as a function of surface pressure for Santo Trac 50 is shown in Fig. 2-5. Traction coefficient is analogous to friction coefficient and slide to roll ratio is the ratio of the amount of sliding of the surfaces relative to the amount of rolling. Sliding (as opposed to slipping) is caused by angular misalignment between the rollers in a cylindrical roller arrangement like the one described here. The ability to transmit torque in the presence of roller misaligned is another benefit of using traction fluid.

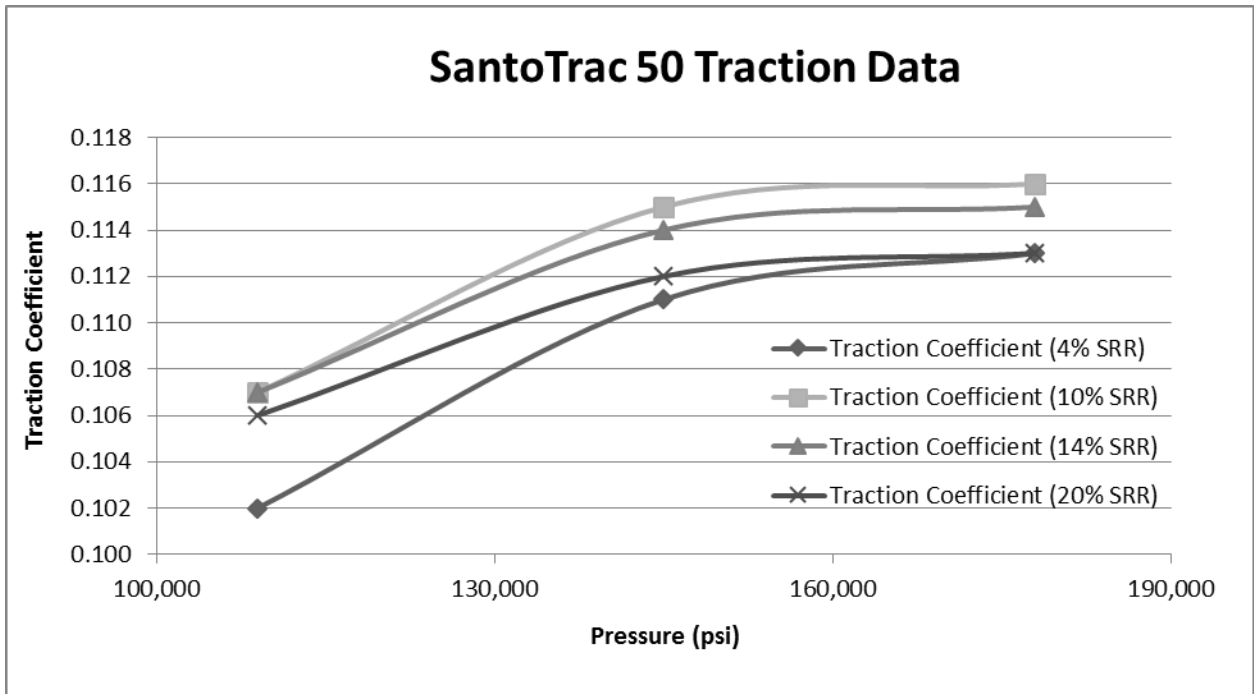


Figure 2-5. Traction coefficient as a function of surface pressure.[28]

The pressure distribution between cylindrical rollers is a semi ellipse, Fig. 2-6, and is given by:

$$P = \frac{4 F_N}{\pi 2aL} \sqrt{1 - \frac{x^2}{a^2}}$$

Where F_N is the normal force between rollers, L is the roller contact length and a is a constant which is a function of roller radii and material properties [29].

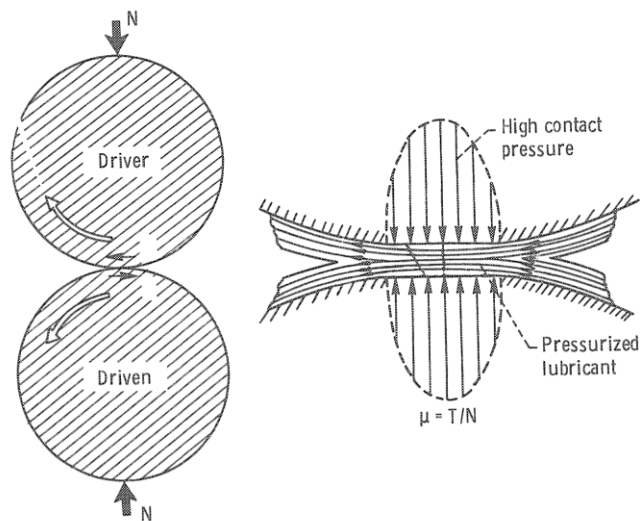


Figure 2-6. Pressure profile between Cylinders, reproduced from [23].

Several methods can be employed to get sufficient internal normal force and thus pressure for slip free operation. One is to have a slight interference fit between all of the rolling elements. Assembly would be accomplished by mechanically deforming the components or by heating certain parts of the assembly [30]. In practice it is difficult to achieve the right tolerances and to assemble the device without scuffing the rolling surfaces.

A second method would be to assemble the device and apply the normal load through external tensioners which would draw components towards each other. This method if applied externally to the centers of the support planets would add size to the system and since it would also need to be applied to both ends of the planets equally which would be difficult to do in practice. If the transmission operates under steady state torque conditions, the constant preload is not an issue, but for cyclical torque conditions encountered in walking, the transmission components would be overloaded for most of the cycle, leading to lower fatigue life.

A last method to apply the normal forces is with a “self wedging” or “self loading” mechanism. A self wedging mechanism applies normal force in proportion to the input torque thus decreasing average pressures and increasing fatigue life. Several novel self wedging configurations described by Loewenthal et al. [23] would apply significant unbalanced forces to the motor shaft and thus to the motor bearings. A balanced configuration is described by Flugrad et al. [31], but the design is only self wedging in one direction. The design chosen for this transmission is a variation of unidirectional acting designs described by Kolchi et al. [32] and Ai et al. [25]. Operation is essentially the same except that there is some hysteresis between input and output if operated in a bidirectional manner. In the present use, the hysteresis is acceptably small at the output since the traction drive is the first stage in the transmission and thus shows up at the output with a 1:14 reduction. Operation of the self wedging mechanism is shown in Fig. 2-7.

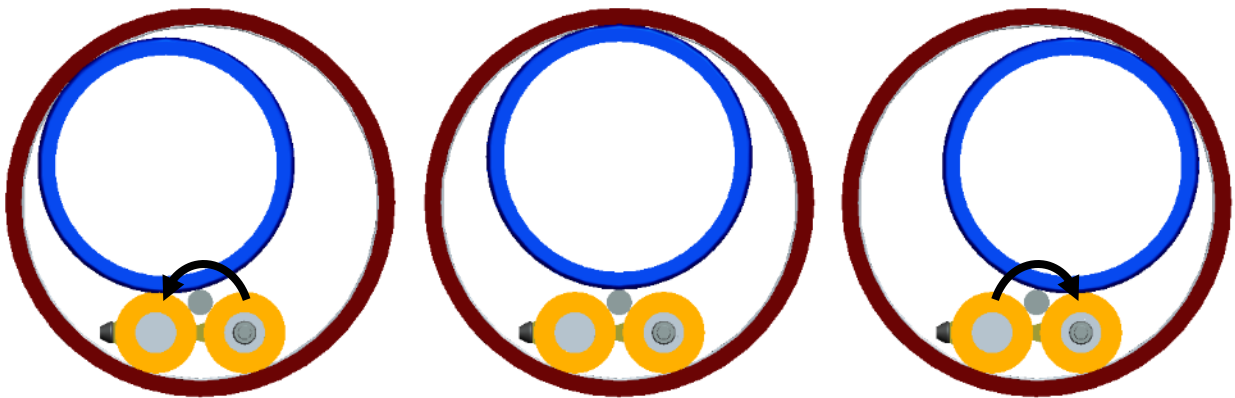


Figure 2-7. CAD model showing bidirectional operation of self wedging mechanism.

In bidirectional operation, the transmission starts in a neutral position (Fig. 2-7 center). As the motor shaft rotates counterclockwise (Fig. 2-7 left) the loading planet is driven into the wedge gap between the left support planet and the outer ring by the friction between the motor shaft and loading planet. To do this the

loading planet and outer ring must deform slightly, As the motor shaft reverses direction the loading planet passes back through the neutral position and then is driven into the wedge gap between the right support planet and the outer ring (Fig. 2-7 right). The amount that it is driven into the gap is directly proportional to the applied torque and indirectly proportional to the structural stiffness of the loading planet and outer ring. High normal force is developed between the motor shaft and loading planet, Fig. 2-8, and are balanced by normal forces from the support planets.

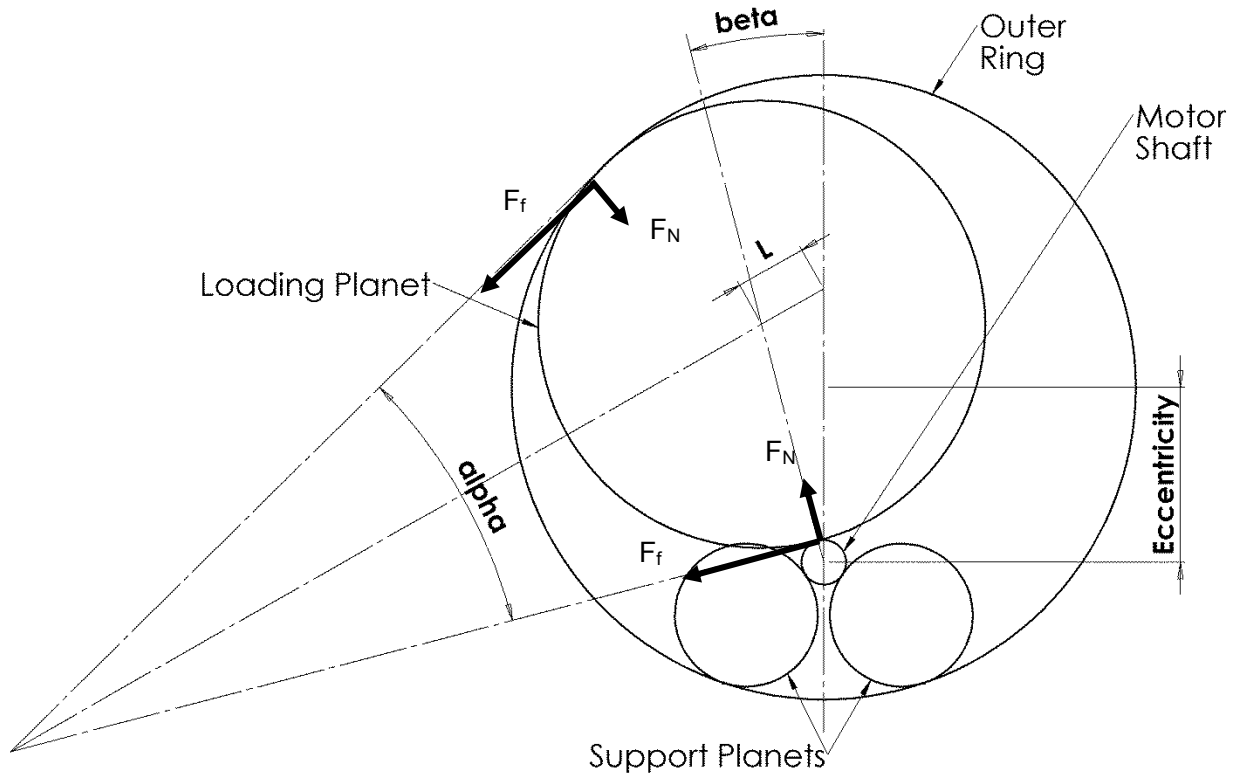


Figure 2-8. Parameters governing operation of self wedging traction drive.

Normal and frictional forces generated by the self wedging action were described by Ai et al[25] and the normal force is given by:

$$F_N = K_C \int_0^L \sin \frac{\alpha}{2} dl$$

Where L is the distance the center is displaced from its neutral position.

α is referred to as the wedge angle and is given by:

$$\alpha = 2 \tan^{-1} \mu_{fc}$$

Where μ_{fc} is referred to as the operating coefficient of friction or traction coefficient, which is a function of contact pressure as described previously.

K_c is the ratio of contact load to total surface deflection.

Finally the frictional force F_f is given by:

$$F_f = \mu_{ofc} F_N$$

Traction Drive Testing

Preliminary tests were carried out to map the efficiency of the traction drive over its operating range. The traction drive output shaft was coupled to a hysteresis brake (H250 Placid Industries), Fig 2-9. Output torque was reduced through a set of timing pulleys by a ratio of 45:120 to match the available range of the brake. Speed was measured using an optical encoder (AMT102-V, CIU Inc.).

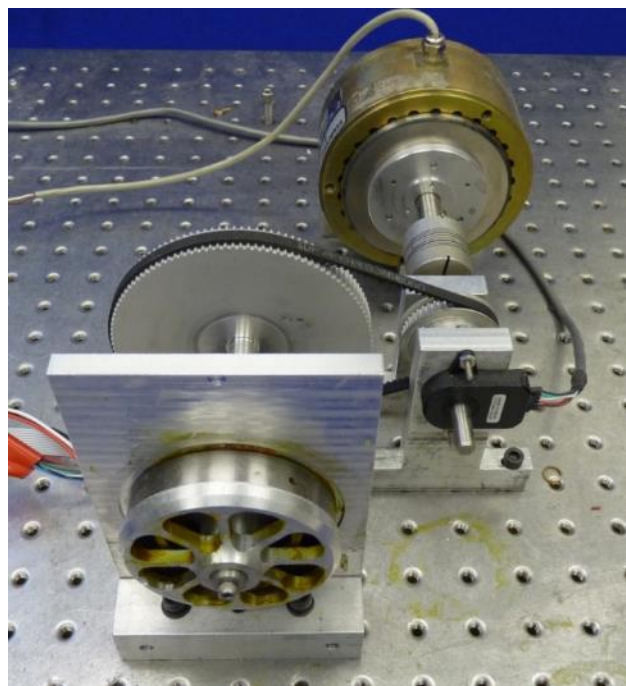


Figure 2-9. Photograph of experimental setup showing traction drive coupled to hysteresis brake.

During testing the brake torque and motor speed were set to give the desired output shaft torque and speed matrix as given in Table 2-1.

Output shaft torque (mN-m)	speed (rpm)		
	923	36	255
358	36	255	890
171	36	255	890

Table 2-1. Traction Drive Testing Parameters.

Results of the preliminary efficiency tests are shown in Fig. 2-10. Efficiency shows an increase with torque and a decrease with speed. An increase in efficiency with increased torque is expected because the surface normal forces and thus traction coefficient increases with increased torque as discussed above. This effect was also observed by Loewenthal et al. [23], and a decrease in traction coefficient with increasing surface speed was experimentally observed by Loewenthal et al. [33] for Santo Trac 50.

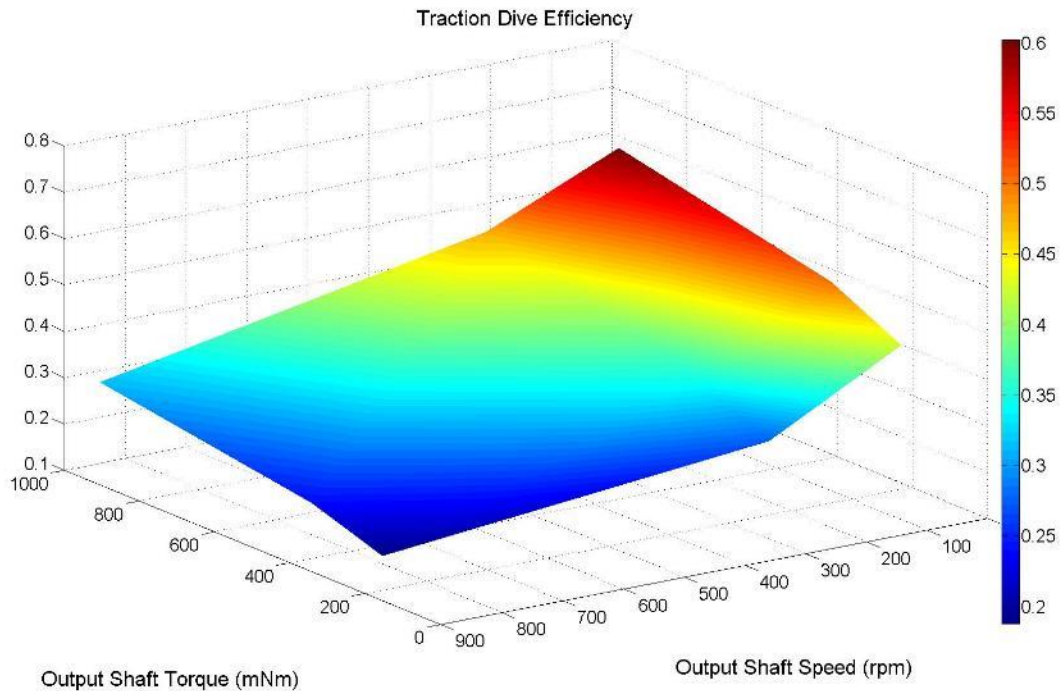


Figure 2-10. Traction drive efficiency as a function of torque and speed.

Cable drive Design

The second stage is a cable drive where the output shaft of the friction drive is the input shaft of the cable drive, Fig. 2-11. Fourteen cables are double wrapped around the input shaft and terminated on each end at the cable wheel at tensioning beams. In this way the cables are frictionally coupled to the input shaft and rigidly attached to the cable wheel such that their rotation is coupled and in opposite directions.

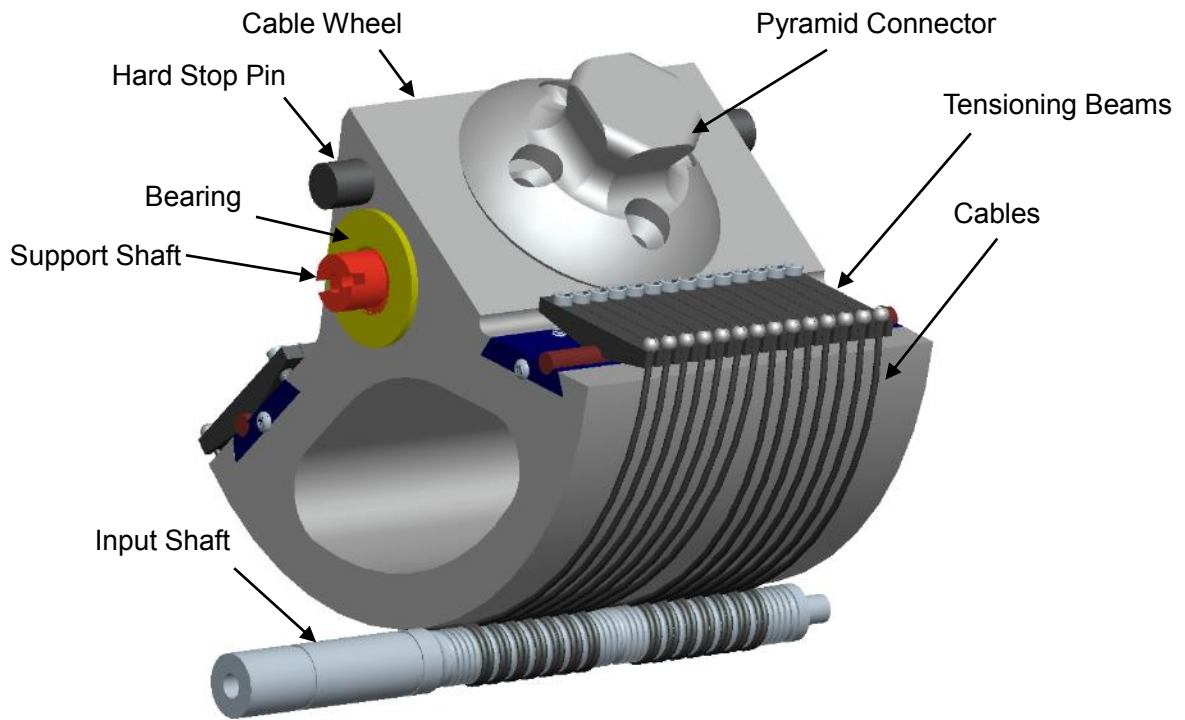


Figure 2-11. CAD model of cable drive (left) and photograph of working prototype (right).

The cable wheel has two bearings which pass through the center of rotation. A cable wheel support shaft passes through the bearings and is supported one side by the traction drive backing plate and on the other by a support bracket. Hard stops are machined into the support bracket and backing plate at the limits of knee flexion and extension, and a hard stop pin is pressed through the cable wheel. A custom pyramid adapter is attached to the top of the cable wheel.

The cables impart a net out of plane twisting moment to the axes of the input and output shafts so they are added in mirrored pairs to counteract this effect. To increase surface contact and help with cable tracking, grooves were cut in the input shaft. Since the cables are mirrored in each side of the shaft, both left and right hand grooves are added. A CAD rendering and a photograph with a close up of the grooves can be seen in Figure 2-12.

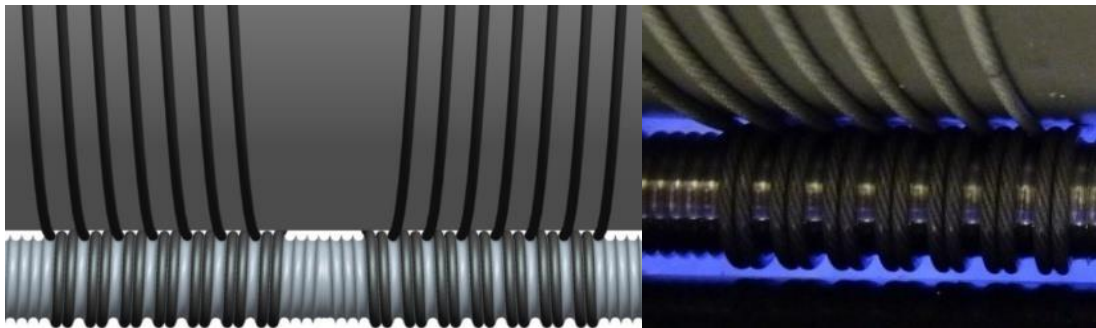


Figure 2-12. CAD rendering of input shaft and close up photograph of cables.

The tension in the cable to transmit the required torque is governed by Eytelwein's formula or the "capstan" equation.

$$T_{load} = T_{hold} e^{\mu\phi}$$

Where T_{hold} is the holding force or force at the looser end of the cable and T_{load} is the loading force, or force at the tensioning arm. The coefficient of friction between the cable and cable wheel or shaft is μ , and ϕ is the angle of contact between the cable and wheel or shaft.

Experiments were done to measure the coefficient of friction between the shaft and cable to calculate how many cables would be needed. A weight was suspended from the end of a cable that was wrapped around a shaft. The other end of the cable was affixed to a force gauge and the holding force was measured for different wrap angles. Using this, the coefficient of friction between the cable and shaft was calculated as $\mu = 0.5$. Plastic coated cables were used instead of bare cable because the coating gives it a higher coefficient of friction and the coated cables help retain internal lubrication, increasing life.

An optimization was performed to minimize the width of the cable wheel to make it fit inside the anatomical envelope and also minimize the cable life factor. Cable life factor is a predictor of cable failure at a specified number of cycles, with a lower cable factor being better. The most flexible type of cable (seven 7 x 7 strands) was used, and its cable factor is represented by the uppermost dashed line in Fig. 2-13.

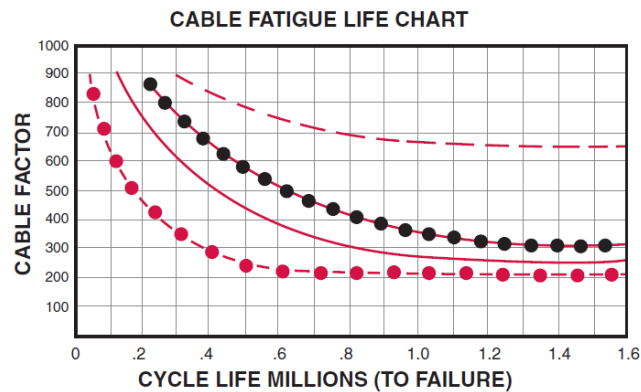


Figure 2-13. Cable life fatigue chart for various cable types [34].

Equations were derived to calculate the cable wheel width as a function of the following parameters:

1. number of cables used
2. the number of times each cable was wrapped around the input shaft
3. cable diameter
4. input shaft diameter
5. output wheel diameter.

To begin the optimization the width of one cable, Fig. 2-14, is calculated.

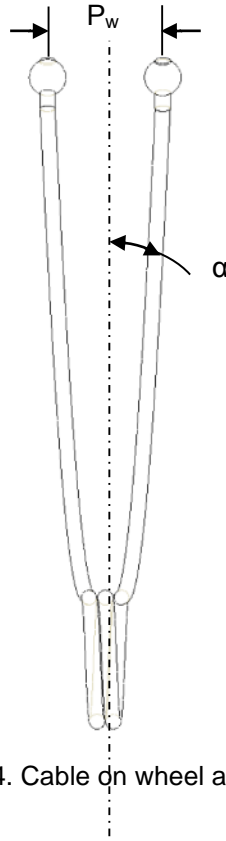


Figure 2-14. Cable on wheel and shaft.

Where α is the angle the cable makes with the input shaft and is given by:

$$\alpha = \frac{\frac{D_{cc}}{2} + .003}{D_s + D_{cc}}$$

Where D_{cc} is the coated cable diameter.

D_s is the input shaft diameter.

.003 is a nominal spacing between cable wraps.

P_w is the pitch of the cable on the output wheel:

$$P_w = 2(D_w + D_{cc})\tan(\alpha)$$

Where D_w is the diameter of the output wheel.

W_{mc} is the width of multiple cables on the output wheel:

$$W_{mc} = 2 \left[\left[\frac{P_w * \text{knee angle}}{2\pi} + \frac{2D_{cc}}{2} + \frac{P_w * \text{knee angle}}{2\pi} + D_{cc}N_r \right] + \frac{P_w * \text{knee angle}}{2\pi} + [(N_r + 1)D_{cc}]N_{cc} \right]$$

Where *knee angle* is the range of motion of the knee.

N_C is the number of cables on each half.

T_{load} is the load on the cable:

$$T_{load} = \frac{\tau}{2N_C \frac{D_W}{2} (1 - e^{-\mu \varphi})}$$

Where τ is the output torque at the knee:

μ is the coefficient of friction between the input shaft and cable

φ is the cable wrap angle:

$$\varphi = 2 \pi N_r$$

Where: N_r is the number of wraps an individual cable makes around the input shaft.

T_{hold} is the holding force to hold the load:

$$T_{hold} = T_{load} - \frac{\tau}{2N_C \frac{D_W}{2}}$$

C_F is the cable life factor:

$$C_F = \frac{T_{load}}{(D_C D_S)}$$

Where D_C is the bare cable diameter.

The goal of the optimization was to keep the width of the cable wheel (Wmc) below about 2.6 inches to fit inside the anatomical envelope and to minimize the cable life factor, C_F . Several different cable diameters were considered and finally a cable diameter of 0.037" was selected because it had the highest C_F curve of all small sized cables. A small cable diameter allows for the input shaft to be smaller as its diameter is a function of the cable minimum bend radius. With these selected the last two variables were the number of cables and the number of wraps. Fig. 2-15 shows three dimensional surface plots of cable wheel width and cable life factor as functions of these two variables.

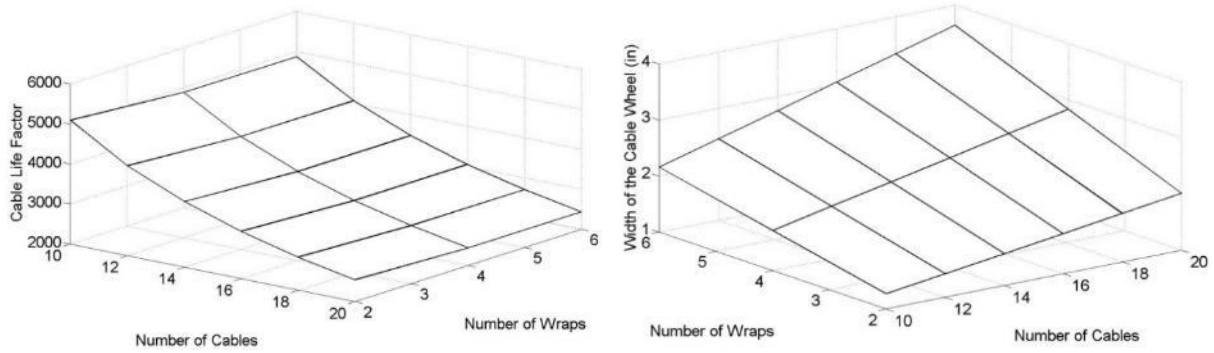


Figure 2-15. Surface plots showing the relationship between number of cables, number of wraps and cable width and cable life.

The optimization led to the selection of fourteen cables with two wraps each around the input shaft Fig. 2-16. The wheel width is 2.3 inches. Note that the cable life factor achieved was above the recommended range, but since assumed torque was the maximum knee torque and not the average knee torque, it was decided that the design was acceptable for prototyping.

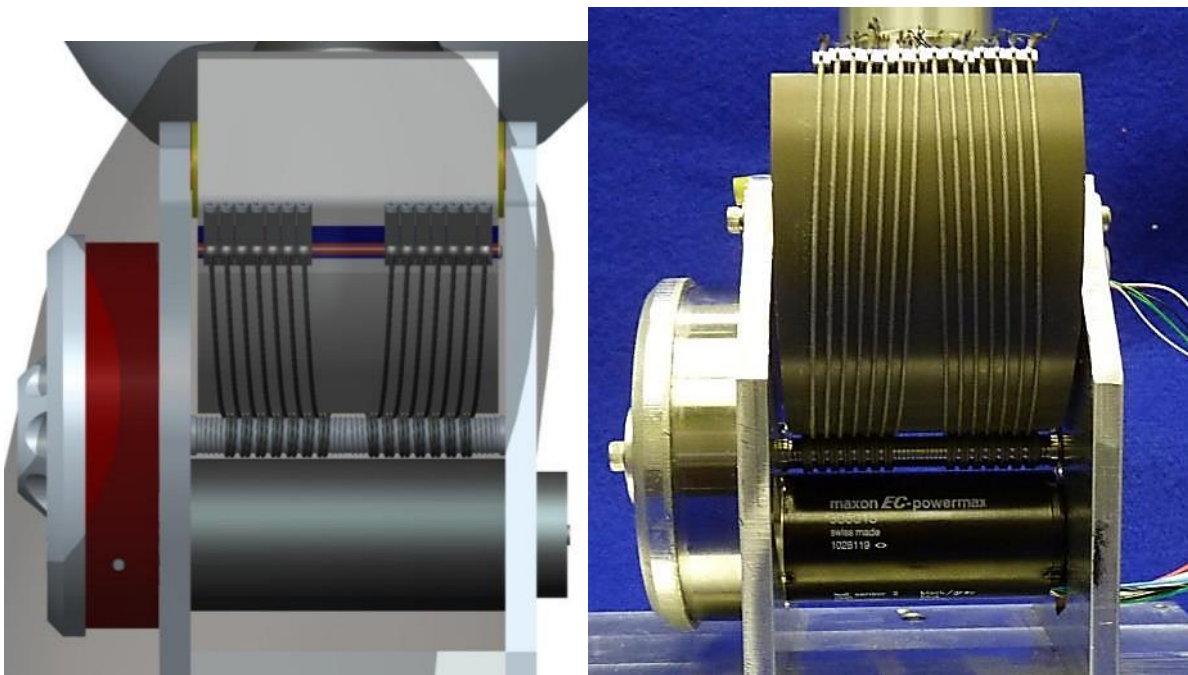


Figure 2-16. CAD model of cable drive and traction drive (left) and photograph of working prototype (right).

For cable termination, a ball with a through hole (Sava Industries) was swaged onto each end as shown in Fig. 16. Custom top and bottom dies were machined from 4140 steel and hardened to about 45 Rc. The dies were placed in an arbor press and used to plastically deform the ball onto the cable. A detail of the

dies can be seen in Fig. 2-17. The bottom die was incorporated into a fixture which was used to exactly set cable length.

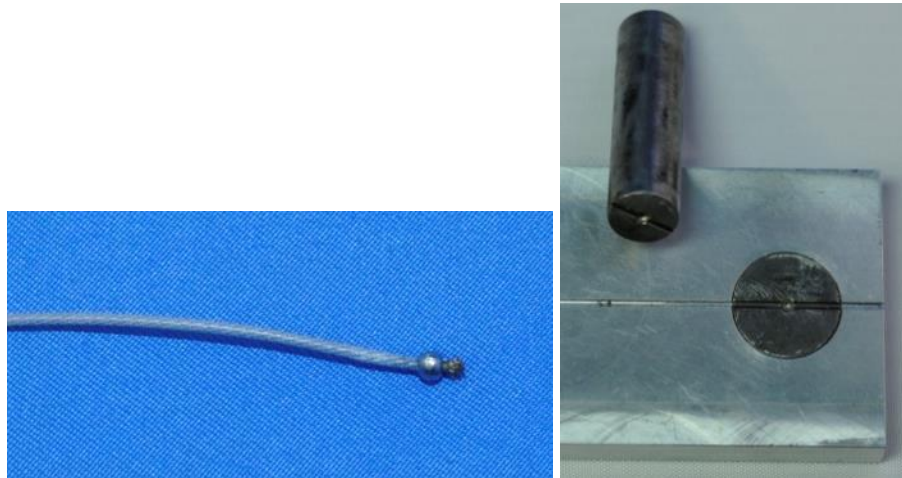


Figure 2-17. Detail of cable termination (left) and top and bottom die (right).

Rocker arm style tensioning beams were used to apply tension to each cable. In one end of the beam, there was a hemispherical depression to seat the ball and a slot for the cable to pass through. The other end had a through hole for a cap screw and the middle of the beam had a semicircular cut to sit on a rod shaped rocker. The cap screw is tightened on one end of the beam which takes up the slack and applies tension to the cable. The entire tension beam assembly sits on a steel insert that dovetails into the aluminum cable wheel, Fig. 2-18.

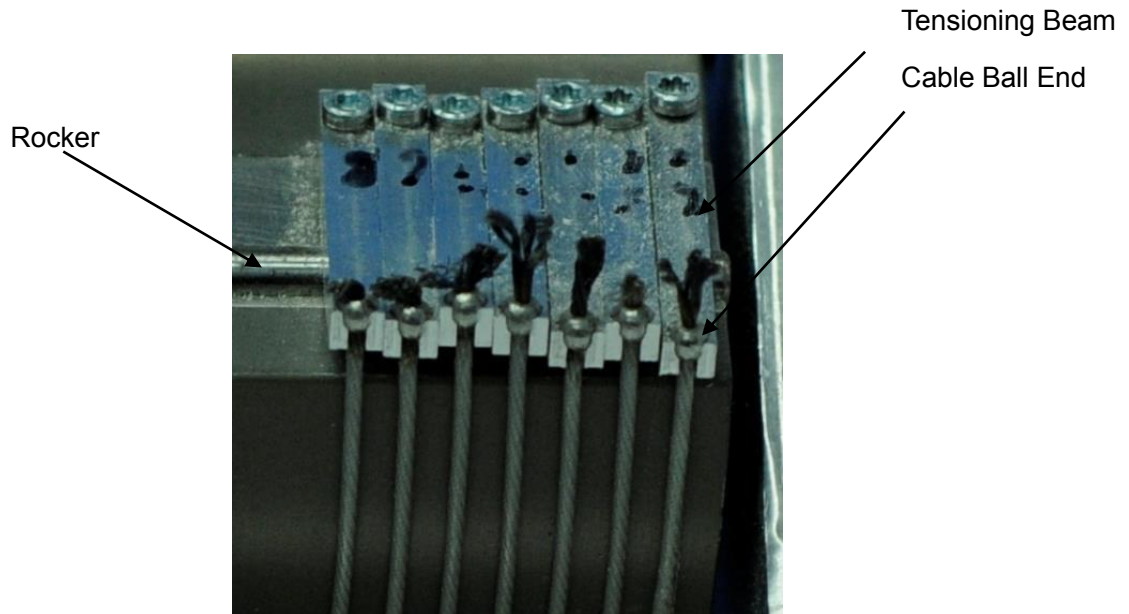


Figure 2-18. Photograph showing close-up view of cable tensioning mechanism and cable termination.

To minimize the friction between the cable and cable wheel so as to maximize the effect of the tensioning beam, the wheel was hard coat anodized and impregnated with Teflon. The holding tension or T_{hold} was calculated using Eytelwien's formula given the torque requirements of the knee. Proceeding from the input shaft to the output wheel, T_{hold} on the input shaft becomes T_{load} on the cable wheel and the holding tension is now applied by the tensioning beams. In this way, the holding tensioning applied by the beams can be thought of as the cable preload. For this design, the cable preload was more difficult to predict. Eytelwien's formula predicted a relatively low preload of about 1 lb. In practice it needed to be much higher to keep the cables from slipping. This was most likely due to several factors. First the coefficient of friction between the cable wheel and cable may have been higher than assumed. Next ϕ or the angle of contact between cable and cable wheel was constantly changing which may have led to some unpredictable behavior. Last the input shaft was dynamically loaded in a fully reversed fashion which may have required significantly more force than calculated.

After it was observed that the preload would need to be higher than calculated, an experiment was conducted to measure the needed preload. One cable was installed between the input shaft and cable wheel. The cable wheel was rotated by hand and torque at the input shaft was measured with a dial indicator type torque wrench. The cable preload was increased via the tensioning beams until the input shaft could sustain one cables worth or 1/14th of the desired torque without slipping. Next the cable preload was determined by measuring the deflection of the tensioning fingers with a custom gauge, Fig. 2-19.



Figure 2-19. CAD model of deflection measurement gauge (left) and gauge in use (right).

The gauge consists of a .0001 inch resolution dial indicator mounted in a custom steel housing with side fingers that touch the beam ends. To use the gauge, it was placed on a flat surface, and the dial was rotated to zero. It was then set onto the deformed tensioning beam and the dial indicated the deflection at the center of the beam relative to the ends.

Next a finite element analysis, Fig. 2-20, was performed to predict the tension in the cable that would cause this deflection. The results of the analysis predicted that about 30 lbs. of tension had been applied to the tensioning beam to cause the measured deflection.

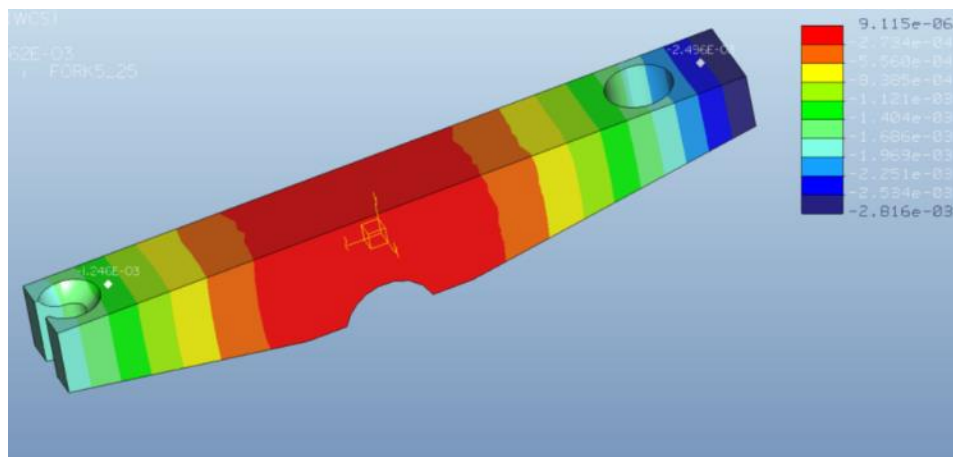


Figure 2-20. FEA analysis showing displacement of tensioning finger.

Setting the tension in the cables was an iterative process that involved installing the cables and tensioning both ends. All cables were installed and set using the measurement gauge. The wheel was rotated back and forth between the hard stops to even out the tension between the two sides of the cable and then they were re-checked and re-tensioned if necessary.

Traction/cable Drive Assembly Testing

The cable and traction drives were assembled and cycle tested through the range of motion or normal walking for approximately 10 minutes. The transmission size is quiet compact at 4.3" wide, 5.25" tall, and 3.75" deep. The transmission exhibited extremely smooth and relatively quiet operation compared to a ball screw design with no visible damage to the cables or traction surfaces.

Conclusions

A novel high ratio 196:1 hybrid traction/cable drive transmission for lower limb powered prostheses was designed and fabricated. Bench top tests were performed in which preliminary traction drive efficiency was measured. Both stages were assembled and cycle testing was performed over the range of motion for walking.

With its preliminary performance, small size and quiet operation, the traction/cable drive could be a viable option for a high ratio transmission for lower limb prosthetics, but extensive testing and possibly redesign would be needed to determine the reliability of the system. Surface fatigue was a concern for the traction drive and 1 and 2 million cycles would need to be done to determine if this would be a problem. Design iterations would be slow as all of the parts must be machined from bearing grade steel and then hardened and precision ground.

Next it was felt that the cables were operating outside of the recommended range since the installed cable tension was more than had been calculated. The cables would need to be cycle tested to find their operational limits.

Given the amount of complexity, time and cost involved in iterating these components, a decision was made to explore more highly characterized transmission components for use in a prosthetic device.

CHAPTER III

Belt, Chain, Chain Transmissions and Parallel Link Load cell Development

Introduction

Several options were considered for the next transmission design. Gears are a natural choice, but the ratio needed for this transmission would require multiple stages and would be heavy. A second consideration was a harmonic drive [35]. These can achieve high transmission ratios in a compact package, but are non back drivable, which is essential for this design. Other more exotic options were briefly considered such as a magnetic transmission from Magnomatics [36]. The transmission promises to produce a high ration in a single stage through contactless magnetic interaction, but the technology is as untested as the traction drive.

Finally multiple combinations of belts and chains were investigated over several months. The belts included trapezoidal and specially shaped curvilinear tooth (GT-2) belts. Additionally, Single and multi-rib v-belts were assessed. Multiple pitch chains were tested including 0.1475", 0.1875", and 0.25". Lastly a hybrid belt called a cable-chain was investigated.

Prototyping and Testing

Bench top tests were carried out in separate knee and ankle assemblies. Three stages were necessary to keep the biggest pulleys smaller because of the lower limit in size on both sprockets and pulleys for the stage inputs. A summary of tested combinations and a brief explanation of the outcomes are detailed in Table 3-1.

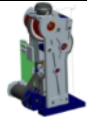
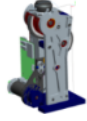
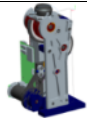
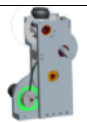
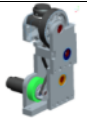


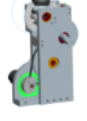
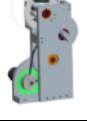
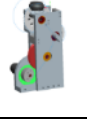
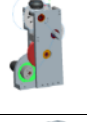

Drive	Stage 1	Stage 2	Stage 3	Comment	CAD
Knee 1)	Single v-belt	.1495" pitch chain	.25" pitch chain	Never implemented due to v-belt slippage in bench top tests	
Knee 1a)	Trapezoidal timing belt	.1495" pitch chain	.25" pitch chain	Excessive audible noise in chain stages due to chain tensioning rollers	
Knee 1b)	Trapezoidal timing belt	.1495" pitch chain	.25" pitch chain	Removed rollers, replaced with eccentric tensioning bushings, still excessive audible noise in chain	
Knee 2)	GT-2 timing belt	GT-2 timing belt	.25" pitch chain	Too much perceived backlash in chain	
Knee 3)	GT-2 timing belt	GT-2 timing belt	GT-2 timing belt	Rapid belt failure under bench top tests	
Ankle 1)	GT-2 timing belt	GT-2 timing belt	GT-2 timing belt	Rapid belt failure under bench top tests	
Ankle 1a)	GT-2 timing belt	.1475" pitch chain	.25" pitch chain	Stage 1 belt slippage	
Knee 2b)	.1475" pitch chain	N/A	N/A	Excessive audible noise	
Knee 2c)	cable chain	N/A	N/A	Rapid failure under bench top tests	
Knee 2d)	Double v-belt	.1495" pitch chain	.25" pitch chain	Quietest to date, unacceptable chain, sprocket wear	
Knee 2c)	Double v-belt	.1875" pitch chain	.25" pitch chain	3 hour operation in bench top tests	
Ankle 1b)	Double v-belt	.1875" pitch chain	.25" pitch chain	7 tooth sprocket tested on stage 1	

Table 3-1. Summary of bench top Belt Chain tests.

All drives started with a Maxon EC 30 motor as before. In each test, the drive was first run with no load in a fully reversed sinusoidal motion at high speed to access the noise levels. If the noise was acceptable, the drive combination was tested under a load equivalent the maximum forces the drive would experience during walking, Fig. 3-1.



Figure 3-1. Inverted ankle assembly bench top testing setup.

The combination that showed the most promise for low noise and high durability was a first stage two rib Polyflex JB v-belt (Gates Corp.), second stage 0.1875" pitch chain (U.S. Tsubaki), and third stage 0.25" pitch chain (Diamond Chain). A CAD model of the assembled knee and ankle using these components is shown in Fig. 3-2. The knee had a transmission ratio of $\sim 138:1$. The first stage had a ratio of 5:1, the second 6.2:1, and the last 4.4:1. The ankle had a ratio of $\sim 178:1$, with the first stage at 5:1, the second at 8:1, and the last 4.4:1.

In each assembly, the v-belt smaller pulley is affixed directly to the motor shaft. The second stage smaller chain sprocket is coupled to the first stage larger pulley and the last stage smaller chain sprocket is connected to the third stage sprocket. Sprockets and pulleys are suspended between two side plates that are bolted to each other through spacers that hold them apart. Additionally bearings that hold the shafts of the rotating components are held in eccentric mounts within the side plates. Eccentric mounts are used to take up the slack in the belts and chains to minimize backlash.

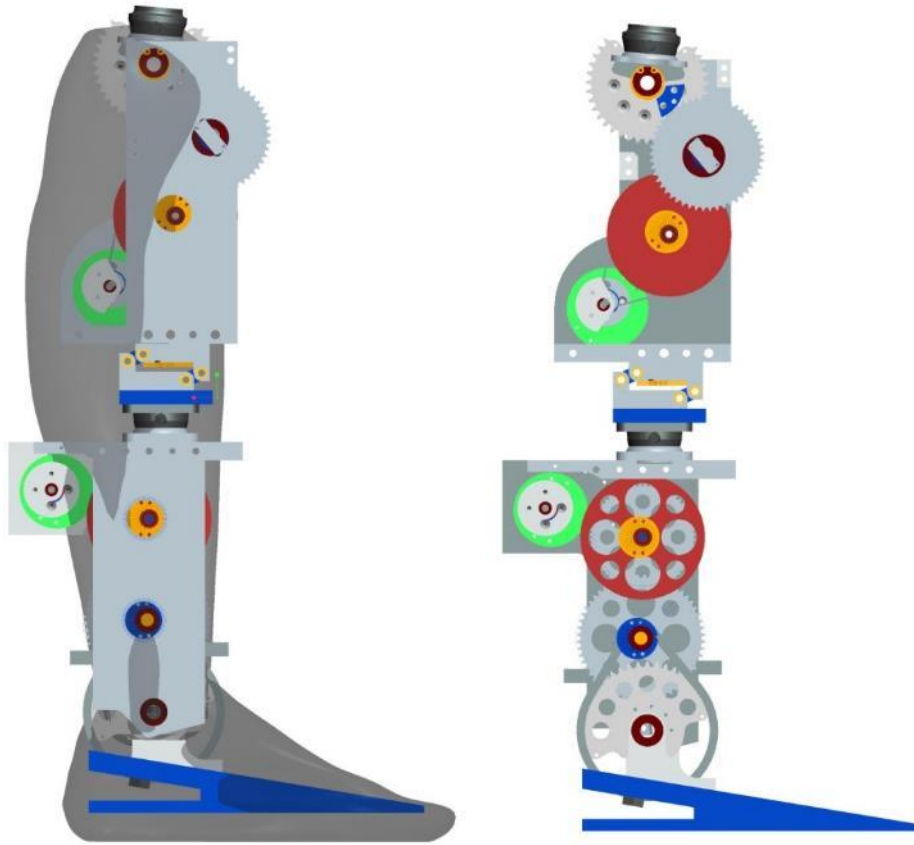


Figure 3-2. CAD models of first prototype belt-chain-chain leg shown inside the anatomical envelope (left) and without covers right showing the drive train (right).

The prototype knee and ankle assemblies were connected together into a full proof of concept knee and ankle leg prototype and a carbon fiber foot (Freedom Innovations) was attached to the bottom of the ankle, Fig 3-3.

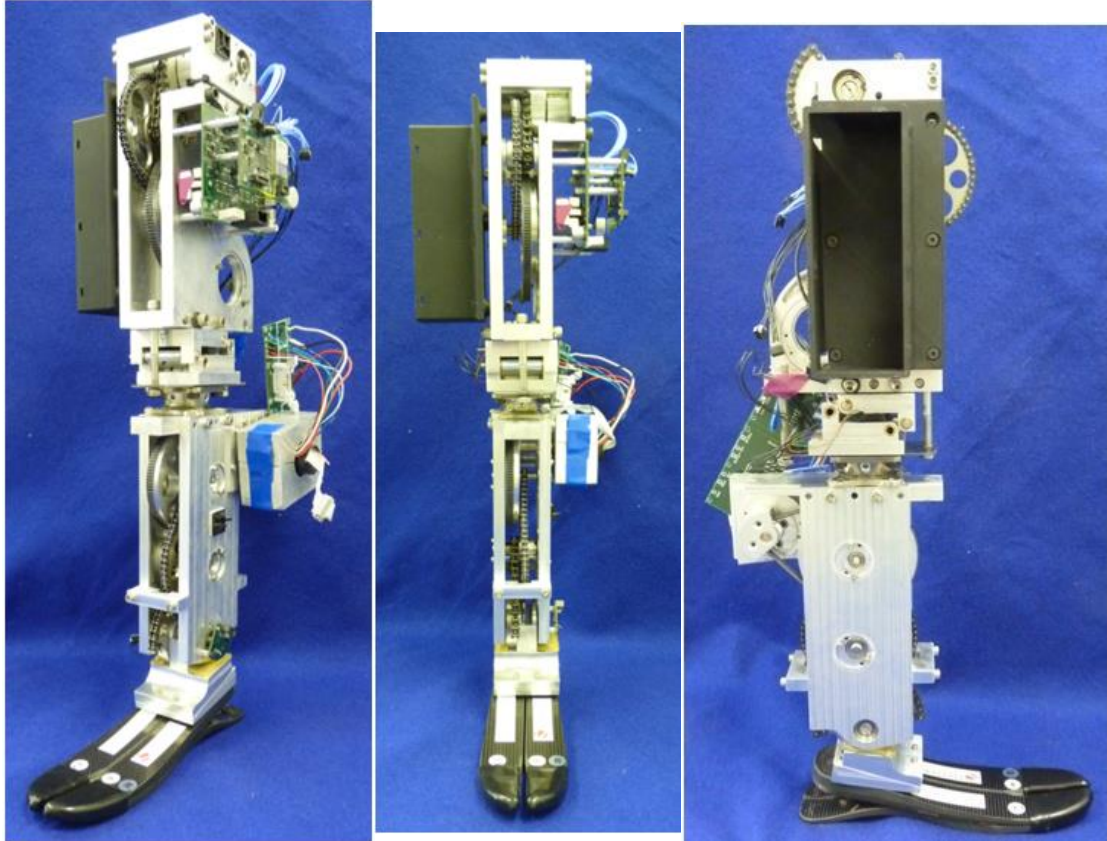


Figure 3-3. Photographs of assembled leg prototype.

A battery compartment can be seen on the right side of the far right picture and control electronics can be seen on the left side of the leg in the far left picture. A parallel link load cell can be seen connecting the knee and ankle and will be described in more detail in a subsequent section. A non contact Hall Effect magnetic encoder (Austria Microsystems) was used to sense knee and ankle joint position. Note that the final weight of the leg was too heavy (~12.5 lbs) for an amputee to walk on. Also the transmission ratio was lower than desired since commercial sprockets were used and only available with a minimum number of 9 teeth for the larger chain.

Load cell

The previous leg design incorporated a sensorized prosthetic foot to measure ground contact as shown in Fig. 3-4 [22]. Ground contact information is used during state transitions and during ground adaptation. This foot used strain gages to measure the bending strain caused by toe and heel load.

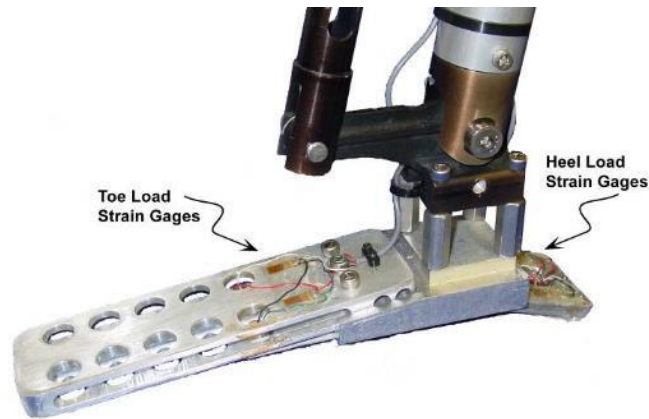


Figure 3-4. Sensorized prosthetic foot.

Since two of the stated goals of the leg redesign were to eliminate wires that crossed over joints and simplify sensor design a new load cell design was needed. It was proposed to put the load cell between the modular knee and ankle portions of the new leg design. The challenge of the mechanical design is to build a sensor that measures only the axial force imparted to the leg by ground contact while mechanically “filtering” out bending moments.

One approach is to use mechanical flexures that have a high stiffness in the direction of the bending moment and relatively low stiffness in the direction of the axial force. The author designed such a load cell that was incorporated in a previous knee only design described by Fite et al, [21]. This load cell was quite heavy at 300 gm (.6 lbs), and vertically too tall.

A lighter more compact load cell was proposed that could be placed between the ankle and knee portions of the leg. Instead of flexures, this design uses a four bar mechanism to ensure that two plates stay parallel to each other regardless of the forces applied to them. Referring to Fig. 3-5,a neodymium magnet is imbedded in the Load Cell Top which is connected to the knee and a Hall effect sensor (Austria Microelectronics) is embedded in the Load Cell Bottom which is connected to the ankle. A compliant urethane spacer is sandwiched between the two plates. Connecting links hold the top and bottom together via connecting pins that rotate within bronze bushings.

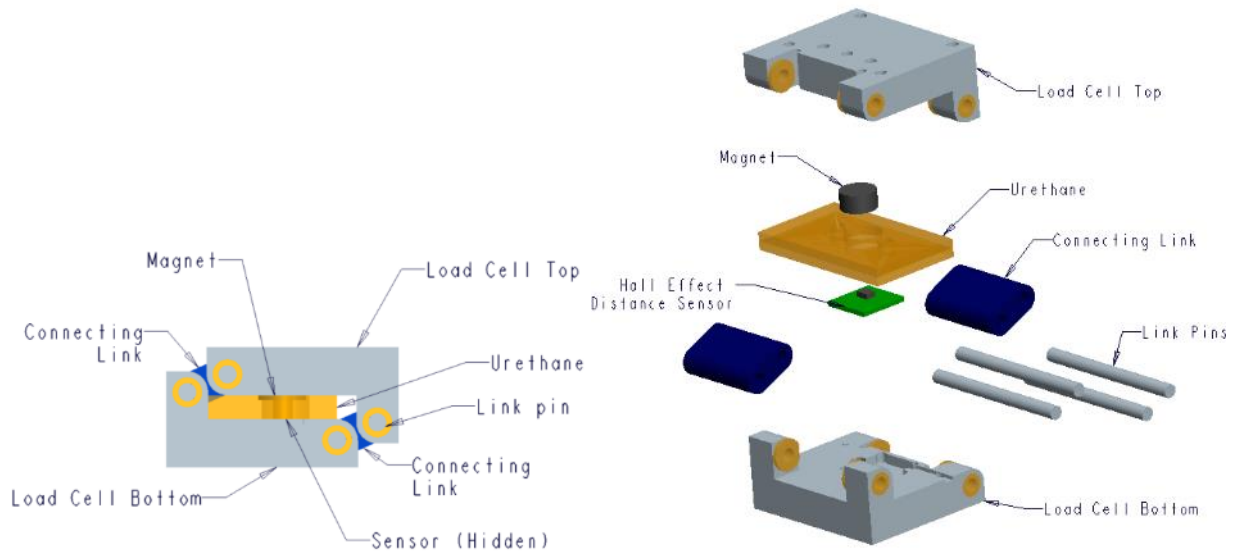


Figure 3-5. CAD models of load cell showing a side view (left) and exploded view (right).

Operation of the load cell is shown in Fig. 3-6. When a force is applied between the two plates, it will result in movement between the plates. A pure moment load such as would be seen at heel strike or toe off, would produce no movement, but would result in tension and compression loads in the two connecting links. Note that this load is directly proportional to the distance between the two connecting links, so if the distance is increased the forces would decrease.

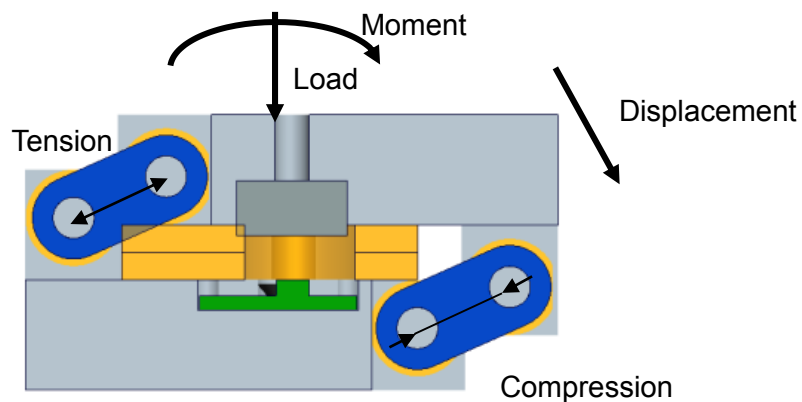


Figure 3-6. Cross sectional view of load cell showing operation.

A bench top load cell, Fig.3-7, was manufactured and assembled. Loads were applied to the load cell at the centerline, at a moment arm of 3 inches and 9 inches, approximately simulating ground contact at heel strike and toe off. Repeatable results were achieved after several iterations of magnet type, urethane hardness and magnet to sensor spacing. One problem that was noted was that there was a significant amount of static friction in the joints when a load was applied at a large moment arm. As a result a higher

load was needed to move the load cell at greater distances from the center. This is because of the aforementioned tension/compression load in the connecting links and the resulting high bearing load between the connecting links and link pins. This load cell was included in the proof of concept design of the belt-chain-chain leg described above.

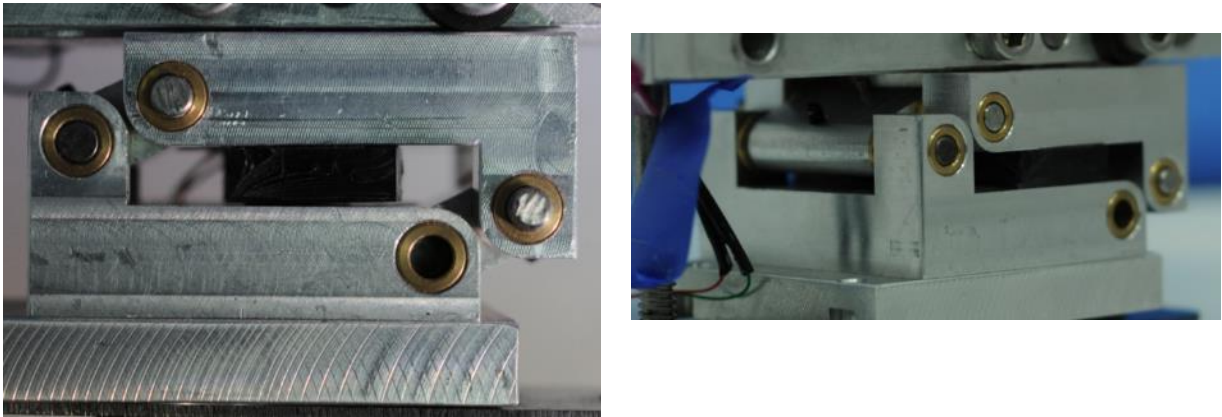


Figure 3-7. Side and isometric views of experimental test load cell.

Conclusions

The prototype leg and load cell designs showed enough promise to pick this configuration for further development. The design survived ~ 3 hours of simulated walking loads during bench top testing and was relatively quiet, but there were several issues in the prototype that would need to be remedied in the next version. The sprockets used were what was available commercially and were not of hardened steel so tooth wear was an issue during testing. The sprockets were also larger than desirable so transmission ration was too high. The prototype was too heavy to be used and the load cell design needed to be refined.

CHAPTER IV

Generation 2.0 Transfemoral Prosthesis

Introduction

Two subsequent versions of the belt-chain-chain leg were designed using all of the lessons learned from the first prototype. For brevity, one description will serve for both versions. The main differences were that the second version was lighter than the first ~9.2 lbs vs. ~9.7 lbs and the addition of a spring foot to the second version which will be described on more detail in a subsequent section.

There were several major design improvements between these versions and the prototype version. The side plates were replaced with machined structural shells that fully enclosed all of the drive components and fit together with a locating lip. Next custom sprockets were machined from 4140 steel and the teeth were flame hardened for better wear resistance. The parallel link load cell was incorporated into the structure. An eccentric mount for the motor was extended for better heat sink capacity. The drive train components were also positioned to better conform to the anatomical envelope. CAD models of the next version of the leg can be seen in Fig. 4-1.

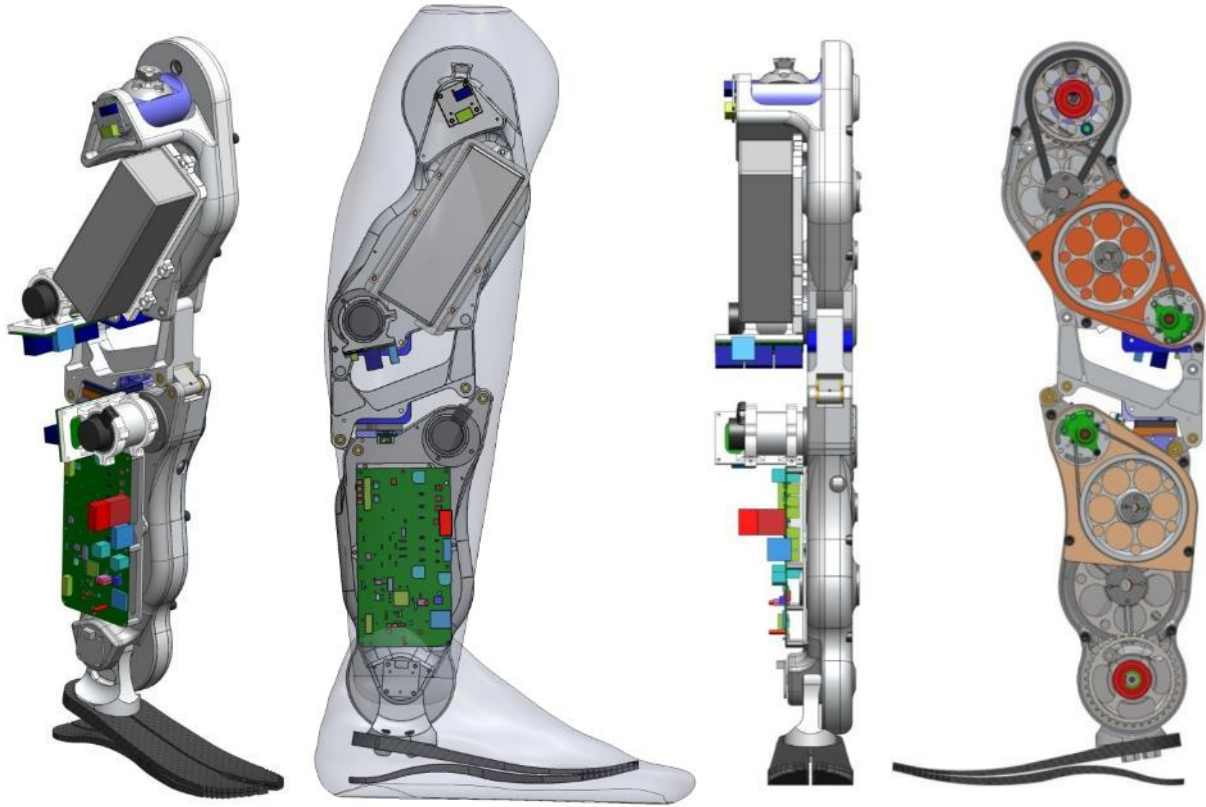


Figure 4-1. Isometric, right (showing 90% male anatomical envelope), front and left side (with covers hidden) views of leg.

Prosthesis Design

By machining custom sprockets instead of relying on commercially available sprockets, the transmission ratios of the knee and ankle were increased. The knee had a transmission ratio of $\sim 179:1$. The first stage had a ratio of $5:1$, the second $7.1:1$, and the last $5:1$. The ankle had a ratio of $200:1$, with the first stage at $5:1$, the second with $8:1$, and the last $5:1$. Details of the ankle drive train with and without belt and chains can be seen in Fig.4-2.

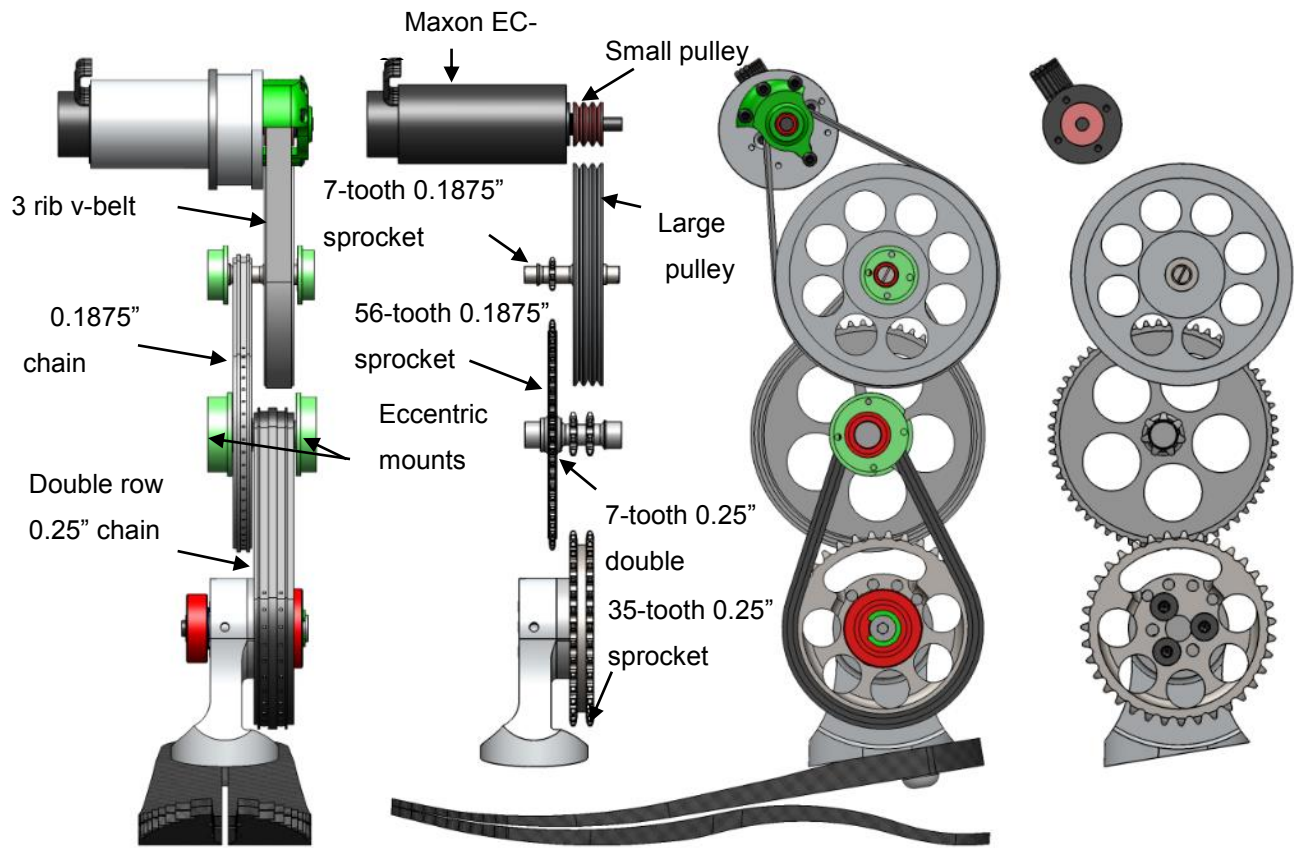


Figure 4-2. Front and left side views of the ankle drive train with and without belt and chains.

For added reliability the two rib v-belt of the initial prototype was replaced with a three rib v-belt (Gates Corp.). The second stage chain is 0.1875" pitch chain from U.S. Tsubaki. After analysis, it was determined that the last stage 0.25" pitch chain was stressed past its design limit, so it was upgraded from a one row to a two row chain from U.S. Tsubaki. High strength 4041 steel was used for sprockets and the teeth were flame hardened for durability on all 7 tooth sprockets. Final drive sprockets were also machined with a curved slot that has an arc equal to the range of motion. A pin with a rubber bushing passes through the slot and is trapped in pockets in the shell halves to serve as a hard stop. The shafts that support the final drive sprockets have a neodymium magnet embedded in one end for the Hall effect sensors. As with the prototype, eccentric mounts hold the bearings within the side shells and when rotated, tension the chains and take out backlash. Bearings were a minimum ABEC class 5 and were sized appropriately to withstand the maximum forces that would be imparted by the transmission components with a minimum safety factor greater than 1.5 for dynamic radial load capacity load. For noise reduction, sets of bearings are preloaded together using outer race bearing springs from Smalley Steel Ring. A picture of the ankle drive train in the ankle housing can be seen in Fig. 4-3. The upper half of the 0.1875" pitch chain is obscured by an internal black colored shield that keeps chain grease from contacting the belt.

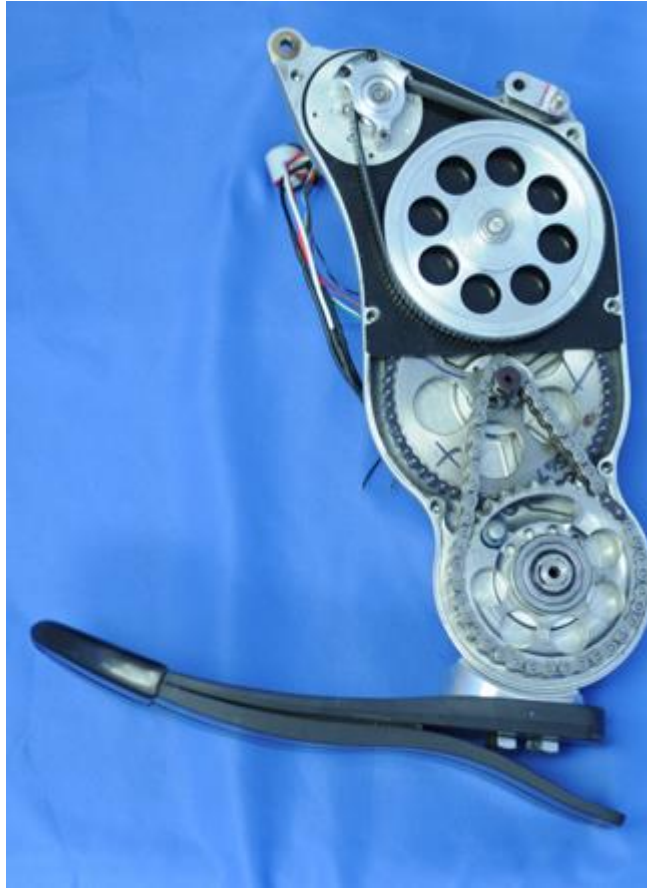


Figure 4-3. Ankle drive train.

Analysis

Target weight for this leg was less than 10 lbs. which is less than the weight of the amputated limb. It is necessary to keep the weight of the prosthetic as light as possible because connection to the residual limb is via vacuum socket and can become loosened by a heavy prosthetic or high inertial load. To minimize the weight, high strength 7075 aluminum was used extensively throughout the leg for the structural components and lightening holes were added to steel sprockets wherever possible. Hand calculations were performed on parts with simple geometries and finite element analysis was conducted on more complex parts to ensure a safety factor of at least 1.8 and to find areas where parts had been overdesigned. Fig. 4-4 shows an example analysis done on a sprocket.

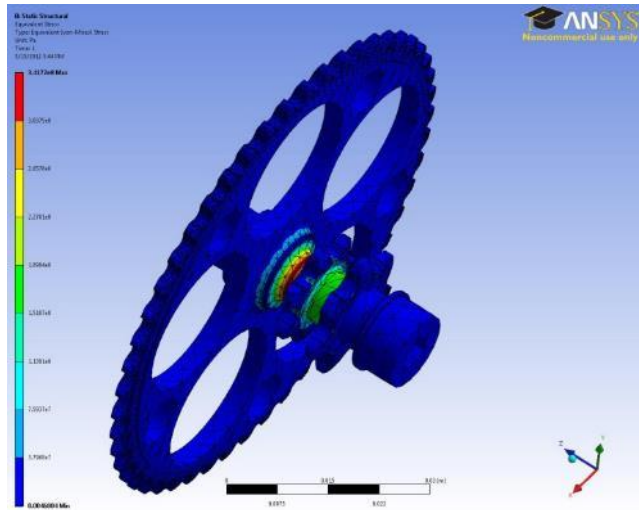


Figure 4-4. Finite element analysis of sprocket.

. The results of the finite element analysis suggested several areas where material could be removed to save weight and also places where material needed to be added to increase the safety factor. The knee lateral shell was one such part where the results of the FEA had a large effect on the final shape of the part. The process of applying the loads, generating the mesh and analyzing stresses are shown in Fig. 4-5.

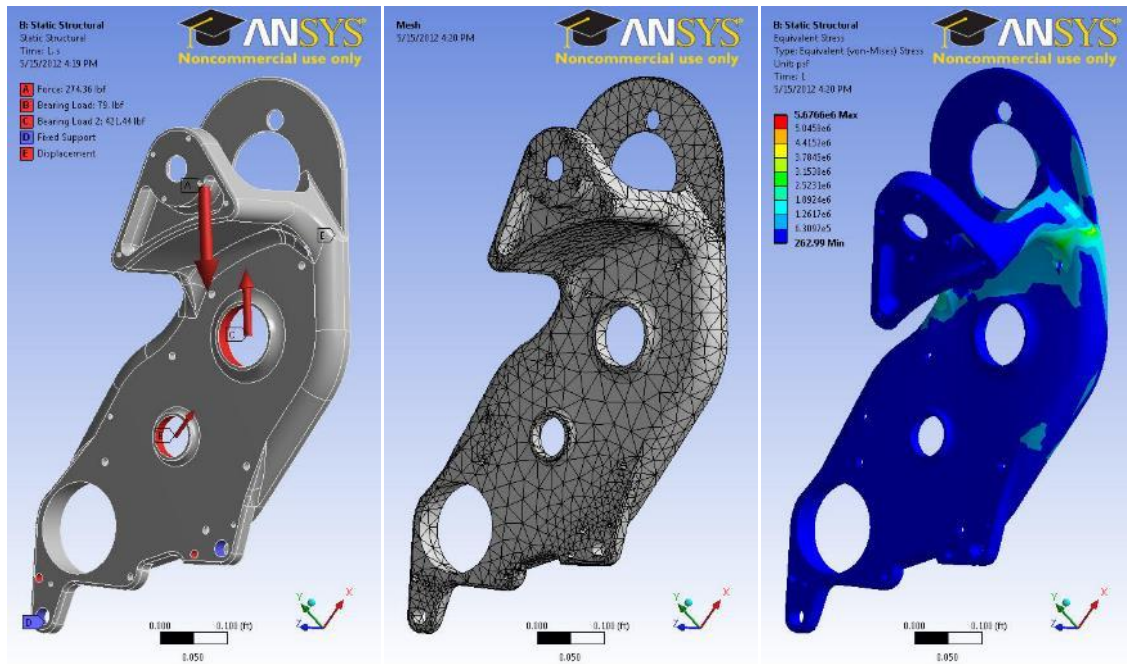


Figure 4-5. Finite element analysis of knee Lateral shell showing applied loads (left) finite element mesh (center) and von-Mises stress (right)

Assembly

The leg is put together by first assembling the eccentric mounts and bearings into the structural shell halves. Next, drive train components including chains, sprockets, and an internal shield are assembled and dropped into one half of the shell, Fig 4-6.

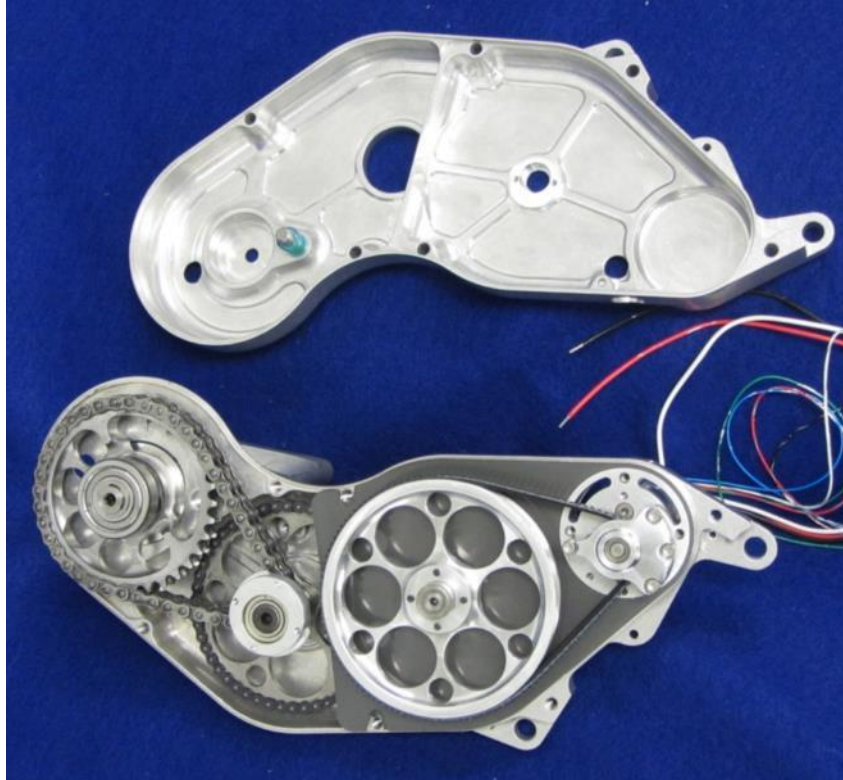


Figure 4-6. Shell halves with drive train installed.

Next the belt is installed and the two shells are mated together. After the two sides are bolted together the chains are tensioned by rotating the eccentric mounts which moves the sprocket centers apart. Simultaneous rotation is achieved by with a special tool, Fig. 4-7, that connects the eccentric mounts. Chain tension is assessed by checking the relative backlash between adjacent sprockets. Eccentric mounts are locked into place with external locking screws.

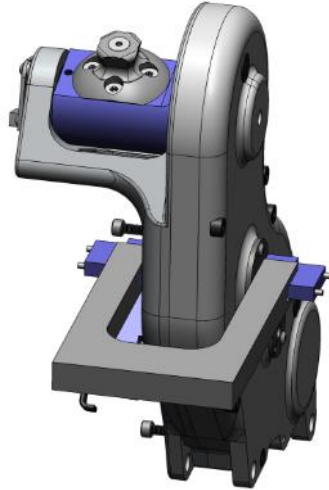


Figure 4-7. Knee assembly with eccentric timing tool.

Next the belt is tensioned by rotating the motor which is mounted in an eccentric housing. Tension is assessed by plucking the belt like a guitar string and measuring the frequency of vibration using a sonic tension meter (Gates Corp), Fig. 4-8. When the tension has been set, the motor is held into place with locking screws.



Figure 4-8. Sonic tension meter.

Once the knee and ankle are assembled the load cell is coupled to the ankle assembly. The load cell will be described in more in a later section. At this point they can be coupled together directly for the shortest configuration or a spacer can be added to make the leg as tall as necessary. CAD models of the short (50% female) and tall (90% male) configurations are shown in Fig. 4-9. Note that the spring foot is shown in this model and will be described in more detail in a subsequent section.

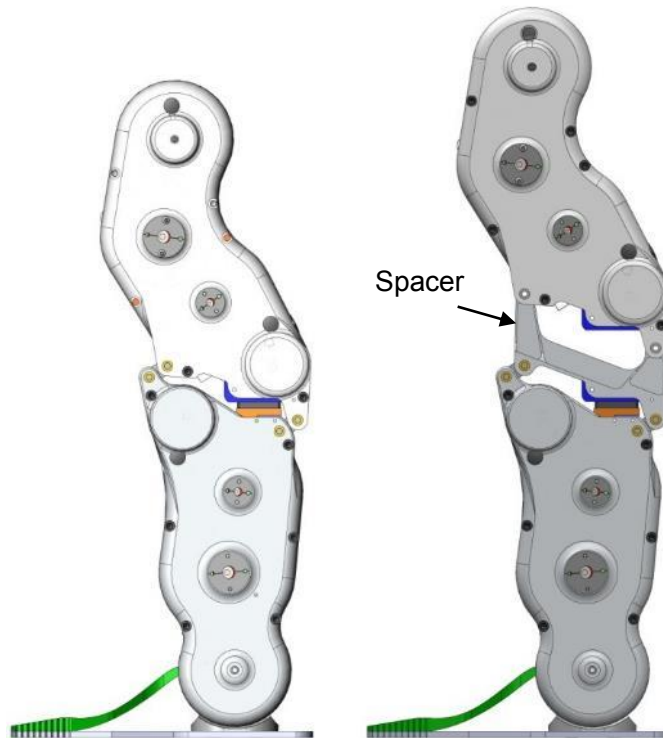


Figure 4-9. Leg with and without spacer.

Once the knee and ankle are assembled, the electronics and battery are attached to the right sides of the ankle and knee respectively Fig. 4-10. Hall effect magnetic rotary position sensors are attached to the right side of the leg at the knee and ankle joints. Last the foot is attached at the bottom of the ankle.

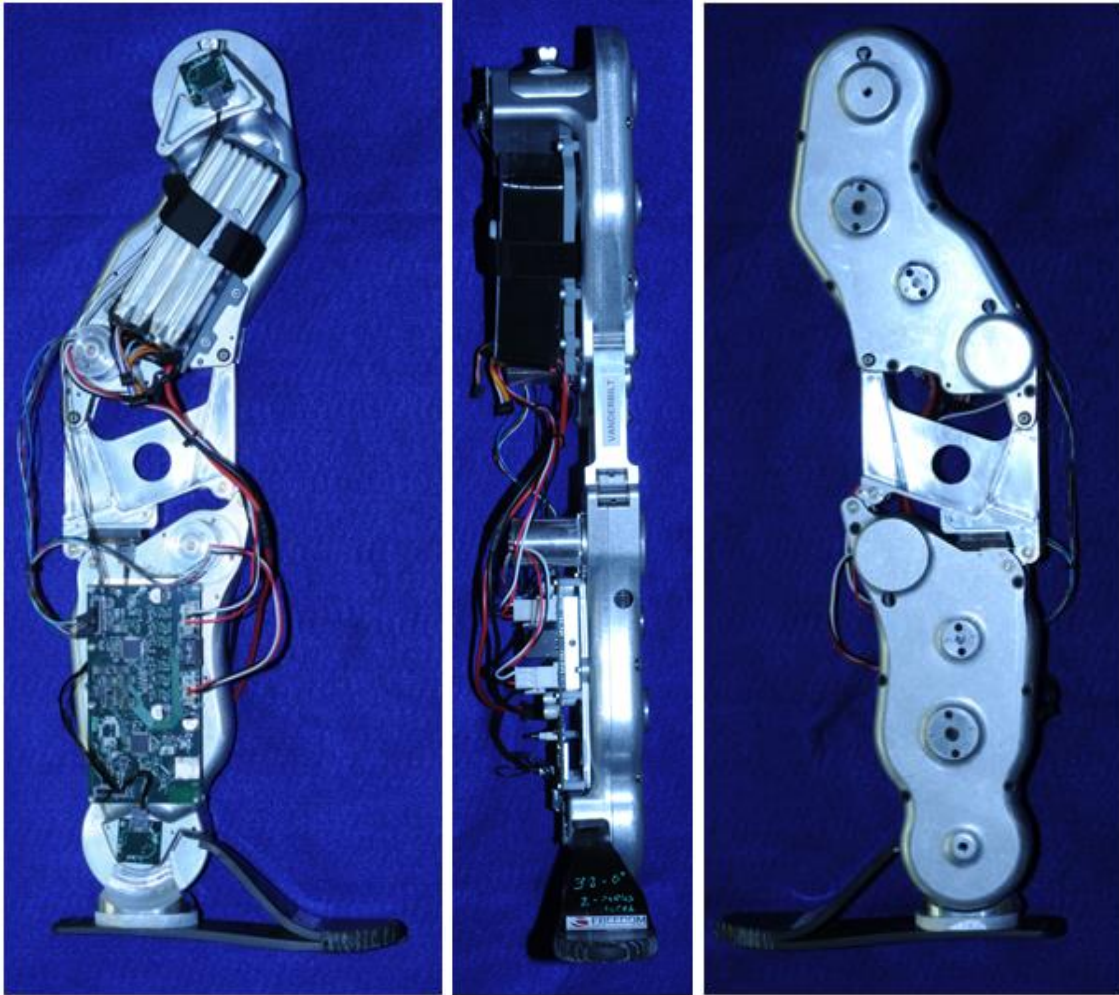


Figure 4-10. Right, front and left side views of leg.

Load Cell

As stated previously the load cell design showed promise but had problems with static friction arising from the high tension and compression forces in the connecting links. The load cell was also a standalone unit and so was taller than necessary. In the new design, the top and bottom parallel links were incorporated into the structure of the knee and ankle assemblies as shown in Fig. 4-11.

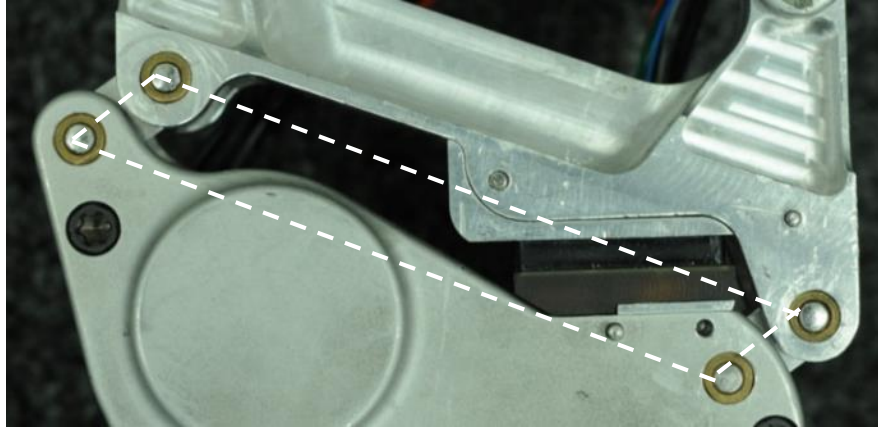


Figure 4-11. Detail view of load cell incorporated into leg housing. Parallel linkages are shown in dashed white lines.

The top and bottom links were also rotated down at the back of the leg to more closely follow the outline of the internal components so as to add a minimal amount to the build height. In addition, the distance between the connecting links was increased to decrease the tension and compression forces in them and thus reduce the bearing loads and static friction. The load cell Top and Bottom which hold the magnet and magnetic sensor respectively were made into separate components from the top and bottom links to make those parts easier to manufacture, Fig 4-12.

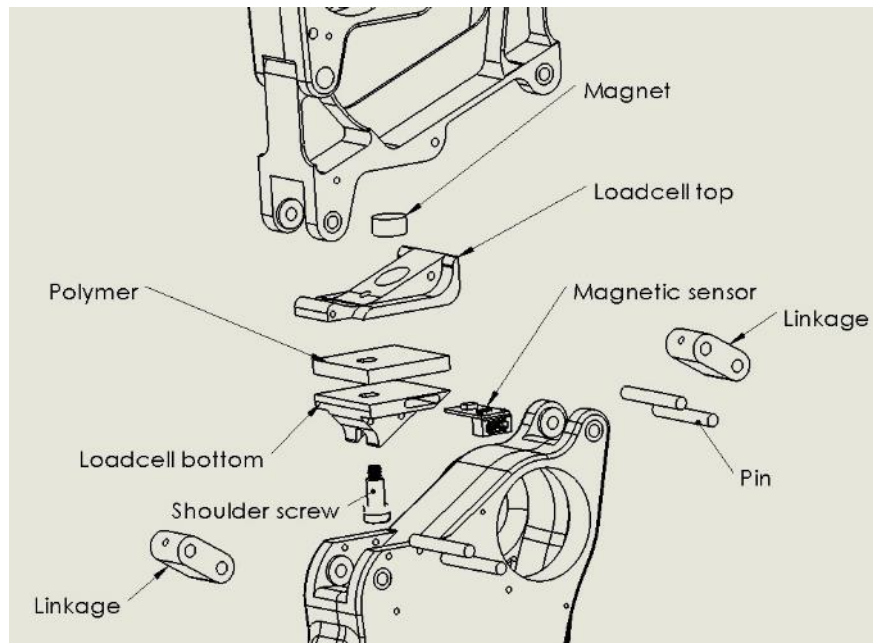


Figure 4-12. Exploded view of load cell included in belt-chain-chain leg.

A shoulder screw was added to hold the load cell together and provide preload between the two halves. Just as with the first parallel link load cell, this design took several iterations to find the right stiffness polymer, magnet type and magnet spacing away from the magnetic sensor. After those variables were finalized, the load cell has been used for several thousand strides with no issues.

Spring Foot

For level ground walking almost all of the ankle torque is in plantarflexion (with the toe rotating down). The Vanderbilt transfemoral ball screw knee and ankle prosthesis had a integrated spring in line with the ankle ball screw, Fig. 4-13 to bias the effective motor torque in that direction thus decreasing the maximum motor torque required (or the maximum transmission ratio with a given motor). The spring stored energy just before and released energy during push off. The spring engages at about 5 degrees of dorsiflexion.



Figure 4-13. The powered tethered prototype.

This type of coil biasing spring design is obviously not possible with the above described transmissions. A carbon fiber reinforced polymer (CFRP) leaf spring acting in parallel was proposed as a possible alternative to the steel ball screw. The leaf spring design is commonly used in prosthetic foot designs for energy return at push off and energy absorption at heel strike. A CFRP leaf spring would be lighter than a steel spring and could possibly be designed to have a longer fatigue life than the steel spring which becomes permanently deformed after several thousand cycles. It would also presumably be easier to incorporate the spring into the foot design since prosthetic feet are predominantly made from CFRP. Additionally including the spring into the foot would allow for the spring to be easily changed out providing a different spring rate. Fig. 4-14 shows a CAD rendering of the spring foot design concept attached to the ankle assembly. The design consists of a sole plate rigidly attached to the leaf spring at the toe by Kevlar thread wraps. The sole plate is bolted to the foot adapter part which rotates about the ankle joint center.

The spring contacts a plastic ultra high molecular weight polymer (UHMW) bumper that is inserted into a boss on the ankle lateral plate.

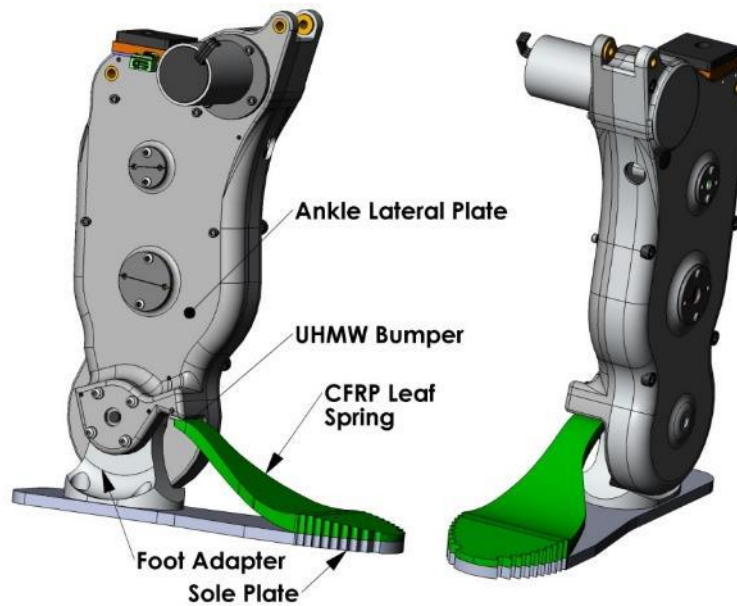


Figure 4-14. CAD rendering of spring foot design and ankle assembly.

Spring operation is shown in Fig. 4-15. The foot is seen plantarflexed (left) with the spring free and uncompressed. Contact occurs when the ankle is at a neutral position (center) and is fully compressed in maximum dorsiflexion (right).

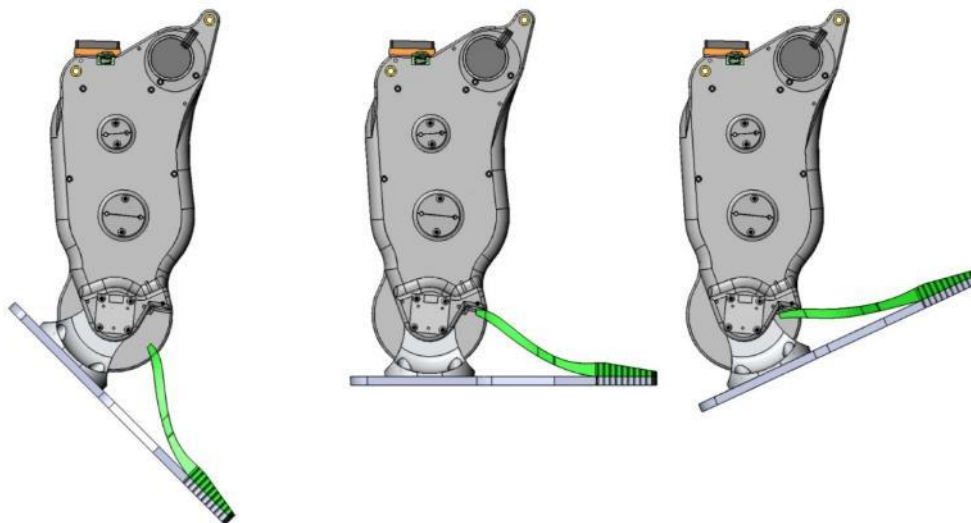


Figure 4-15. CAD model showing spring foot shown in plantarflexion (left), neutral (center), and dorsiflexion (right).

The next step was to design the spring to have the appropriate stiffness. For level ground walking where maximum dorsiflexion is about 7 degrees, optimum torsional stiffness ideally would be about 8 N-m/deg. with an engagement at zero degrees. For upslope walking or standing facing up a hill this stiffness would be too high. A torsional stiffness of 4 N-m/deg. was chosen as a compromise between the two conditions. Fig. 4-16 shows ankle angle vs. ankle torque for fast level ground walking and the reduction in torque that would occur by adding a parallel spring with 4 N-m/deg of stiffness.

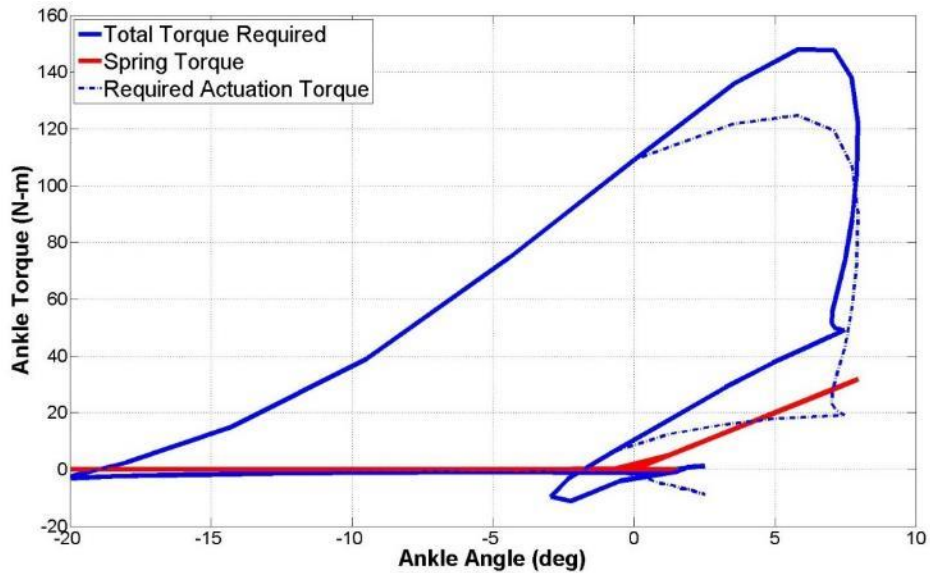


Figure 4-16. The reduction in ankle torque required by the transmission by the addition of a spring in parallel for fast walking taken from averaged normal biomechanical data [3].

The next step was to determine an equivalent linear spring stiffness for the leaf spring. Referring to Fig. 4-17, the joint lever arm is .04 meters.

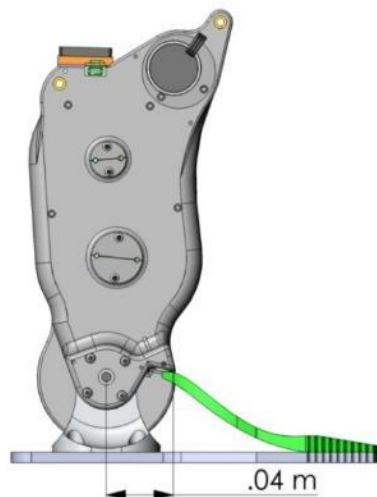


Figure 4-17. CAD model of ankle showing leaf spring-ankle moment arm.

For every degree of rotation, the force exerted at the tip of the spring on the UHMW insert is:

$$\frac{4 N - m}{deg} \times \frac{1 deg}{.04 m} = 100 N$$

The linear travel of the spring is given by:

$$\delta \cong r\phi$$

And for every degree of rotation, the tip of the spring travels approximately:

$$\delta \cong .04 m \times \left(\frac{1 deg \times \pi rad}{180 deg} \right) = .0007 m$$

Dividing the force by the displacement gives an equivalent linear spring stiffness of:

$$K = \frac{100 N}{.0007 m} = 142,857 N/m$$

Several iterations of the spring were designed and analyzed using FEA software to give the desired spring stiffness and remove stress concentrations. The modulus of elasticity for CFRP can change significantly based on the direction that the fibers are layered during assembly and it is difficult to find published data. For this analysis a modulus of 34000 MPa was used based on data published for use in the leaf spring of an automotive suspension [37]. Fig. 4-18 shows FEA stress and deflection results.

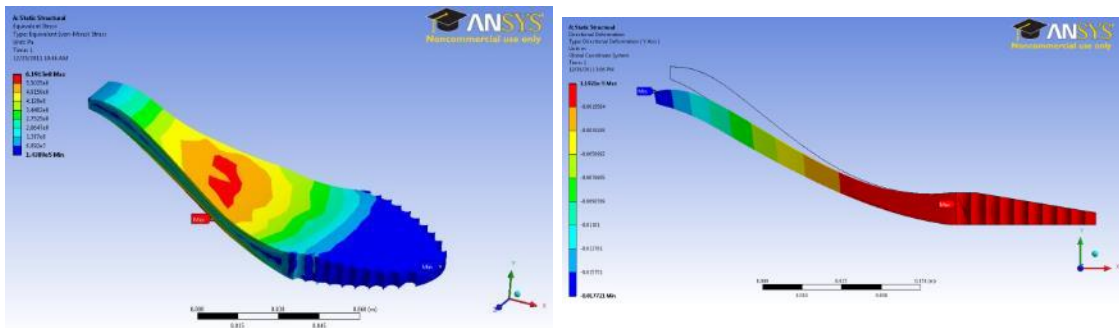


Figure 4-18. FEA analysis of spring foot showing von Mises stress (left) and maximum deflection (right).

A plot of force vs. deflection of the spring is shown in Fig. 4-19. The analysis predicted a linear spring stiffness of 141,076 N/m which is within 2% of the target stiffness.

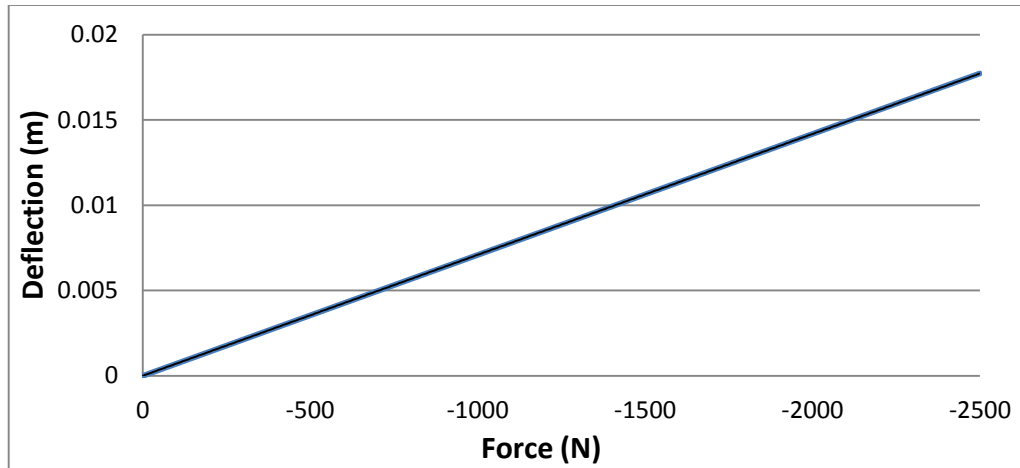


Figure 4-19. FEA prediction of force vs. deflection of the spring of CFRP leaf spring.

A CFRP foot (Fig. 4-20) was manufactured according to specifications by Freedom Innovations who is a leader CFRP prosthetic foot design.



Figure 4-20. Picture of spring foot.

The foot was attached to the ankle and has been tested during walking. Preliminary experiments were inconclusive because high levels of friction between the leaf spring and UHMW bumper made parameter tuning difficult. Solving this problem is proposed in the future work section below.

Conclusions

The goal of this work was to redesign a transfemoral prosthesis to make it more commercially viable. To accomplish this, new transmission, ground contact load cell and motor torque reducing/biasing spring designs were developed. The designs were incorporated into a new prosthetic leg and a total of five legs have been assembled and successfully tested. The leg with the most use is one worn by our test subject who is a unilateral transfemoral amputee six years post amputation Fig. 4-21.



Figure 4-21. Test subject wearing belt-chain-chain leg.

Testing has included more than one hundred hours of operation and over 50,000 steps with no major mechanical problems. The testing regime has encompassed walking, running and stair ascent and descent. The new leg is appreciably quieter than the ball screw leg at ~60dB as opposed to ~75. It also fits inside the anatomical envelope more tightly. The new leg is modular with the transmission of each being completely shielded within its own housing. Height can be adjusted from a 50 percentile female height upwards by the addition of spacers. Sensors have been removed from the foot and all contact rotary position sensors have been changed to noncontact to increase reliability. A biasing spring foot has been designed to replace the steel spring design of the ball screw leg, although problems with friction still need to be resolved. A novel parallel link load cell has been developed to sense ground contact. Lastly, the largest indication that the leg has the potential to be a commercial product is that it has been licensed by a commercial partner who is well known in the lower limb prosthetics industry.

CHAPTER V

Generation 3 Transfemoral and Transtibial Prostheses

Introduction

The Gen 2.0 design described in Chapter IV proved that the combination of belts and chains allowed for a more modular, reliable, and quiet design. In addition it allowed for more flexibility to place joint centers and shape the transmission to more closely resemble the anatomical envelope. The four bar parallelogram load cell was a viable design idea to sense load and not moment and therefore obviate the necessity of a sensorized foot. The carbon fiber leaf spring foot showed promise promised to replace the parallel coil spring, although problems with friction kept it from being fully tested. Although the design was successful in proving new ideas, it needed addition refinement to make it into a pre commercial product.

The next design iterations aimed to take make the design into a pre commercial product by focusing on five areas. First it was desirable to have a truly modular design such that standard prosthetic components could be used between the knee and ankle units for adjustability or so the ankle can be used as a transtibial prosthetic. In addition, a standalone transtibial prosthesis will need to be much shorter compared to the Gen 2.0 design for accommodate longer residual limbs. Secondly the sensors needed to be enclosed. Third the friction in the spring foot needed to be eliminated to make it useable. Fourth, the parallel link load cell had a few undesirable characteristics that needed to be eliminated such as non-repeatability and hysteresis due to creep in the elastomeric rubber spring element and stiction in the bronze bushings. Additionally, its motion was not parallel with the axis of the leg, which was hypothesis may feel unnatural to the user. Furthermore, the old load cell was integrated into the knee and ankle transmission housings and thus could not be modified easily. It would be better to have a modular load cell which could be swapped out if a different stiffness was needed or a new design was developed. Last, the battery and electronics needed to be fully enclosed.

This chapter will briefly describe the design of a transtibial prosthesis which addressed the first three issues, namely modularity, sensors and spring foot. Next a modular load cell which will be described which addresses the issues of non-repeatability, hysteresis, and non-linear motion. Last, the design of a transfemoral prosthesis will be presented which addresses the issue of enclosing the battery and electronics.

The design presented here is essentially the same as the previous in terms of components, structure, assembly and analysis, therefore this chapter will be less detailed than the previous and will highlight the main differences with, and additions to the Gen 2.0 design.

Finally results of transmission characterization measurements will be presented. Several tests were performed to measure the range of stiffness and damping that each joint could emulate and each joint was commanded with a torque step to access open loop torque tracking.

Generation 3.0 Transtibial Prosthesis

A transtibial prosthesis was designed using the same belt, chain, chain configuration described in Chapter IV, but there were two major differences. First, the first and last stages of transmission were arranged in a folded configuration instead of a linear arrangement as before. A shorter design allows for more adjustability between a knee and ankle unit and for a longer residual shank. Next the transmission ratio was reduced from 200:1 to 143:1 to make the package smaller. Additionally larger bearings were employed in the ankle joint to allow the angular position sensor to be placed inside the joint. Last, a needle roller bearing was added to the ankle housing and a cam was added to the spring foot to eliminate friction in the interface. All of these changes can be seen in see Fig. 5-1.

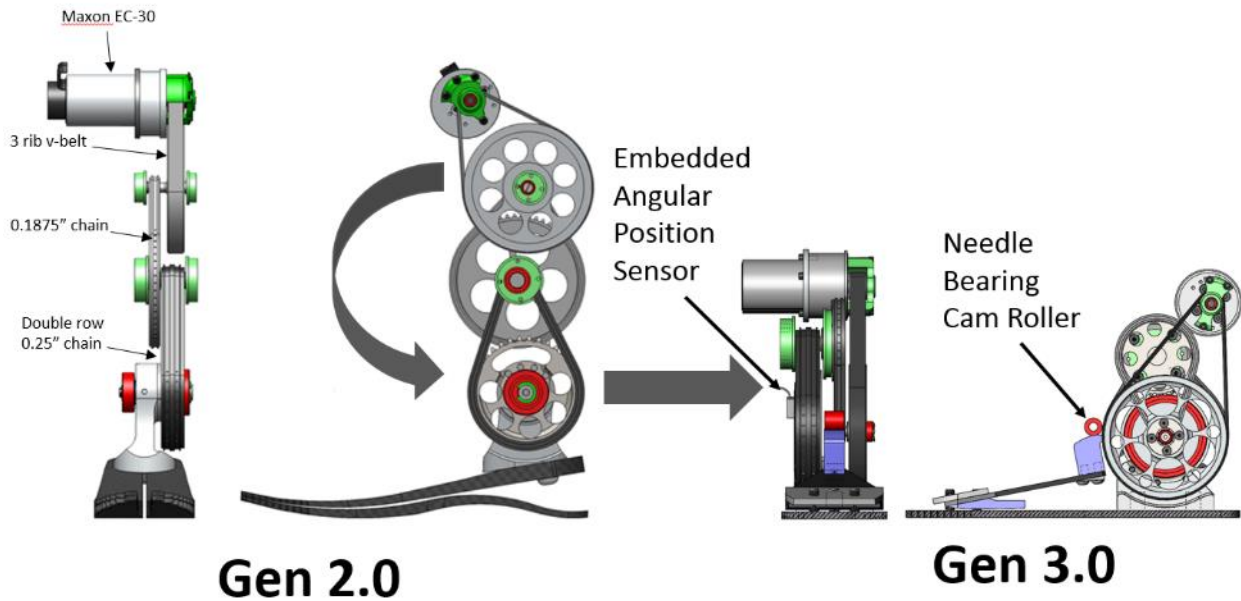


Figure 5-1 Transmissions of Gen 2.0 and 3.0 ankle units, showing a linear vs. folded configuration. Also showing the addition of an embedded angular position sensor and cam roller configuration in Gen 2.0.

A 7075 aluminum structural shell housing was employed as with Gen 2.0, Fig 5-2. All sprockets were flame hardened 4140 steel and bearings were minimum ABEC 5 tolerance. As with previous designs, finite element analysis was performed using ANSYS and all transmission components and structural members had a factor of safety of 1.8 and 2.0 respectively.



Figure 5-2. A picture of the physical prototype from Schultz et al. [38]

For controller development and testing, a transfemoral control board and a battery were attached to the outside of the housing (not shown). Additionally, able bodied adapters were made to allow a non amputee to walk on the prosthesis. A commercial passive carbon fiber prosthesis was used for the contralateral side. For detailed results of the tests and controller development the interested reader is referred to Schultz et al. [38]. Prosthesis and healthy power and torque vs. percent of stride are given in Fig. 5-3.

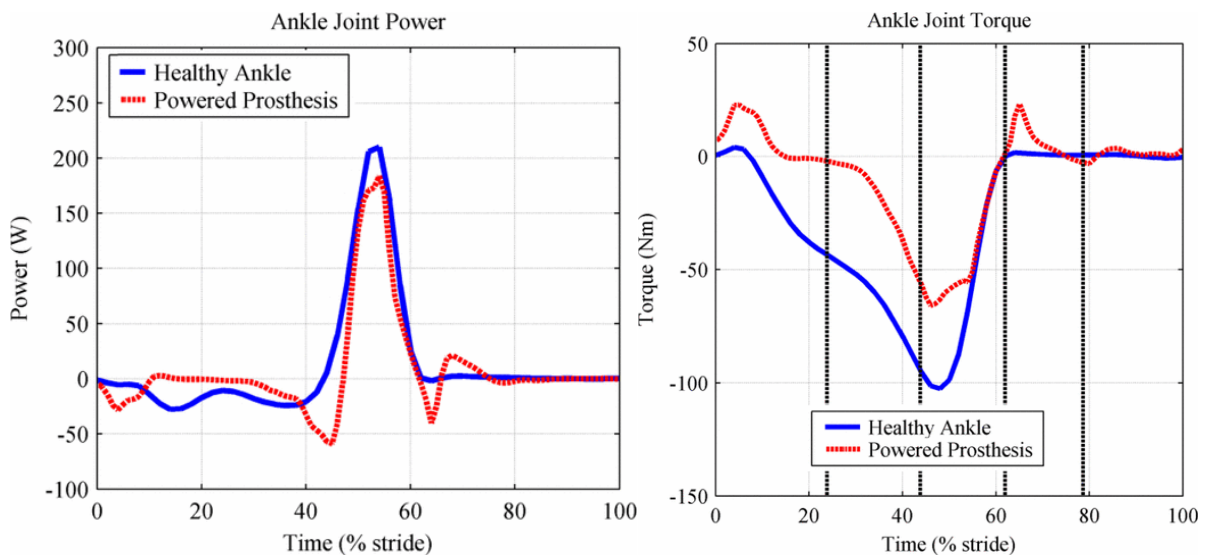


Figure. 5-3. Power and torque vs. percent of stride for the Gen 3.0 prosthesis, from Schultz et al [38].

Referring to the above plots, the prosthesis is able to reproduce biomechanically healthy levels of power, but is torque limited during push off (~40% of stride). This was due to a low spring stiffness in the foot and to the reduction in transmission ratio from Gen 2.0 to Gen 3.0.

It is worth noting that even though the spring stiffness was lower than needed, the cam roller interface did work well compared to the Gen 2.0 design, but the springs had a very low cycle life. In a subsequent design, the spring shape was changed from curved to straight, the stiffness was increased, and an aluminum cam was added Fig. 5-4. This design worked well and was used in subsequent ankles.

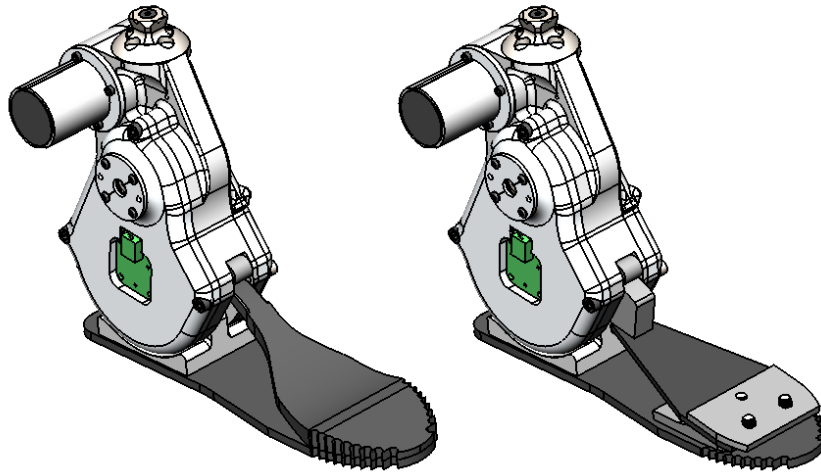


Figure. 5-4. Curved and straight spring feet.

Gen 3.0 Transtibial Prosthesis Conclusions

A standalone transtibial prosthesis was developed and successfully tested on a healthy subject using an able bodied adapter. The transmission was made significantly shorter than the previous design by folding the transmission on itself. It was able to reproduce biomechanically healthy levels of power, but was somewhat torque limited at push off due to a reduction in transmission ratio from the previous design and a low foot spring stiffness. The torque deficiency will be addressed in a subsequent redesign.

Load Cell

A new load cell was developed to address the issues listed above, namely, non-repeatability, hysteresis and motion that was not parallel with the axis of the leg. The four bar mechanism design was again used, but in a double back to back arrangement as shown in Fig. 5-5. This change resulted in axial motion from top to bottom of the device. To eliminate non-repeatability and hysteresis, needle roller bearings replaced bronze bushings at all joints and a steel die spring replaced the rubber elastomer. A standard pyramid connection was added to the distal end to mate with a standard pyramid pylon or the ankle unit.

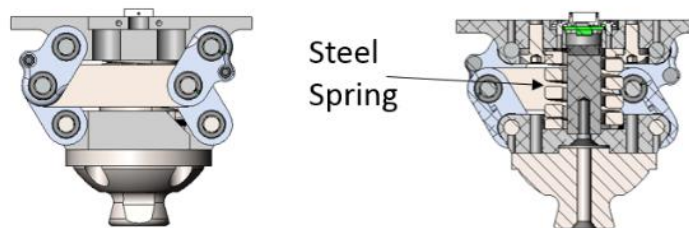


Figure 5-5. The double four bar load cell (left) and a cross section showing the steel spring (right)

The load cell as designed worked well and showed repeatable, linear behavior in a modular package. The design was subsequently used in a transfemoral design described below.

Generation 3.0 Transfemoral and Generation 3.1 Transtibial Prostheses

Using the folded transmission developed in the Gen 3.0 Transtibial described above, a new knee unit was developed. It had a transmission ratio of 172:1, essentially the same as 179:1 of the Gen 2.0 design. The slight difference was a result of packaging and discrete chain length considerations. In addition the structural housing was made a little wider to provide a heat sink for the electronics and a space for the battery. Covers were added to house these components.

A new Gen 3.1 ankle was designed using a folded transmission. To increase the needed torque during push off a EC60 flat motor replaced the EC30 of the Gen 3.0 design. With the additional motor torque the transmission ratio was reduced from 143:1 to 118:1 to make a more compact package. Also a new foot was used based on the design from the Gen 3.0 ankle.

Last, the double four bar was used and attached to the bottom of the knee unit and a standard prosthetic pylon was used to connect the units. The transfemoral design is shown in Fig. 5-6.

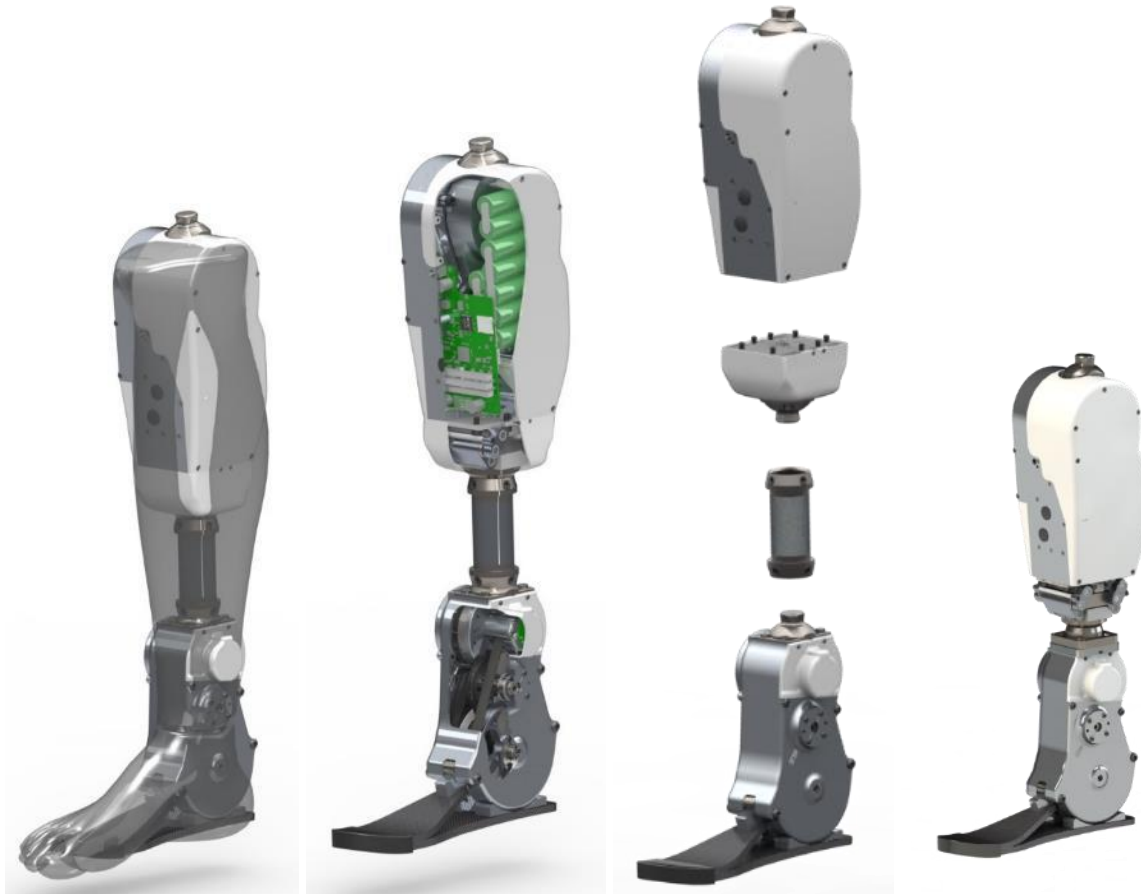


Figure 5-6. Gen. 3.0 Transfemoral and Gen. 3.1 Transtibial Prostheses showing fit inside a 50% male anatomical envelope (left), enclosed electronics and battery (center left) modularity of knee, loadcell and ankle units (center right) and configured for shortest build height of 8% female (right).

Transmission Characterization

The primary control strategy employed for the devices described here is impedance control, where the joint torque emulates torsional springs and dampers and is given by:

$$\tau = k_l(\theta - \theta_o) + b\dot{\theta} \quad (1)$$

Therefore, tests were performed to measure the range of stiffness and damping that each joint could emulate. In addition, each joint was commanded with a torque step to access open loop torque tracking. Finally a chirp signal was commanded to measure the damped natural frequency of each joint. The experimental setup for measuring stiffness and damping is shown in Fig. 5-7.

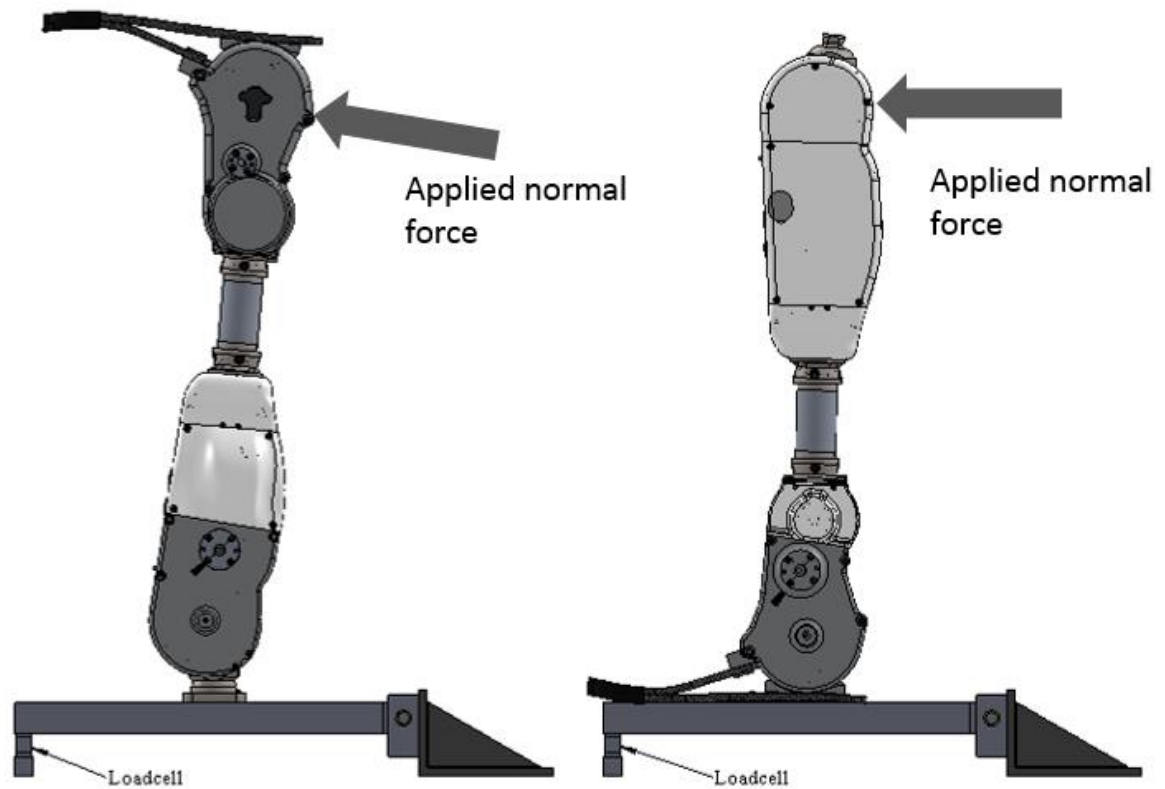


Figure 5-7. Experimental setup for measuring stiffness and damping of knee (left) and ankle (right)

Each joint was rigidly attached to a beam. The right side of the beam was supported with a pin joint using a steel pin and bronze bushing. The left side was supported by a push-pull type load cell (Transducer Techniques Model MLP-100), which was zero phase filtered at 30 Hz to reduce analog noise. The ankle joint stiffness range was measured without the spring foot and then a separate test was performed to measure the contribution of the spring by itself.

Each joint was programmed to emulate a range of stiffness from 1 N-m/deg. to 22 N-m/deg. This range is more than adequate as the stiffness required in the knee and ankle are approximately 6 Nm/deg. and 7 Nm/deg. respectively. Next, a normal force was applied at the other end of the leg, producing a torque about the respective joint, which was measured as a linear force at the load cell. Results are shown in Fig. 5-8, where the commanded stiffness is plotted as a straight line and the measured data is plotted on top of it.

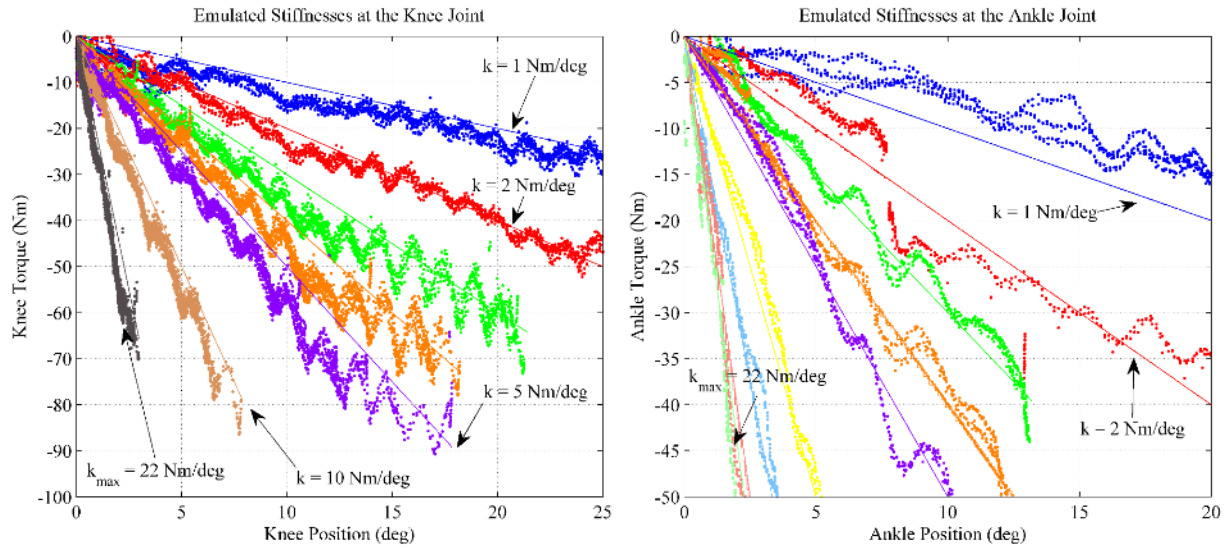


Figure 5-8. Commanded and measured stiffness at the knee joint (left) and ankle joint (right).

As seen, the ankle is able to provide highly stable stiffness tracking well beyond the range needed for control. It should be noted that the undulations in the measured data are caused by torque ripple which is a well know phenomena in chain driven systems.

Next, the foot was re-attached and the ankle programed to have zero stiffness. A normal force was applied at the top of the knee and the spring stiffness was measured. Results are shown in Fig. 5-9. The spring stiffness was about 7.4 Nm/deg. over the range of normal walking from zero to eight deg. of dorsiflexion. The stiffness can be changed by altering the carbon fiber layers in the spring, and the final value is a tradeoff between the value required for walking and for slope standing. A higher value helps more energy during push off, but the motor has to fight it if the user is standing on and facing up a slope.

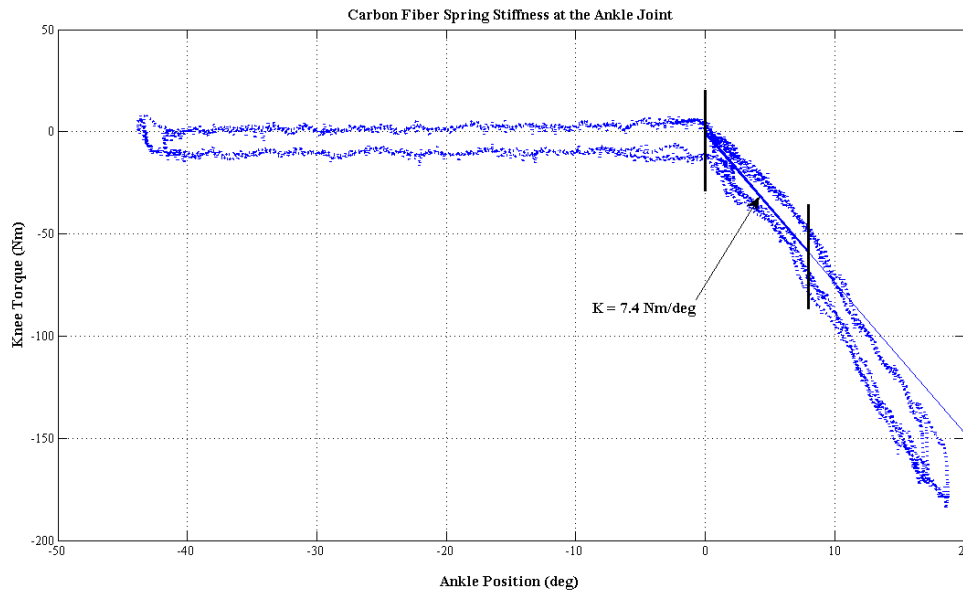


Figure 5-9. Measured stiffness of foot spring.

The same experimental setup was used to measure damping. The knee and ankle joints were rotated through a range of velocities from slow to fast. Joint torque was measured with the load cell and joint velocity was measured using the joint position sensors. Several preliminary experiments were done to measure the range that each joint could produce before becoming unstable. Afterwards the knee was programmed to emulate 0.55 Nm*s/deg. and 0.10 Nm*s/deg. and ankle to emulate 0.2 Nm*s/deg and 4.0 Nm*s/deg. Fig. 5-10.

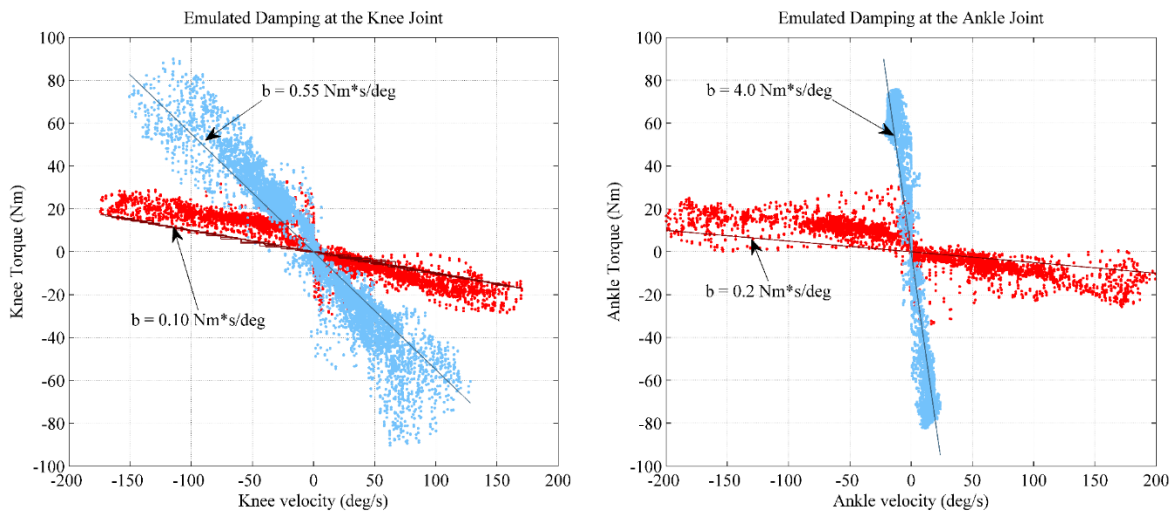


Figure 5-10. Commanded and measured damping at the knee joint (left) and ankle joint (right).

Note that the ankle is able to emulate a much higher damping because of the larger rotor inertia of the motor. As shown, the knee and ankle were able to provide highly stable damping at the commanded values.

In each case, the commanded values are above and below the maximum needed value of about 0.5 Nm*s/deg.

The last test measured the open loop step response to a torque input. In this test, the knee and ankle joints were separated and rigidly attached to a table in a horizontal position, Fig. 5-11. The end opposite the joint was then attached to the table through the same load cell mentioned above, such that torque at the joint was measured as a linear force.

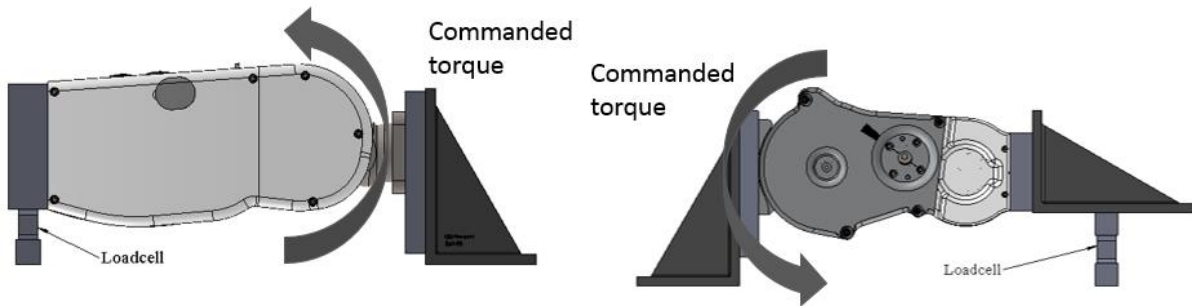


Figure 5-11. Experimental setup for measuring open loop torque response of knee ankle joint (left) and ankle joint (right)

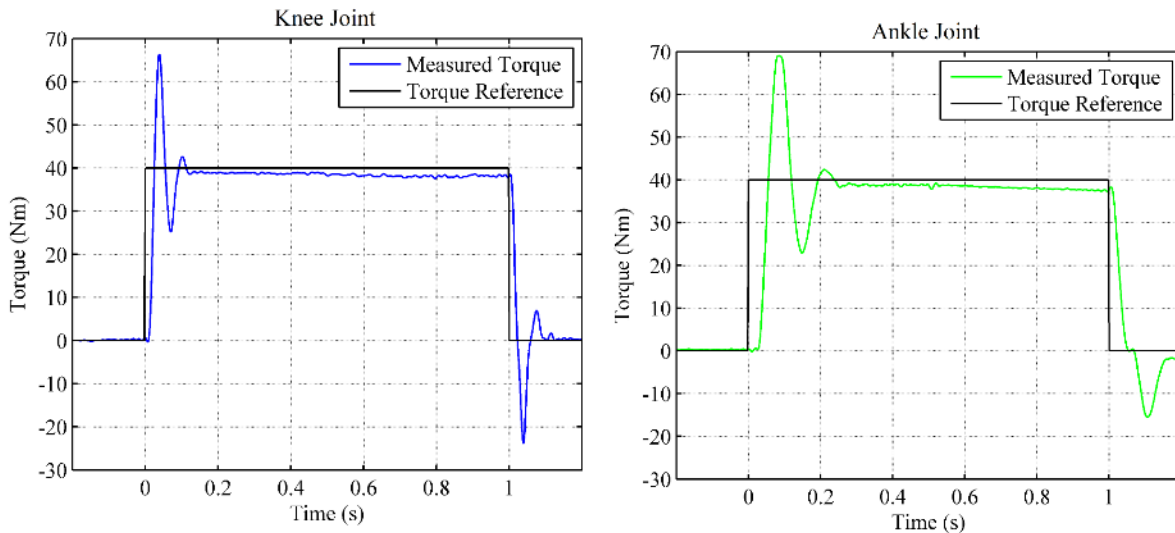


Figure 5-12. Torque step response of ankle joint (left) and knee joint (right).

As shown the knee and ankle joint transmission dynamics are characterized by a rise time of approximately 100 ms and 250 ms respectively. The knee has a damped natural frequency of approximately 15 Hz and approximately 2.5% a steady state torque. The ankle joint has a damped natural frequency of 6 Hz approximately 2.5% and a steady state torque error of.

It should be noted that knee and ankle joint torque data for healthy subjects are characterized by significant frequencies at or below 1 to 2 Hz (as given by a Fast Fourier Transform of the data presented in[27]) and torque magnitudes similar to the ones shown above, therefore, the transmission dynamics of the knee and ankle joints are assumed to essentially preserve the torque dynamics characteristic of walking.

Conclusions

A new generation of transfemoral and transtibial prosthetic devices were developed which the author feels is very close to a pre commercial product. Both transmission packages were made much more compact by introducing a folded belt, chain, chain configuration. Standard prosthetic connections are used between the devices which allow for maximum adjustability and flexibility. The design is truly modular such that the ankle transmission can be separated and used as a standalone unit as demonstrated. A new spring foot design was presented which successfully eliminates the stiction of the previous design and a new modular parallel link load cell design was shown which is both repeatable and linear. All sensors, electronics and batteries were completely enclosed

Finally results of the transmission characterization were presented. The measurements demonstrated that each joint could produce necessary levels of stiffness and damping and that biomechanically normal levels of torque could be produced with the bandwidth needed for walking.

CHAPTER VI

Manuscript 2: A Powered Knee and Ankle Prosthesis for Transfemoral Amputees

Brian E. Lawson, Jason E. Mitchell, Don Truex,
Amanda Shultz, Elissa Ledoux, and Michael Goldfarb

Department of Mechanical Engineering
Vanderbilt University
Nashville, TN 37235

Provisionally Accepted to the
IEEE Robotics and Automation Magazine
Special Issue on Wearable Robotics

Abstract

This article describes the design and control of a powered knee and ankle prosthesis for transfemoral amputees. Following a description of the design hardware of a recent prosthesis prototype, the authors describe a hybrid control approach that provides coordination for level walking. The hybrid control approach combines a piecewise-passive impedance-based component during the stance phase of gait with a high-impedance trajectory-tracking component during terminal stance and swing. To validate the design, the controller was implemented on the powered prosthesis prototype, and its ability to provide level walking functionality was evaluated on three transfemoral amputee subjects. Data are presented from these experimental trials indicating that the prosthesis and control approach reproduce knee and ankle joint kinematic and kinetic features that are highly representative of corresponding healthy joint biomechanics.

Introduction

Lower limb prostheses have traditionally been energetically passive devices (i.e., they can store or dissipate power, but cannot produce net power). Amputees who utilize passive limbs generally walk more slowly, expend significantly more energy during ambulation, are more limited in the types of terrain they can traverse and types of activities they can perform, and fall frequently relative to healthy counterparts

x[39-47]. The intent of a prosthesis is to replace the biomechanical functionality of the healthy limb. The joints of the healthy limb provide a variety of biomechanical behaviors which vary considerably within and between activities, and which are in general characterized by power dissipation, storage, and generation. As such, it is reasonable to assume that endowing a prosthesis with power, and by extension with the ability to emulate the variegated behaviors exhibited by the healthy limb, would alleviate some of the previously cited deficiencies in mobility and stability.

Although investigations of powered prostheses started several decades ago (see, for example,[48, 49] , the vast majority of relevant research has occurred within the past decade, due presumably to recent enabling improvements in constituent component technology, such as the increased power density of brushless DC motors, the increased energy and power density of lithium-polymer and lithium-ion batteries, and the enhanced functional capability of low-power microcontrollers and integrated-circuit-based inertial measurement units (IMUs). Publications describing powered prosthetic systems to date can be grossly classified as those describing the development of powered ankle prostheses (and corresponding control systems), e.g. [18, 50-58], which have been directed at limb replacement for people with transtibial amputation, or those describing the development of powered knee prostheses (and corresponding control systems), e.g. [13, 14, 59, 60], which have been directed at limb replacement for people with transfemoral amputation. The design and control approaches associated with these powered prosthesis systems vary considerably, and the interested reader is referred to the cited articles for details regarding device design and corresponding control approaches for each.

The authors have developed over the past decade a powered knee and ankle prosthesis system which is described in this paper. Unlike the previously mentioned research efforts, which describe single-joint powered prosthesis systems, the prosthesis system described here incorporates and coordinates the actions of both a powered knee and ankle joint, with the intention of better replicating the biomechanical functionality of the healthy limb for persons with transfemoral amputation. This paper is intended to present and summarize the significant design and control aspects of this prosthesis system, which currently exists in its third major design generation. Relative to the previously cited published works, and relative to prior publications on related topics by the authors, e.g. [61-65], this paper presents and describes a new and substantially different design of a powered knee and ankle prosthesis (Section II), which offers a number of desirable features relative to previously published designs. In addition, a new control approach is described in Section III, which substantially reduces the number of tunable parameters in the controller relative to a previously published control approach employed by the authors. Finally, in an effort to demonstrate efficacy of the prosthesis design and validity of the control approach described here, Section IV presents new and previously unpublished experimental results from multi-subject level walking trials.

Prosthesis Design

Design Objectives

As presented in [61-65], the nominal torque, speed, and range of motion design objectives for each joint are informed by the superposition of biomechanical data published for healthy subjects for the basic activities of locomotion, principally walking and stair ascent and descent. As described in those papers, such activities require a nominal range of motion, maximum torque, and peak power of 120 deg, 75 Nm, and 150 W, respectively, at the knee joint, and 65 deg (45 deg plantarflexion, 20 deg dorsiflexion), 130 Nm, and 250 W, respectively, at the ankle joint.

The design presented here further incorporates several objectives beyond those associated with the electric design previously described by the authors [61]. First, the design presented here is intended to incorporate mechanically-separable knee and ankle joints that are connected via a pyramid connector and pylon interface, which enables compatibility with the mechanical interfacing, height adjustment, and alignment norms of the prosthetics industry. Second, in order to fit a larger population of individuals, the prosthesis was designed to accommodate a lower minimum build height relative to the previously presented design. Third, for both cosmetic and protective reasons, each joint of the prosthesis was designed with a fully enclosed actuator and transmission. Fourth, in an effort to increase the operational lifetime of the prosthesis, the present device was designed such that no electrical wires cross either the knee or ankle joint (i.e., all instances of flexing wires were eliminated). Finally, the previously presented design incorporated instrumentation (i.e., strain gages) on the foot. In order to more easily accommodate the wide variety of foot sizes used in a lower limb prosthesis, in addition to eliminating flexing wires (across the ankle joint), the present device was designed with a non-instrumented foot. In place of load information from the foot, load information in the design described here is provided by a load cell located in the shank. Attaining all of these objectives necessitated a complete redesign relative to that presented in [61], such that the current device is different in essentially every component, as described below.

Actuation and Structure

A rendering of the powered prosthesis, with some sections cut away to show design components, is shown in Fig. 6-1. Additionally, a summary of key design characteristics is included in Table 6-1. As shown in Fig. 6-1, the prosthesis consists of a powered knee unit and a powered ankle unit, separated by a standard prosthetic pylon, allowing alignment adjustments between the knee and ankle axes, as well as adjustability of the shank length. As shown in the figure, the knee unit includes a battery and embedded system that powers and controls both joints. The knee unit additionally incorporates a load cell, which measures the ground reaction force along the shank. The knee and ankle units are electrically connected by a flexible wire tether to accommodate height adjustability.

The Vanderbilt Powered Prosthesis

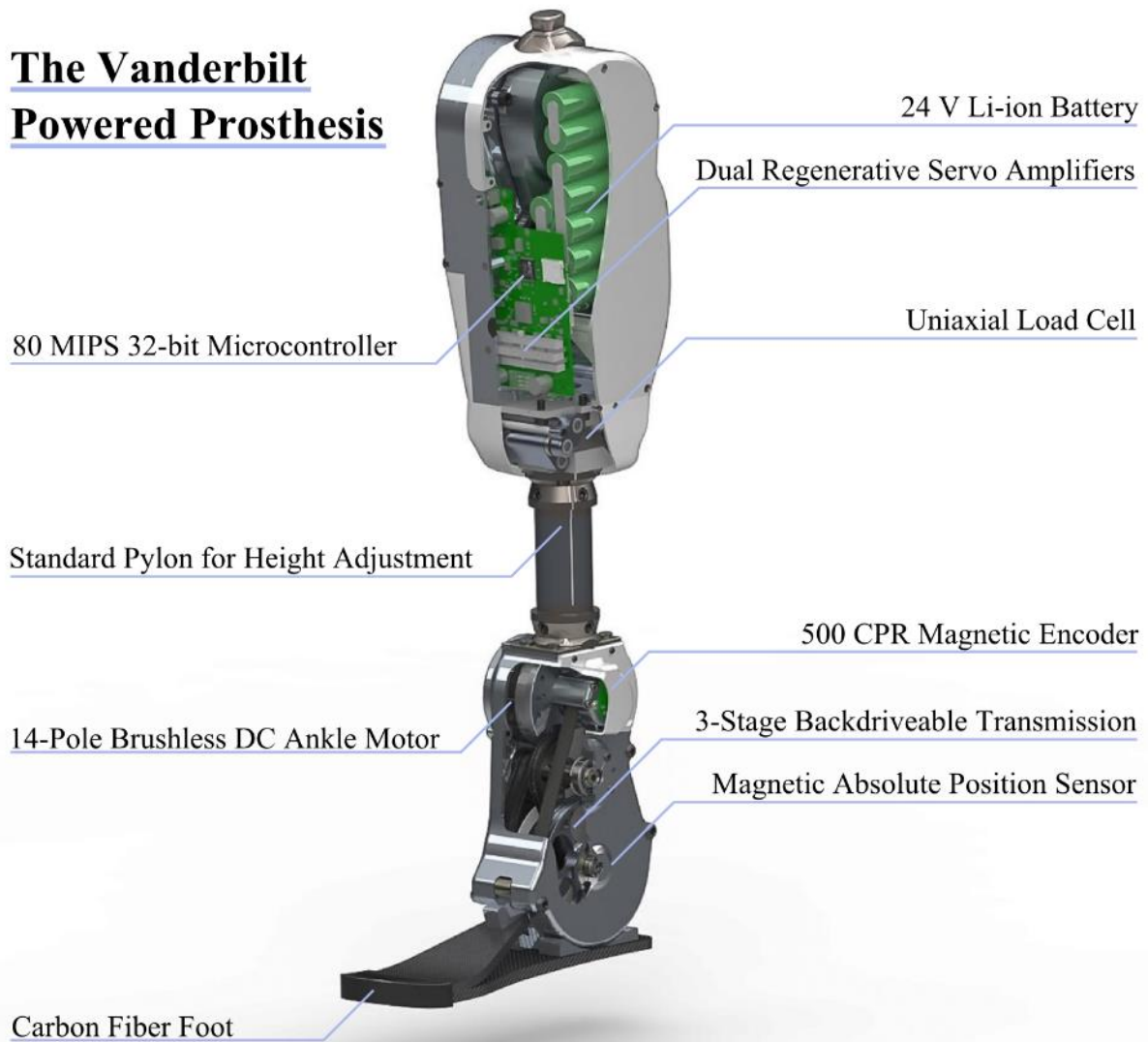


Figure 6-1. A rendering of the CAD model of the powered prosthesis.

Characteristic	Value
Maximum Knee Torque	85 Nm
Maximum Ankle Torque	110 Nm (from motor)
Knee Range of Motion*	-5° to 115°
Ankle Range of Motion†	-45° to 25°
Battery Capacity	125 W·hr
Maximum Battery Current	30 A
Maximum Motor Current	18 A
Nominal Mass‡	5 kg

* Positive in flexion

† Positive in dorsiflexion

‡ As configured for a 50th percentile male

Table 6-1. Mechanical and Electrical Characteristics of the Powered Prosthesis

The control approach described subsequently requires that each joint of the prosthesis be capable of utilizing feedback control to provide software emulation of a range of stiffness and damping behaviors. Such emulation requires four-quadrant control of power at each actuated joint, and thus requires a torque-controllable and back-drivable joint. In order to provide this design objective, both the knee and ankle units were designed incorporating the combination of a brushless DC motor and a three-stage belt/chain speed reduction transmission. Specifically, the knee incorporates a Maxon EC-4pole 30 brushless motor, which drives the knee joint through a 176:1 speed reduction, the combination of which is capable of generating a maximum active torque of approximately 85 Nm through its actuated range of motion of 120 deg (5 deg hyperextension and 115 of flexion). The ankle joint incorporates a Maxon EC60 brushless motor, which drives the ankle joint through a 115:1 speed reduction, the combination of which is capable of generating a maximum active torque of approximately 110 Nm through its actuated range of motion of 70 deg (25 deg dorsiflexion and 45 deg plantarflexion). The actuator output at the ankle joint is supplemented by a carbon-fiber leaf spring incorporated into the foot, which is characterized by a stiffness of approximately 6 Nm/deg, and engages at approximately zero degrees in the ankle range of motion. The spring biases the output capabilities of the ankle towards plantarflexion, which is consistent with the biomechanical characteristics of the ankle during locomotion[27]typical ankle angles during late stance, the spring provides around 60 Nm of supplemental torque. Note that the spring is initially calibrated and subsequently cancelled within the low-level control system (e.g., a command of zero torque from the low-level controller will result in a freely moving joint). In this manner, the only substantive effect of the parallel ankle spring is to shift the maximum torque and power output capabilities of the joint to better align with the asymmetric output characteristics of the healthy ankle.

The structural components of the knee and ankle units are machined from 7075 aluminum alloy. The knee and ankle structures are designed to accommodate users of up to 115 kg body mass in addition to the internal loads imposed by the actuators, with a minimum safety factor of 2 against structural failure. Given the respective sizes of the knee and ankle units, the minimum build height of the prosthesis corresponds to a measurement between the knee center and ground of 425 mm, which corresponds to a 10th percentile female dimension, as given by[66] (i.e., the prosthesis should fit all adult males, and 90% of the adult female population). As configured for a 50th percentile male, the mass of the prosthesis prototype is approximately 5 kg.

Sensing

In addition to a 6-axis IMU in the shank, the prosthesis includes sensing for the knee and ankle angles and angular velocities, and for the axial load in the shank. All sensing is based on contactless sensors to enhance reliability and lifetime. The angular positions of the knee and ankle joints are measured by absolute magnetic encoders (4000 counts/rev) located coaxially with the joints, and also by incremental magnetic encoders (4000 counts/rev) located coaxially with the motor shafts. Note that although the sensor resolution is the same, the incremental encoder provides a measurement resolution relative to the joint approximately two orders of magnitude greater than the absolute encoder, since its resolution is effectively multiplied by the transmission ratio of the respective joint (i.e., 176 or 115 for the knee and ankle, respectively). In order to mitigate drift in the absolute angular position measurement of each joint, position information from the incremental encoder (around the motor) is fused with position information from the absolute encoder (around the joint) with a first-order complementary filter with a -3 dB crossover frequency of 1 Hz. The angular velocities of the knee and ankle joints are calculated from the incremental magnetic encoders on the motor shafts using a differentiator with a second-order roll off at 40 Hz. Note that all filters are implemented as discrete-time approximations of continuous-time transfer functions at a sampling rate of 500 Hz. The axial load in the prosthetic shank is measured through the previously mentioned load cell, which is situated just distal to the knee unit (see Fig. 1). The load cell consists of a double parallelogram four-bar linkage, configured such that the parallel platforms are separated by a helical compression spring with a stiffness of approximately 360 N/mm (2080 lb/in), and which are constrained by the linkage to move strictly axially with respect to the shank. A linear magnetic encoder measures the displacement across the spring, and thus produces a measure of the shank axial load. The measurement range can be variably configured, but for the experiments described here, was set for a maximum axial load of 1000 N (225 lb). Given the use of a 10-bit A/D converter, a measurement range of 1000 N results in a measurement resolution of approximately 1 N. Note that, at maximum load, the load cell compresses approximately 2.8 mm (0.110 in).

Embedded Electronics

The essential components of the prosthesis electrical system are depicted in the schematic shown in Fig. 6-2. The prosthesis power supply is a nominal 24 V lithium-ion battery pack, rated at approximately 125 W-hr. Since the prosthesis consumes approximately 85 W of electrical power during normal level walking (average for the three subjects tested for this article), the battery pack is estimated to provide 1.5 hours of continuous walking on a full charge, which corresponds to a walking range of approximately 6.75 km at a typical speed of 4.5 km/hr. The main processing element is a 32-bit microcontroller from Microchip Technologies (PIC32MX575F512L), which runs the primary control loop at 500 Hz. In this loop the main controller executes the joint torque controllers (described subsequently), in addition to performing secondary functions such as logging data, communicating with the servo controller, and servicing other peripherals (such as communication with the IMU over SPI). A secondary processing element (a 16-bit digital signal processor from Microchip Technologies, dsPIC33FJ64GS608) receives motor current commands from the main controller at 500 Hz, and uses these references to control current in the brushless DC motors via a pair of custom regenerative servo-amplifiers, each of which samples motor current at 150 kHz, runs closed-loop current control at a sample rate of 4.6 kHz (based on a filtered version of the sampled motor current), and switches the MOSFET bridges at a PWM rate of 45 kHz. The current control loop for each motor consists of the combination of a feed-forward motor model supplemented with a PI feedback loop.

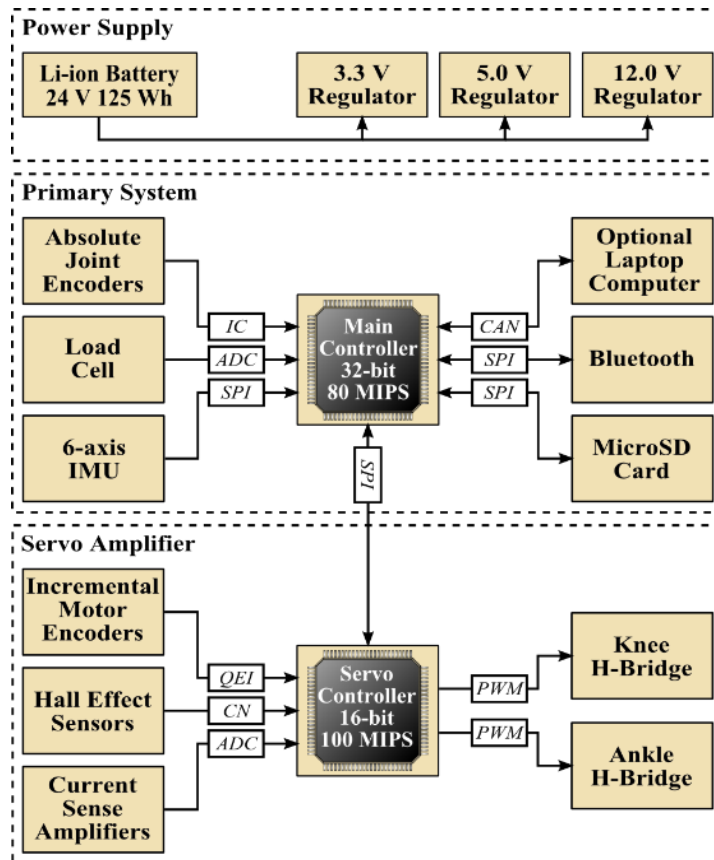


Figure 6-2. Overview of the embedded system architecture. Inputs to the main controller include absolute encoders for each joint; an analog voltage signal from the load cell, measured via an onboard 10-bit A/D converter; and an integrated 6-axis inertial measurement unit which communicates over a serial peripheral interface (SPI). Outputs to the main controller include an optional controller area network (CAN) interface for real time data monitoring on a computer, a wireless Bluetooth interface also for data monitoring, and a microSD card reader for both data logging and parameter selection. The inputs to the servo-controller include incremental encoders for each joint; Hall effect sensor signals from the brushless DC motors; and analog current measurement signals from the three phases of each brushless DC motor (via the onboard 10-bit A/D converter). The outputs of the servo-controller are pulse-width modulated (PWM) signals that control the brushless motor MOSFET bridges.

Control Approach

Low-level control

As previously mentioned, the control approach described subsequently requires software emulation of stiffness and damping at each joint via feedback-controlled actuation. As described in [67-69], the capacity of a feedback-controlled system to emulate a range of stiffness and damping behaviors is limited by the extent of open-loop phase lag (i.e., dynamics), sensor quantization, sampling delay, and hard nonlinearities (such as Coulomb friction and backlash) within the feedback loop. In order to minimize the presence of these behaviors in the feedback loop, a control structure is implemented in the prosthesis in which the high

frequency content of the position signal for the feedback loop is closed around the motor, rather than around the motor and transmission combination. This approach enables stable emulation of a wide range of stiffness and damping behaviors at the motor, and reflects the resulting (simulated passive) behaviors to the user and environment through the dynamics of the mechanical transmission. Such an approach requires a sufficiently transparent transmission relative to the dynamic characteristics of locomotion, and specifically requires that the first mode of vibration of the transmission be high, relative to the frequency content of gait. Additionally, the frictional characteristics of the transmission should be small relative to characteristic levels of torque required for locomotion.

Figure 6-3 shows the measured open-loop characteristics of the joint transmissions for both the knee and ankle joints. Specifically, the plots show the measured joint torque relative to the commanded joint torque for each joint, for a commanded step in torque of 40 Nm. The output torque was measured on a bench-top setup using a bidirectional load cell (Transducer Techniques Model MLP-100), which was zero phase filtered at 30 Hz to reduce analog noise. As shown in the figure, the knee joint transmission dynamics are characterized by a rise time of approximately 100 ms, a damped natural frequency at approximately 15 Hz, and a steady state torque error of approximately 2.5%. The ankle joint transmission dynamics are characterized by a rise time of approximately 250 ms, a damped natural frequency of 6 Hz, and a steady state torque error of approximately 2.5%. Since knee and ankle joint torque data for healthy subjects are characterized by significant frequencies at or below 1 to 2 Hz (as given by a Fast Fourier Transform of the data presented in[27]) and torque magnitudes on the order of those shown in Fig. 6-5, the transmission dynamics of the knee and ankle joints (with damped natural frequencies of 15 and 6 Hz, respectively) are assumed to essentially preserve the torque dynamics characteristic of walking. As such, both knee and ankle joints are able to provide highly stable stiffness and damping emulation (as a result of excluding the transmission dynamics from the software emulation loop), in addition to accurate torque tracking within the frequencies and magnitudes of joint torques characteristic of human locomotion.

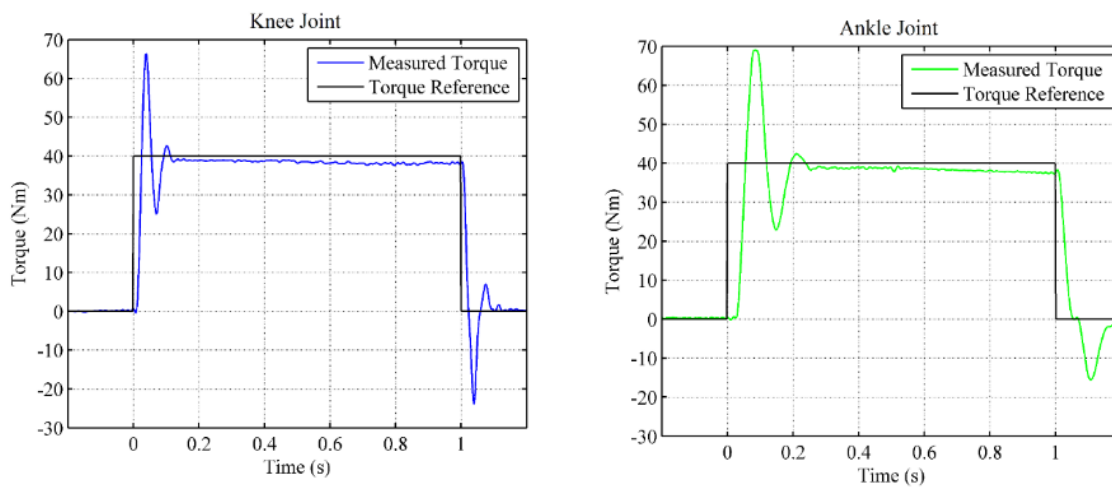


Figure 6-3. Experimentally measured response of both knee and ankle joints to a 40 Nm step command in joint torque.

Coordination control

The prosthesis control system consists of a hierarchical state machine, the top layer of which is called the supervisory controller. The states of the supervisory controller are called “activities.” An activity is itself a finite state machine, the states of which are called “phases.” An example of an activity in the supervisory controller would be standing, and an example of a phase in the standing activity controller would be weight bearing.

The supervisory controller governs transitions from one activity to another, while each activity controller dictates transitions from one internal phase to another. There are four activities contained in the supervisory controller. These activities are shown in the state machine depicted in Fig. 6-4. Within any given phase of any given activity, impedance parameters and equilibria are specified for the knee and ankle joints. The impedance control law for each joint within each finite state is given by:

$$\tau = k(\theta - \theta_{eq}) + b\dot{\theta} \quad (1)$$

where τ is the commanded torque, k is the proportional gain or stiffness, θ is the joint angle, θ_{eq} is the desired joint angle equilibrium position, b is the damping coefficient, and $\dot{\theta}$ is the joint angular velocity. These stiffness and damping behaviors are emulated via the previously mentioned low-level control structure. Note that the control law does not explicitly track motion or torque, but rather emulates the physical relationship (i.e., the impedance) between these two quantities. This approach provides two substantial features. First, joint impedances can be selected that are representative of impedances exhibited by the healthy joint, which facilitates interaction with the ground and should provide to the user a more natural feel relative to a (high impedance) position controlled joint. Second, the behavior of the prosthesis within any given phase will be passive, yet energy can be introduced into the system by changing the stiffness or equilibrium position of the virtual spring during transitions between phases. Since phase transitions are based on mechanical cues from the user, the user retains control over the introduction of power into an otherwise passive system. Thus, the control approach provides both a natural feel (due to the selection of joint impedances) and an inherent safety characteristic (since the user has to be engaged to keep the prosthesis moving, and in the absence of direct excitation or input from the user, the prosthesis defaults to passive behavior). For further details regarding this framework, we refer the reader to [61].

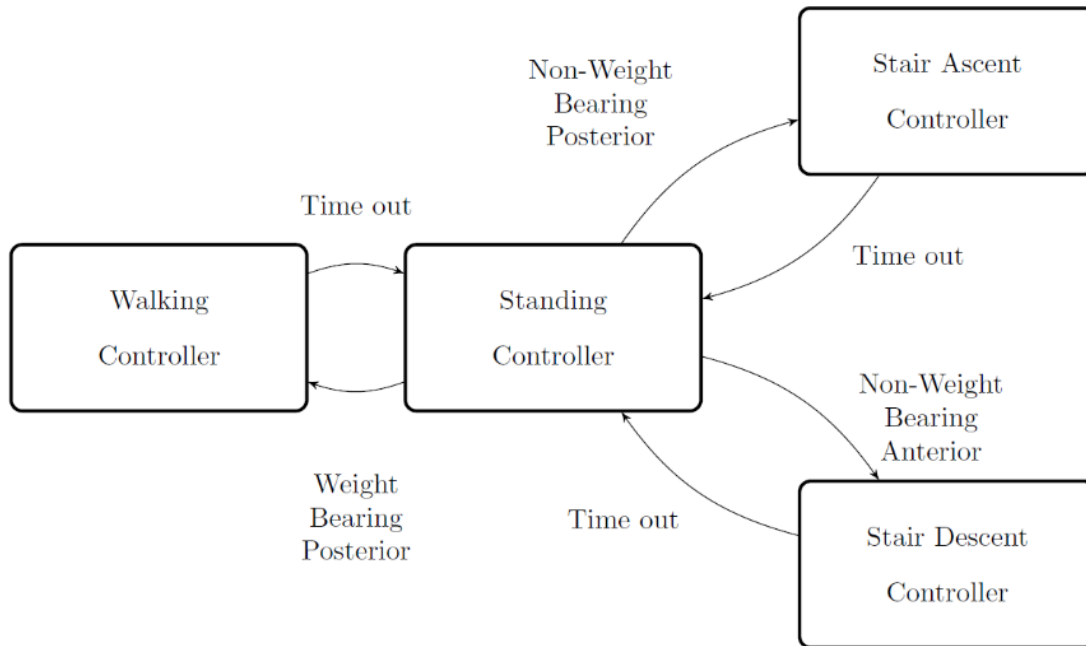


Figure 6-4. The supervisory state machine for the powered prosthesis.

Despite the features provided by this piecewise-passive impedance-based control approach, the approach is somewhat parameter-intensive, since each phase for each joint requires selection of three impedance parameters. As such, for a piecewise-passive impedance-based control approach for level walking with five phases, the two joints would require selection of thirty impedance parameters. In order to reduce the number of control parameters, a hybrid control approach was implemented for the walking controller. Specifically, since the effect of joint impedance is most evident when the prosthesis is in the stance phase of gait (i.e., when the user is interacting with the ground, a high-impedance environment), and less evident when the prosthesis is actively pushing off at the ankle or in swing, the authors implemented a control approach that incorporates a piecewise-passive impedance control approach during early and middle stance, but incorporates a trajectory-tracking high-impedance controller during terminal stance (which is an active segment of the gait cycle) and the swing phase of gait. The resulting hybrid walking controller consists of three phases, as depicted in Fig. 6-5. The first two phases, early stance and middle stance, are basic impedance states that roughly correspond to the first 40% of the gait cycle. The early stance portion begins at heel strike and ends at peak stance knee flexion, entering middle stance. Middle stance continues until an ankle angle threshold is reached, at which point the prosthesis initiates a step with a powered push-off.

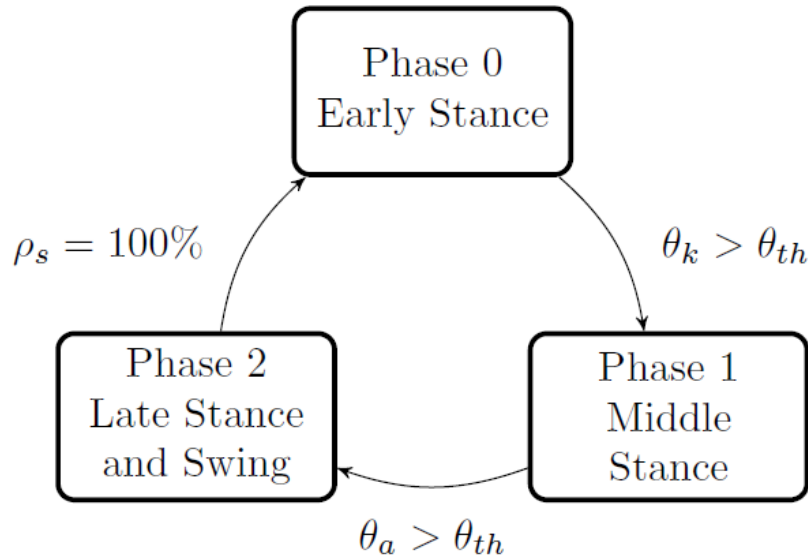


Figure 6-5. The walking state machine for the powered prosthesis. Phases 0 and 1 emulate the virtual impedance equation described by (1), with parameters tuned for each subject and listed in Table II. Phase 2 executes a trajectory as described in the text, and automatically reverts to Phase 0 upon completion of the trajectory (when ρ_s , the percentage of the stride, is equal to 100%). The transition from Phase 0 to Phase 1 is governed by the listed condition, where θ_k is the knee angle and θ_{th} is a predetermined threshold. The transition from Phase 1 to Phase 2 is governed by the listed condition, where θ_a is the ankle angle and θ_{th} is a separate, predetermined threshold.

In the third phase, instead of executing a series of piecewise passive phases, each of which would entail impedance parameter selection, the hybrid controller executes a trajectory at a relatively high impedance, where the trajectory for each joint follows a spline defined by a set of reference points interpolated from healthy walking data at different walking speeds. To achieve a variable cadence, the interpolation is based upon the length of time spent in the preceding stance phase, as determined by a timer that increments while the load signal is above a given threshold. Once the trajectory has finished, the prosthesis automatically reverts to the first phase, early stance, in anticipation of heel strike. In order to provide the energetic role of push-off in late stance, a feed-forward torque command is superimposed at the onset of the trajectory phase. The torque command is a single period of a unity-offset cosine wave, which provides a smooth and computationally simple torque pulse that is scalable in both width (time) and height (magnitude). This form of torque input provides an intuitive mechanism for the tuning of the “amount of push” delivered to (and perceived by) the user. Note that the strength of the powered push-off largely determines the net amount of energy delivered to the user over the stride.

Experimental Implementation and Biomechanical Results

The validity of the powered prosthesis design and control approach was assessed in experiments with three transfemoral amputee subjects. The ability of the powered prosthesis and controller to provide level

walking functionality was assessed by characterizing the knee and ankle joint biomechanics (e.g., joint angles, torques, and powers) during over ground walking, and comparing these to the biomechanical behavior of the knee and ankle joints in the healthy limb.

Biomechanical Assessment

Three subjects were recruited through local prosthetists for the assessment. The subjects' anthropomorphic data, along with data concerning the configuration of the prosthesis, are given in Table 6-2. Approval to perform these assessments was granted by the Vanderbilt Institutional Review Board and informed consent was obtained for each subject prior to each assessment. Subjects additionally gave permission for the publication of photographs and video. Figure 6-6 shows a photograph of one of the subjects walking with the powered prosthesis.

	Subject A	Subject B	Subject C
Height	1.93 m	1.83 m	1.83 m
Weight	79 kg	95 kg	86 kg
Age	25 yrs	24 yrs	46 yrs
Cause of Amputation	trauma	trauma	cancer
Years Post-Independent Ambulation	7	3	2
Amputation Side	right	left	left
Prosthesis Configured Weight*	5.09 kg	5.04 kg	5.05 kg
Prosthesis Configured Height†	54.0 cm	51.9 cm	50.5 cm
Prosthesis Foot Size	28 cm	28 cm	28 cm

* Excluding foot shell and sneaker

† As measured from the sole plate to the knee center

Table 6-2. Subject Data and Prosthesis Configuration



Figure 6-6. A subject walking with the powered prosthesis.

The prosthesis was fit to each subject, and the controller parameters were manually tuned. The primary controller parameters requiring tuning are the impedance parameters, the push-off trigger angle, and the push-off strength (see Table 6-3). The impedance parameters were tuned, starting with a set of nominal parameters obtained from healthy subject data (see discussion in [65]), to achieve subject comfort and sense of synergy with the prosthesis, and to achieve a biomechanical movement in the stance phase representative of healthy gait (e.g., appropriate stance knee flexion). The push-off trigger angle and strength were adjusted to provide a powered push-off that was comfortable to the user. A summary of the control parameters used for each subject is given in Table III. It is notable that not all the impedance parameters needed to be adjusted between subjects to obtain a comfortable gait. This process is analogous to that undertaken by prosthetist and patient as a passive prosthesis is mechanically aligned and adjusted for gait.

		Subject A		Subject B		Subject C	
		Knee	Ankle	Knee	Ankle	Knee	Ankle
Early Stance	k $\left(\frac{Nm}{deg}\right)$	4.5	5	3	5	3.5	2.5
	b $\left(\frac{Nm \cdot s}{deg}\right)$	0.1	0.2	0.1	0.2	0.1	0.2
	θ_{eq} (°)	10	0	10	0	12	0
Middle Stance	k $\left(\frac{Nm}{deg}\right)$	4	4	4	4.5	4	4
	b $\left(\frac{Nm \cdot s}{deg}\right)$	0.1	0.2	0.1	0.2	0.1	0.2
	θ_{eq} (°)	10	0	10	0	12	-3
Push-Off Angle		10°		8°		7°	
Push-Off Strength*		160 Nm		120 Nm		200 Nm	

Note: Highlighted parameters were consistent across all three subjects.

*Push-Off Strength refers to the peak value of the unity-offset cosine torque pulse command that is superimposed with the trajectory controller and is a tunable parameter for the system. This value is not the net torque experienced by the user during push-off.

Table 6-3. Level Walking Parameters for the Three Test Subjects

Biomechanical Data

Once tuned, each subject walked over ground on the prosthesis at a self-selected speed. Figures 6-7 through 6-9 show the averaged biomechanical data from the knee and ankle joints for each of the three subjects, averaged over twelve consecutive strides.

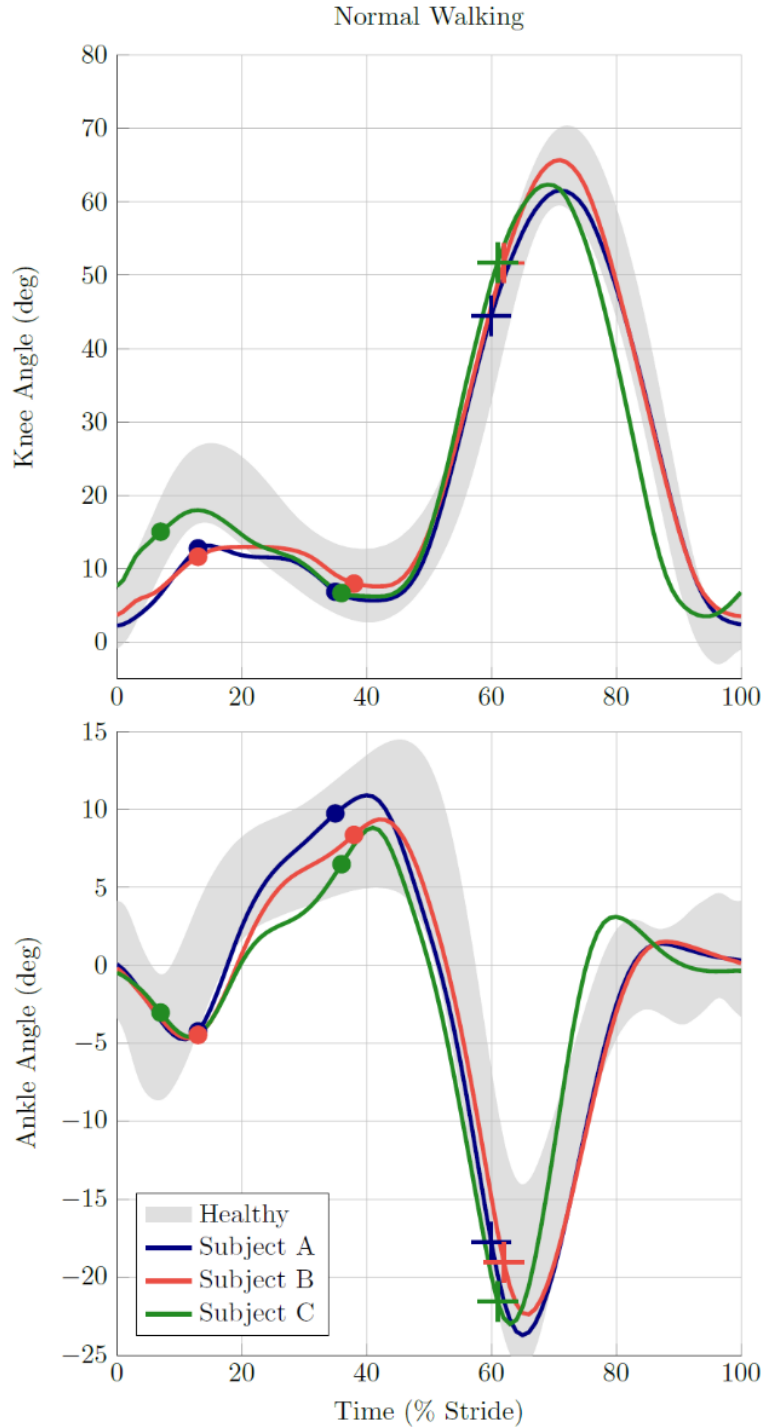


Figure 6-7. Knee and ankle kinematics for 3 amputee subjects using the powered prosthesis. For the knee joint, 0 deg corresponds to full knee extension, and flexion is positive. For the ankle joint, positive angles represent dorsiflexion and negative angles represent plantarflexion. The dots represent average state transitions for each subject (from Phase 0 to Phase 1, and from Phase 1 to Phase 2). The crosses represent toe off, as measured by the load cell. The largest standard deviations for each subject at the knee were 6.95, 6.85, 4.27 deg at 86, 84, and 85% of stride for subjects A, B, and C, respectively. The largest standard deviations for each subject at the ankle were 4.44, 2.68, and 1.88 deg at 57, 58, and 71% of stride for subjects A, B, and C, respectively.

Note that the data shown in these figures were computed in post-processing using sensor data from the prosthesis. The joint angles (Fig. 6-7) were measured with the absolute and incremental encoders at each joint. The joint torques experienced by the user (Fig. 6-8) were computed using a model of the passive characteristics of the motor, transmission (i.e., inertia, friction), and, in the case of the ankle joint, the parallel spring. The following models were used for the ankle and knee joints:

$$\tau_{ext,a} = \begin{cases} \tau_{mot,a} - J_a \ddot{\theta}_a - b_a \dot{\theta}_a - c_a \cdot \text{sgn}(\dot{\theta}_a) - k_a (\theta_a - \theta_0) & \text{if } \theta_a \geq \theta_0 \\ \tau_{mot,a} - J_a \ddot{\theta}_a - b_a \dot{\theta}_a - c_a \cdot \text{sgn}(\dot{\theta}_a) & \text{if } \theta_a < \theta_0 \end{cases}$$

$$\tau_{ext,k} = \tau_{mot,k} - J_k \ddot{\theta}_k - b_k \dot{\theta}_k - c_k \cdot \text{sgn}(\dot{\theta}_k) \quad (2)$$

where subscripts a and k represent each parameter or state for the ankle and knee, respectively, J_x is rotational inertia for the joint at the output, b_x is the viscous damping coefficient, c_x represents Coulomb friction, and k_a and θ_0 are the spring constant and engagement angle, respectively, for the parallel spring at the ankle. All parameters, which are listed in Table 6-5, were either experimentally measured, or estimated based on datasheet information or system identification approaches.

Symbol	Parameter	Value
k_a	Ankle Spring Stiffness*	5.7 Nm/deg
θ_0	Ankle Spring Engagement Angle*	0 deg
J_a	Ankle Effective Rotor Inertia†	1.58 kg·m ²
b_a	Ankle Viscous Friction*	0.0603 Nm·s /deg
c_a	Ankle Coulomb Friction*	1.13 Nm
J_k	Knee Effective Rotor Inertia†	0.103 kg·m ²
b_k	Knee Viscous Friction*	0.0261 Nm·s /deg
c_k	Knee Coulomb Friction*	0.802 Nm

* Experimentally measured

† Taken from motor datasheet

Table 6-5. Parameters for the Knee and Ankle Transmission Models

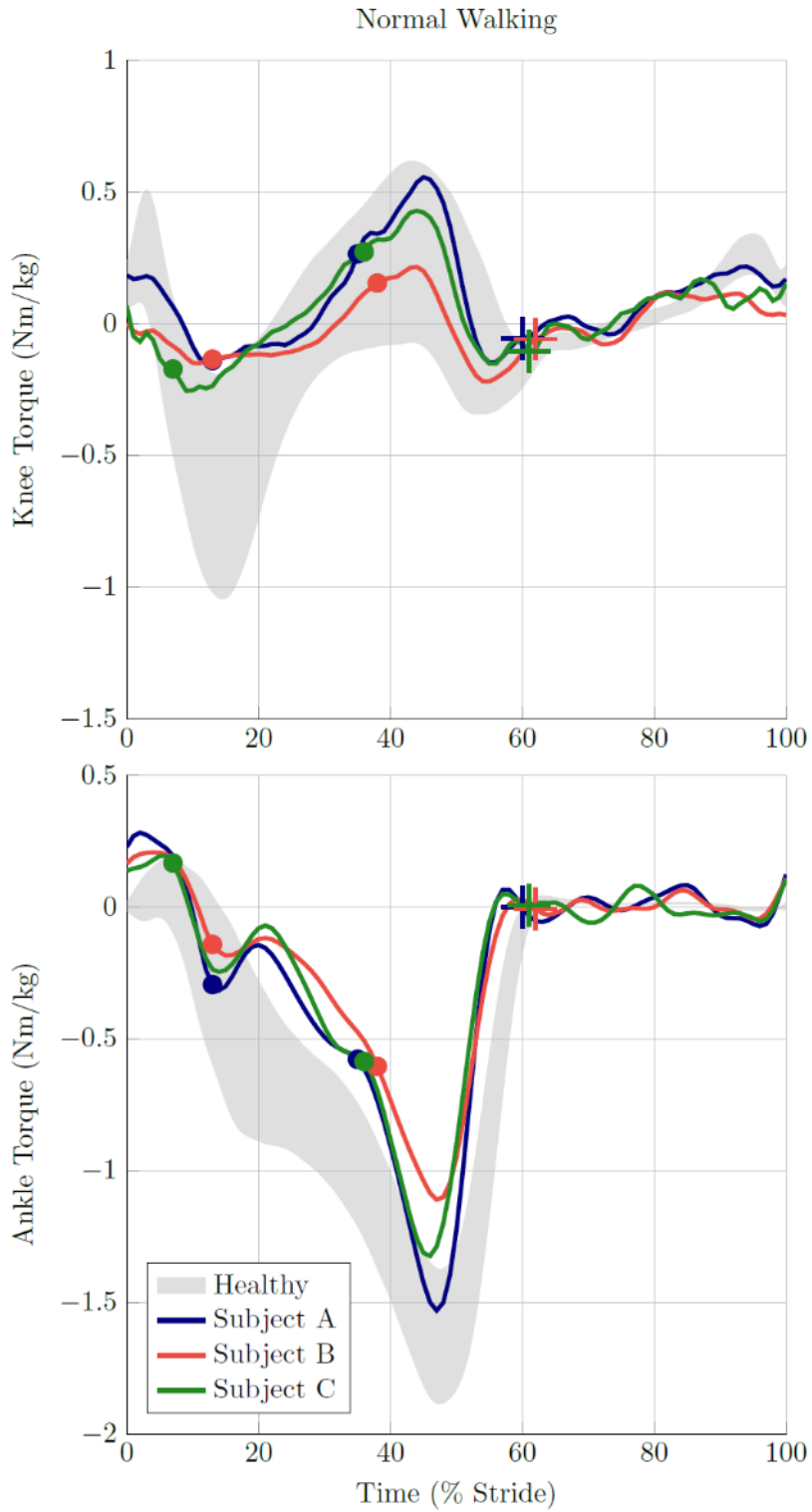


Figure 6-8. Knee and ankle kinetics for 3 amputee subjects using the powered prosthesis. For the knee joint, a positive torque is a flexive torque. For the ankle joint, positive torque is a dorsiflexive torque. The dots represent average state transitions for each subject (from Phase 0 to Phase 1, and from Phase 1 to Phase 2). The crosses represent toe off, as measured by the load cell.

The velocity signal used in the torque model was numerically computed from the position signal instead of using the real-time velocity signal in order to avoid phase lag from the 2nd order roll off. The final computed torque was zero phase filtered with an FFT transform removing frequencies above 20 Hz for the knee and 10 Hz for the ankle (note that these cutoffs are higher than the respective output torque bandwidths measured experimentally in Section III). The joint powers (Fig. 6-9) were calculated as the product of the joint torques and velocities computed in post processing. Finally, note that stride data were parsed based on load cell data, and in accordance with standard methods, plotted as a function of stride percentage. In all cases, the data are plotted along with data characterizing plus and minus one standard deviation around the corresponding mean behavior of the knee and ankle joints for healthy subjects measured during level walking at a self-selected speed, as provided by[27].

Figure 6-7 shows averaged knee and ankle joint angles for each subject exhibited by the prosthesis during walking. For all subjects, the prosthesis provides knee and ankle joint kinematics with the essential characteristics of healthy joint behavior. Specifically, as in healthy walking, the knee joint exhibits stance knee flexion between 0 and 30% of stride, although peak flexion values for the amputee subjects are somewhat less than the healthy average. In the authors' experience, amputee subjects tend to prefer slightly less stance knee flexion, perhaps due to the compliance of the socket interface and/or the lack of proprioception in the limb.

All subjects' ankle behaviors also closely match those of healthy subjects. Most notable is the significant plantarflexion of the ankle joint around 60% of stride. During this period the ankle joint is delivering net positive power, which is a characteristic unique to an active device. Furthermore, the prosthesis actively returns from plantarflexion after toe-off in order to provide ground clearance at the toe during the swing phase of walking.

Figure 6-8 shows the body-mass-normalized knee and ankle joint torques provided by the prosthesis as a function of stride for each subject, also compared to the band of typical healthy subject knee and ankle body-mass-normalized torques. Like the joint kinematics, the joint torques for all subjects are strongly representative of healthy subject data. Regarding the knee torques, the amplitudes for the stance phase reflect the somewhat diminished stance knee flexion relative to healthy subjects. As in the healthy subject data, during the beginning of powered push-off (approximately 45% of stride), the powered prosthesis provides for each subject a flexive torque to counteract the hyperextensive torque supplied by the ground reaction force.

At the ankle, the prosthesis provides an initial dorsiflexive torque immediately following heel strike, followed by a period of increasing plantarflexive torque during the stance phase of walking. As in the healthy subject data, the ankle torque increases throughout stance, and peaks during the powered push-off period between 40 and 60% of stride. Once the toe is off the ground, the external forces on the ankle are small, due to the foot's low moment of inertia, and so little external torque is present during this period.

Body-mass-normalized knee and ankle joint powers for each subject are plotted in Fig. 6-9. As seen in the joint power data, power characterizing the knee and ankle joints falls largely within the healthy subject norms. Regarding the knee joint, power associated with stance knee flexion during early to middle stance is diminished, corresponding to the reduced stance knee flexion seen in these subjects. However, knee joint power during late stance and swing is quite representative of healthy knee joint power data.

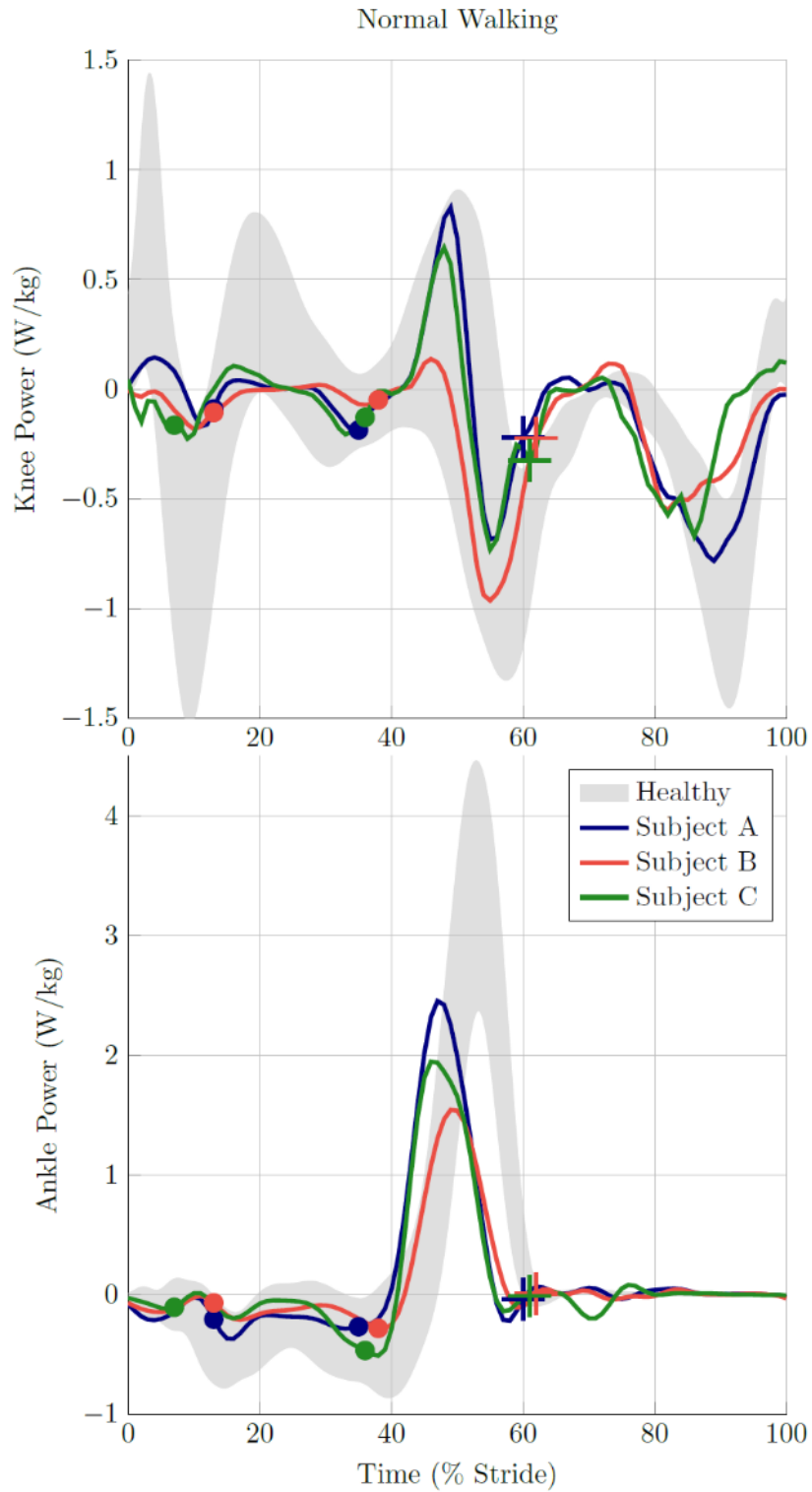


Figure 6-9. Knee and ankle powers for 3 amputee subjects using the powered prosthesis. For both joints positive power is power delivered by the joint, and negative power is power absorbed by the joint. The dots are average state transitions for each subject (from Phase 0 to 1, and from Phase 1 to 2). The crosses denote toe off, as measured by the load cell.

As in the knee joint, the power associated with the ankle joint is quite representative of healthy norms. Specifically, for each subject, the ankle primarily absorbs power during the early and middle phases of stance, and subsequently generates a pulse of power between approximately 40 and 60% of the stride cycle, in accordance with the powered push-off phase of walking. The net energy delivered by the ankle for each subject was 14.4, 9.5, and 13.7 J/stride, respectively, for subjects A, B, and C. Note that the peak power associated with this push-off is on the low side of the healthy mean. This phenomenon is related to torque and power limitations of the hardware. Nonetheless, these data are still in character with the biomechanical behavior of the healthy joint.

Conclusion

The authors describe in this article the design and control of a powered knee and ankle prosthesis for transfemoral amputees. The prosthesis was designed to emulate a generalizable mechanical behavior, and also to modify this behavior in real time, as governed by the prosthesis controller. The resulting system combines passive impedance-type behaviors at the respective joints during most of the stance phase of gait, and relatively high-impedance trajectory control during the swing phase of gait, the combination of which provides coordinated interaction with the user and minimal controller parameterization.

The powered prosthesis was demonstrated on three transfemoral amputee subjects, and shown in all cases to provide knee and ankle joint biomechanical behaviors that are highly representative of healthy joint biomechanics during walking. Finally, although only level walking was described and demonstrated, the authors note that one of the most unique and compelling attributes of a powered prosthesis, such as the one presented here, is its ability to adapt its behavior to a variety of activities and terrain types, and thus provide to the user appropriate biomechanical behaviors across a wide variety of activity. Accordingly, fulfilling the potential of powered prostheses will require the continuing development of coordination controllers for multiple types of activities, in addition to algorithmic structures that recognize when a user intends to transition from one activity to another.

CHAPTER VII

Contributions and Future Work

This work presents the design of lower limb prosthetic devices which provide biomechanically normal levels of torque, and speed and range of motion in self-contained, reliable, quiet, and anatomical packages. The transfemoral prosthesis is the only such device which has both powered knee and ankle joints. Specifically this work accomplishes the following:

- A fundamentally new transmission design using belts and chains was developed and tested. The design is capable of producing biomechanically appropriate levels of torque, stiffness, and damping for walking. The design is quieter and more reliable than the ballscrew version it replaced.
- A novel high ratio 196:1 hybrid traction/cable drive transmission for lower limb powered prostheses was designed and fabricated. The design promises to be even quieter than the belt, chain, chain version, but needs further testing.
- A parallel link ground sensing load cell was developed that is capable of sensing ground contact while mechanically filtering out moments.
- A leaf spring-foot combination was developed to decrease ankle motor torque at toe off.

Future work includes redesign of the transtibial device to incorporate the battery and electronics into a fully enclosed package.

References

1. Adams, P.F., G.E. Hendershot, and M.A. Marano, *Current estimates from the National Health Interview Survey, 1996*. National Center for Health Statistics. Vital Health Stat 10(200), 1999.
2. Waters, R.L., et al., *Energy cost of walking of amputees - Influence of level of amputation*. J. of Bone and Joint Surgery-American Vol., 1974. **vol. 58**(no. 1): p. pp. 42-46.
3. Winter, D.A., *The biomechanics and motor control of human gait: normal, elderly and pathological*. Vol. 2nd edition. 1991: University of Waterloo Press.
4. Sup, F., et al., *Preliminary Evaluations of a Self-Contained Anthropomorphic Transfemoral Prosthesis*. IEEE/ASME Transactions on Mechatronics in the focused section Anthropomorphism in Mechatronic Systems, 2009. **vol. 14**(iss. 6): p. pp. 667-676.
5. Donath, M., *Proportional EMG control for above knee prostheses*, in *Dept. of Mechanical Eng. M.S. Thesis*. 1974, Massachusetts Institute of Tech.
6. Flowers, W.C., *A man-interactive simulator system for above-knee prosthetics studies*, in *Dept. of Mechanical Eng. Ph.D. Thesis*. 1973, Massachusetts Institute of Tech.
7. Flowers, W.C. and R.W. Mann, *Electrohydraulic knee-torque controller for a prosthesis simulator*. ASME J. of Biomechanical Engineering, 1977. **vol. 99**(no. 4): p. pp. 3-8.
8. Grimes, D.L., *An active multi-mode above knee prosthesis controller*, in *Dept. of Mechanical Eng. Thesis Ph.D.* 1974, Massachusetts Institute of Tech.
9. Grimes, D.L., W.C. Flowers, and M. Donath, *Feasibility of an active control scheme for above knee prostheses*. ASME J. of Biomechanical Engineering, 1977. **vol. 99**(no. 4): p. pp. 215-227.
10. Stein, J.L. and W.C. Flowers, *Stance phase-control of above-knee prostheses - Knee control versus SACH foot design*. J. of Biomechanics, 1987. **vol. 20**(no. 1): p. pp. 19-28.
11. Stein, J.L., *Design issues in the stance phase control of above-knee prostheses*, in *Dept. of Mechanical Eng. Ph.D. Thesis*. 1973, Massachusetts Institute of Tech.
12. Bedard, S. and P. Roy, *Actuated leg prosthesis for above-knee amputees*, in *United States patent, USPTO*, Editor. 2003.
13. Martinez-Villalpando, E.C. and H. Herr, *Agonist-antagonist active knee prosthesis: A preliminary study in level-ground walking*. Journal of Rehabilitation Research and Development, 2009. **46**(3): p. 361-373.
14. Lambrecht, B.G.A. and H. Kazerooni. *Design of a semi-active knee prosthesis*. in *Robotics and Automation, 2009. ICRA '09. IEEE International Conference on*. 2009.
15. Bellman, R., A. Holgate, and T.G. Sugar, *Design of an active robotic ankle prosthesis with two actuated degrees of freedom using regenerative kinetics*. Proc. IEEE/RAS-EMBS Int. Conf. on Biomedical Robotics and Biomechatronics, 2008: p. pp. 511-516.
16. Hitt, J.K., et al., *An Active Foot-Ankle Prosthesis With Biomechanical Energy Regeneration*. Journal of Medical Devices-Transactions of the Asme, 2010. **4**(1).
17. Bergelin, B.J. and P.A. Voglewede, *Design of an Active Ankle-Foot Prosthesis Utilizing a Four-Bar Mechanism*. ASME Journal of Mechanical Design, 2012. **Vol. 134**: p. pp. .
18. Cherelle, P., et al., *Design and Validation of the Ankle Mimicking Prosthetic (AMP-) Foot 2.0*. Neural Systems and Rehabilitation Engineering, IEEE Transactions on, 2014. **22**(1): p. 138-148.
19. Au, S. and H. H., *Powered ankle-foot prosthesis*. IEEE Robotics & Automation Magazine, 2008. **vol. 15**: p. pp. 52-59.
20. Herr, H.M. and A.M. Grabowski, *Bionic ankle-foot prosthesis normalizes walking gait for persons with leg amputation*. Proceedings of the Royal Society B-Biological Sciences, 2012. **279**(1728): p. 457-464.
21. Fite, K.B., et al., *Design and Control of an Electrically Powered Knee Prosthesis*, in *IEEE International Conference on Rehabilitation Robotics*. 2007. p. pp. 902-905.
22. Sup, F., et al. *Design and Control of an Active Electrical Knee and Ankle Prosthesis*. in *Proceedings of the 2008 IEEE/RAS-EMBS International Conference on Biomedical Robotics and Biomechatronics*. 2008.
23. Loewenthal, S.H. and E.V. Zaretsky, *Design of Traction Drives*. Nasa Reference Publication 1985. **1154**.

24. Loewenthal, S.H., N.E. Anderson, and D.A. Rohn, *Evaluation of a High-Performance Fixed-Ratio Traction Drive*. Journal of Mechanical Design-Transactions of the Asme, 1981. **103**(2): p. 410-422.
25. Ai, X.L., M. Wilmer, and D. Lawrentz, *Development of friction drive transmission*. Journal of Tribology-Transactions of the Asme, 2005. **127**(4): p. 857-864.
26. Rooks, B., *The Harmonious Robot*. Industrial Robot, 2006. **33**(2): p. 6.
27. Winter, D.A., *The biomechanics and motor control of human gait*. 1987: University of Waterloo Press.
28. Garrison, G., *Santo Trac 50 Graphs*, J.E. Mitchell, Editor. 2011.
29. Norton, R.L., *Machine Design, An Integrated Approach*. 1997, Upper Saddle River: Prentice-Hall.
30. Ai, X., *Wedge Loading Mechanism for Traction Drives in United States patent*, USPTO, Editor. 2007: US.
31. Flugrad, D.R. and A.Z. Qamhiyah, *A self-actuating traction-drive speed reducer*. Journal of Mechanical Design, 2005. **127**(4): p. 631-636.
32. Kolchi, S., et al., *Auxiliary Device for Bicycle wit Traction Roller Type Gear*, USPTO, Editor. 2003.
33. Loewenthal, S.H. and D.A. Rohn, *Elastic Model of the Traction Behavior of Two Traction Lubricants*. ASLE Transactions, 1984. **27**(2): p. 9.
34. http://64.201.227.3/sava/sava_cat.pdf. *Sava cable life*
35. Chironis, N.P. and N. Sclater, *Mechanisms and Mechanical Devices Sourcebook*. 2nd. ed. 1996, Washington, D.C.: McGraw-Hill.
36. <http://www.magnomatics.com/default.aspx>.
37. Kumar, M.S. and S. Vijayarangan, *Static analysis and fatigue life prediction of steel and composite leaf spring for light passenger vehicles*. Journal of Scientific & Industrial Research, 2007. **66**: p. 7.
38. Shultz, A.H., et al. *Preliminary evaluation of a walking controller for a powered ankle prosthesis*. in *Robotics and Automation (ICRA), 2013 IEEE International Conference on*. 2013.
39. Genin, J.J., et al., *Effect of speed on the energy cost of walking in unilateral traumatic lower limb amputees*. European Journal of Applied Physiology, 2008. **103**(6): p. 655-663.
40. Waters, R., et al., *Energy cost of walking of amputees: the influence of level of amputation*. J Bone Joint Surg Am, 1976. **58**(1): p. 42-46.
41. Schmalz, T., S. Blumentritt, and R. Jarasch, *Energy expenditure and biomechanical characteristics of lower limb amputee gait: The influence of prosthetic alignment and different prosthetic components*. Gait & Posture, 2002. **16**(3): p. 255-263.
42. Jaegers, S.M.H.J., J.H. Arendzen, and H.J. Dejongh, *Prosthetic Gait of Unilateral Transfemoral Amputees - a Kinematic Study*. Archives of Physical Medicine and Rehabilitation, 1995. **76**(8): p. 736-743.
43. Schmid, A., et al., *Centre of pressure displacements in trans-femoral amputees during gait*. Gait & Posture, 2005. **21**(3): p. 255-262.
44. Seroussi, R.E., et al., *Mechanical work adaptations of above-knee amputee ambulation*. Archives of Physical Medicine and Rehabilitation, 1996. **77**(11): p. 1209-1214.
45. Vrieling, A.H., et al., *Uphill and downhill walking in unilateral lower limb amputees*. Gait & Posture, 2008. **28**(2): p. 235-242.
46. Miller, W.C., et al., *The influence of falling, fear of falling, and balance confidence on prosthetic mobility and social activity among individuals with a lower extremity amputation*. Archives of Physical Medicine and Rehabilitation, 2001. **82**(9): p. 1238-1244.
47. Miller, W.C., M. Speechley, and B. Deathe, *The prevalence and risk factors of falling and fear of falling among lower extremity amputees*. Archives of Physical Medicine and Rehabilitation, 2001. **82**(8): p. 1031-1037.
48. Tomovic, R. and R.B. McGhee, *A Finite State Approach to the Synthesis of Bioengineering Control Systems*. Human Factors in Electronics, IEEE Transactions on, 1966. **HFE-7**(2): p. 65-69.
49. Flowers, W.C., *Use of an amputee-computer interactive facility in above-knee prosthesis research*, in *Proceedings of the 1974 annual conference - Volume 1*. 1974, ACM. p. 335-339.
50. Au, S., M. Berniker, and H. Herr, *Powered ankle-foot prosthesis to assist level-ground and stair-descent gaits*. Neural Networks, 2008. **21**(4): p. 654-666.
51. Au, S.K., J. Weber, and H. Herr, *Powered Ankle-Foot Prosthesis Improves Walking Metabolic Economy*. Ieee Transactions on Robotics, 2009. **25**(1): p. 51-66.

52. Eilenberg, M.F., H. Geyer, and H. Herr, *Control of a Powered Ankle-Foot Prosthesis Based on a Neuromuscular Model*. Neural Systems and Rehabilitation Engineering, IEEE Transactions on, 2010. **18**(2): p. 164-173.
53. Mathew A. Holgate, A.W.B., Thomas G. Sugar. *Control Algorithms for Ankle Robots: A Reflection on the State-of-the-Art and Presentation of Two Novel Algorithms*. in *Conference on Biomedical Robotics and Biomechanics*. 2008. Scottsdale, AZ.
54. Hitt, J.K., et al., *An Active Foot-Ankle Prosthesis With Biomechanical Energy Regeneration*. Journal of Medical Devices, 2010. **4**(1): p. 011003-011003.
55. Bergelin, B.J., et al., *Concept Through Preliminary Bench Testing of a Powered Lower Limb Prosthetic Device*. Journal of Mechanisms and Robotics, 2010. **2**(4): p. 041005-041005.
56. Bergelin, B.J. and P.A. Voglewede, *Design of an Active Ankle-Foot Prosthesis Utilizing a Four-Bar Mechanism*. Journal of Mechanical Design, 2012. **134**(6): p. 061004-061004.
57. Suzuki, R., et al. *Control method for powered ankle prosthesis via internal model control design*. in *Mechatronics and Automation (ICMA), 2011 International Conference on*. 2011.
58. Caputo, J.M. and S.H. Collins, *A Universal Ankle-Foot Prosthesis Emulator for Human Locomotion Experiments*. Journal of Biomechanical Engineering, 2014. **136**(3): p. 035002-035002.
59. Hoover, C.D., G.D. Fulk, and K.B. Fite, *Stair Ascent With a Powered Transfemoral Prosthesis Under Direct Myoelectric Control*. Mechatronics, IEEE/ASME Transactions on, 2013. **18**(3): p. 1191-1200.
60. Rouse, E.J., et al. *Clutchable series-elastic actuator: Design of a robotic knee prosthesis for minimum energy consumption*. in *Rehabilitation Robotics (ICORR), 2013 IEEE International Conference on*. 2013.
61. Sup, F., et al., *Preliminary Evaluations of a Self-Contained Anthropomorphic Transfemoral Prosthesis*. Mechatronics, IEEE/ASME Transactions on, 2009. **14**(6): p. 667-676.
62. Sup, F., H.A. Varol, and M. Goldfarb, *Upslope Walking With a Powered Knee and Ankle Prosthesis: Initial Results With an Amputee Subject*. Neural Systems and Rehabilitation Engineering, IEEE Transactions on, 2011. **19**(1): p. 71-78.
63. Lawson, B., et al., *Control of Stair Ascent and Descent With a Powered Transfemoral Prosthesis*. Neural Systems and Rehabilitation Engineering, IEEE Transactions on, 2013. **21**(3): p. 466-473.
64. Lawson, B.E., H.A. Varol, and M. Goldfarb, *Standing Stability Enhancement With an Intelligent Powered Transfemoral Prosthesis*. Biomedical Engineering, IEEE Transactions on, 2011. **58**(9): p. 2617-2624.
65. Sup, F., A. Bohara, and M. Goldfarb. *Design and Control of a Powered Knee and Ankle Prosthesis*. in *Robotics and Automation, 2007 IEEE International Conference on*. 2007.
66. C.C. Gordon, T.C., C.E. Clauser, B. Bradtmiller, and J.T. McConville, *Anthropometric survey of US army personnel: methods and summary statistics - 1988*. 1989.
67. Colgate, J.E. and J.M. Brown. *Factors affecting the Z-Width of a haptic display*. in *Robotics and Automation, 1994. Proceedings., 1994 IEEE International Conference on*. 1994.
68. Colgate, J.E. and G. Schenkel. *Passivity of a class of sampled-data systems: application to haptic interfaces*. in *American Control Conference, 1994*. 1994.
69. Diolaiti, N., et al., *Stability of Haptic Rendering: Discretization, Quantization, Time Delay, and Coulomb Effects*. Robotics, IEEE Transactions on, 2006. **22**(2): p. 256-268.